

Diploma Thesis

(Diplomarbeit zur Erlangung des akademischen Grades eines Diplom-Ingenieurs der Studienrichtung Verfahrenstechnik an der Technischen Universität Graz)

Ultra Scale-Down of a Disc Stack Separator

Michael Felber

Advisors:

Dipl.Ing. Stefan Radl

Univ.-Prof. Dr.techn. Dipl.Ing. Johannes G. Khinast

Institute for Process and Particle Engineering

Research Group Pharmaceutical Engineering

Graz, February 2010

Declaration

The work presented in this diploma thesis is to the best of my knowledge and belief, original, except as acknowledged in the text. This material has not been submitted, either in the whole or in part, for a degree at this or any other university.

Place, Date

Signature

Eidesstattliche Erklärung

Ich erkläre an Eides Statt, dass ich die vorliegende Arbeit selbstständig und ohne fremde Hilfe verfasst, andere als die angegebenen Quellen nicht benutzt und die den benutzten Quellen wörtlich und inhaltlich entnommenen Stellen als solche kenntlich gemacht habe. Ich versichere, dass ich dieses Diplomarbeitsthema bisher weder im In- noch im Ausland (einem Beurteiler oder einer Beurteilerin) in irgendeiner Form als Prüfungsarbeit vorgelegt habe.

Ort, Datum

Unterschrift

Acknowledgements

I would like to express my sincere gratitude to my advisors Dipl.Ing. Stefan Radl and Prof. Johannes G. Khinast for their support, guidance and patience during this work.

Furthermore, I want to thank Sandoz, as the sponsor of this project, for providing the opportunity to make this work possible.

Additionally, I would like to thank all of those who helped to complete this picture. Many thanks to my colleagues at the institute for supporting me, directly and indirectly. I am grateful for all the enriching conversations and tasteful tea breaks.

Last but not least, I would like to thank my family and friends. I want to thank my girlfriend Birgit for her growing interest and support. Special thanks go to my parents and grandparents for supporting me ever since I can remember.

Abstract

Performance prediction of full-scale processes is an important factor during the development of new products in the pharmaceutical industry. Mimicking a full-scale process with a minimal amount of feed material on the laboratory scale reduces the necessary time for development, and therefore, allows a significant reduction of the connected costs. In this work, a laboratory-scale process matching an industrial-scale disc stack separator, installed at Sandoz, had to be found. The design of such a laboratory-scale process, a so-called ultra scale-down (USD) process, is presented in this work.

The key influences in the processes have been identified through literature study, which lead to a proposed scale-down process. Disc stack separators expose bio-materials to significant levels of stress in the entrance region, due to the acceleration in the fast turning bowl. This effect leads to cell destruction connected with a reduction of clarification performance due to small-sized cell debris. Laboratory centrifuges alone are not sufficient to mimic the full-scale process behaviour, since the fluid, relative to the centrifuge tubes, is at rest during processing. Therefore, a shear device has been designed to produce similar cell destruction prior to the laboratory centrifuge runs. The shear device consists of a motor-driven rotating disc in a cylindrical chamber with attached inlet and outlet tubes. The geometry of the shear device has been determined by simulations, and lead to a final geometry of the cylindrical chamber of 50 [mm] in diameter with a height of 20 [mm]. The operating parameters have been determined by simulations for the shear device and according to the Sigma theory of equivalent settling area for the laboratory centrifuge. Since the required quantity of feed material is unfavorable for batch processing, a continuous process including a tube pump has been proposed.

The occurring stress-level in the entrance region of the disc stack separator has been quantified by simulations. The stress-level exposure, expressed through the energy dissipation rate (EDR), was in the order of $10^5 [W kg^{-1}]$. Additionally, simulations of the dense phase passing the narrow contraction of the so-called Viscon nozzles showed EDR levels up to $10^9 [W kg]$. Furthermore, an attempt to estimate the EDR during droplet impact after discharge of bio-material through automatically opened nozzles has been made. Here, the flow is characterized by significant complexity due to the very high circumferential speed of the nozzles (up to $200 [m s^{-1}]$) in the housing. Calculations of a simplified approach with air resistance for spherical rigid droplets in a stationary atmosphere indicated that high EDR levels above $10^9 [W kg]$ are possible for larger droplets. These calculations indicated the high potential for cell destruction in the Viscon nozzles and the ejection mechanism. The design of additional components for the USD process, mimicking these effects, still offers challenges for future investigations.

Kurzfassung

Das Abschätzen des Prozessverhaltens von Produktionslinien stellt einen entscheidenden Faktor in der pharmazeutischen Produktentwicklung dar. Gelingt eine repräsentative Abbildung des Prozesses in Laborgröße, z.B. mit Hilfe eines Ultra Scale-Down (USD) Prozesses, so kann die Entwicklungszeit auf ein Minimum reduziert werden, wie auch die damit verbundenen Entwicklungskosten. In dieser Arbeit wurde ein Laborprozess ausgelegt, der einen Tellerseparator der Sandoz GmbH in Produktionsgröße repräsentativ abbilden soll.

Die Haupteinflüsse auf den Prozess wurden durch eine Literaturstudie erarbeitet, und waren die Grundlage für die Auslegung des vorgeschlagenen Konzepts. Die Beschleunigung des eintretenden Materials im Eintrittsbereich des Tellerseparators bewirkt hohen Zellstress bei biologischen Produkten, und führt unter Umständen zu Zellzerstörung. Das aufgebrochene Zellmaterial verschlechtert in weiterer Folge die Klärleistung des Separators. In Laborzentrifugen befindet sich das Produkt, relativ zu den Behältern, in Ruhe, und zeigt folglich keine Zellzerstörung. Daher war es notwendig eine Schereinrichtung auszulegen und der Laborzentrifuge vorzuschalten. Als Schereinrichtung wurde eine rotierende Scheibe in einer zylindrischen Kammer gewählt, wobei die finale Geometrie anhand von Simulationen bestimmt wurde (Kammerdurchmesser 50 [mm], Höhe 20 [mm]). Die Betriebsparameter des USD Prozesses wurden mittels Simulationen für die Schereinrichtung und der Sigma Theorie der äquivalenten Klärflächen für die Laborzentrifuge bestimmt. Diskontinuierliches Betreiben des USD Prozesses würde Nachteile bezüglich von Chargenwechsel bringen, und daher wurde der Prozess kontinuierlich mit einer Schlauchpumpe ausgelegt.

Der Zellstress im Eintrittsbereich des Tellerseparators wurde mit Computersimulationen bestimmt. Der Zellstress wurde mit der Energiedissipationrate (EDR) quantifiziert und ergab eine Größenordnung von $10^5 [W kg^{-1}]$. Zusätzlich wurden Simulation der Strömung durch die Querschnittsverengungen in den sogenannten Viscon-Düsen vorgenommen. Das Ergebnis lieferte eine EDR in einer Größenordnung von über $10^9 [W kg^{-1}]$. Weiters wurde versucht die EDR im Aufprall der Tropfen nach dem Abschleudern der schweren Phase von den hydraulischen Düsen abzuschätzen. Die Strömungsverhältnisse in diesem Bereich sind aufgrund der hohen Drehzahl des Separators (Umfangsgeschwindigkeit über $200 [m s^{-1}]$) hochkomplex. Vereinfachungen durch kugelförmige, starre Tropfen in einer ruhenden Atmosphäre ergaben EDR über $10^9 [W kg]$ für größere Tropfendurchmesser. Die Berechnungen weisen auf das hohe Potential für Zellzerstörung in den Viscon-Düsen und während dem Tropfenaufprall hin. Eine Erweiterung des Prozessdesigns, für die Abbildung dieser Verhältnisse, bietet Herausforderungen für weitere Arbeiten auf diesem Gebiet.

Contents

List of Figures	iv
List of Tables	vii
Nomenclature	viii
Abbreviations	xi
1 Introduction	1
1.1 Motivation	1
1.2 Objectives	1
1.3 Thesis Outline	2
2 Background	3
2.1 Basics of Disc Stack Separators	3
2.1.1 Analysis of the Flow in Disc Stack Separators	4
2.2 Droplet Impact on Surfaces	5
2.2.1 Basic Considerations	5
2.2.2 Cell Stress Associated with Droplet Impingement	5
2.3 Scale-Down Approaches for Disc Stack Separators	7
3 Proposed Scale-Down Approach for Sandoz' Disc Stack Separator	11
4 Simulation of Multiphase Flow	13
4.1 Available Simulation Concepts	13
4.2 Computational Methods and Models	15
4.2.1 Numerical Methods for Solving the Governing Equations of Fluid Flow	15
4.2.2 Particle Tracking Method	16
4.2.3 Turbulence Models	17
4.2.4 Launder-Sharma Low-Reynolds-Number Turbulence Model	18
4.3 Geometry and Grid Generation	19
4.4 Numerical Solution of the Governing Equations	19
4.5 Post-Processing	20
5 Results for Sandoz' Disc Stack Separator	21
5.1 Operating Parameters and Geometry	21
5.2 Simulation of the Inlet Pipes	21
5.2.1 Generation of the Geometry	21
5.2.2 Results of the Simulation	23

5.3	Simulation of the Full-Scale Separator	23
5.3.1	Grid Generation	23
5.3.2	Boundary Conditions for the Simulations	29
5.3.3	Results	30
5.4	Viscon Nozzles	38
5.4.1	Estimation of the Energy Dissipation Rate in the Viscon Nozzles	39
5.4.2	Simulation of the Viscon Nozzles	41
5.4.3	Results	42
5.5	Radial Exit Nozzles	49
5.5.1	EDR Estimation Neglecting Air Resistance	50
5.5.2	EDR Estimation Including Air Resistance	52
6	Design of the Ultra Scale-Down Device	56
6.1	Designing the Shear Device	56
6.1.1	Geometrical Configurations of the Shear Device	57
6.1.2	EDR Profiles	58
6.1.3	Influence of the Computational Mesh	62
6.1.4	Comparison of Different Geometries	63
6.1.5	Geometry of the Shear Device	67
6.2	Operating Parameters of the Shear Device	69
6.2.1	Generating the Computational Mesh	69
6.2.2	Running the Simulations	69
6.2.3	Results of the Simulations	69
6.3	Sigma Theory of Equivalent Settling Area	71
6.3.1	Applying the Sigma Theory to Sandoz' Disc Stack Separator . .	73
6.3.2	Applying the Sigma Theory to the Laboratory Centrifuge	75
6.3.3	Experimental Determination of the Correction Factor of the Disc Stack Separator	79
6.4	Specifications of the Ultra Scale-Down Process	80
6.4.1	Tube Pump	80
6.4.2	Shear Device	83
6.4.3	Cooling of the Shear Device	85
6.4.4	Accessories	88
7	Conclusions and Outlook	90
7.1	Conclusions	90
7.2	Outlook	90
	References	92

Appendix	95
A Components of the Ultra Scale-Down Process	95
A.1 Data Sheets of Components	95
A.2 Offers for Key Components	101
B Simulation-Related Content	104
B.1 Particle Tracking	104
B.2 EDR Profile Simulations	112
B.2.1 M4 Script File for a Parameter-Based Mesh Generation of the Shear Device	112
B.2.2 The makeMesh Shell Script	117
B.2.3 Determination of the EDR Profiles	118
B.2.4 Calculating the Total EDR of a Simulation	122
C EDR Calculation for Radial Exit Nozzles	125
C.1 Numerical Calculation of the EDR	125
C.2 Validation of the Numerical Approach	128
C.2.1 Drag after Clift and Gauvin	128
C.2.2 Stokes Law	128
D Data from Sandoz	129
D.1 Data from Test Runs of the Disc Stack Separator	129

List of Figures

2.1	Schematic drawing of a disc stack separator with automatic continuous discharge	3
2.2	Droplets deposition model: critical curve (schematically, after [Mundo et al., 1995])	6
2.3	Droplet with suspended cells impacting on a liquid layer [Wang et al., 2008]	6
3.1	Illustration of the proposed ultra scale-down process	11
5.1	Geometry of the first section of the inlet pipe system (section1)	22
5.2	Geometry of the second section of the inlet pipe system (section2)	22
5.3	Surface plot of the computational mesh of the inlet pipe system	23
5.4	Plot of the magnitude of the velocity at the outlet of the second section of the inlet pipes (section2)	24
5.5	Schematic drawing of the full-scale separator geometry	25
5.6	Schematic drawing of the periodic slice of the separator geometry	25
5.7	Ordering pattern of cell faces for the cyclic patch boundary conditions required by <i>OpenFOAM</i>	27
5.8	Ordering pattern of multiple surfaces in a cyclic patch required by <i>OpenFOAM</i>	27
5.9	Full-scale separator mesh with 800k cells	28
5.10	Velocity in the 800k cells mesh (plane cut through the baffled region of the separator)	31
5.11	Relative velocity to the rotating walls in the 800k cells mesh (plane cut through the baffled region of the separator)	32
5.12	Energy dissipation rate (plane cut through the baffled region of the separator)	33
5.13	Plot of the EDR in the disc stack separator ($\omega_{DS} = 8,000 [rpm]$, $\dot{m}_f = 2,500 [kg h^{-1}]$, 2.6M cell mesh)	35
5.14	Plot of the EDR at the disc attached to the inlet pipe exit and at the edges of the baffles ($\omega_{DS} = 8,000 [rpm]$, $\dot{m}_f = 2,500 [kg h^{-1}]$, 2.6M cell mesh)	36
5.15	Plot of the EDR at the outer edges of the baffles ($\omega_{DS} = 8,000 [rpm]$, $\dot{m}_f = 2,500 [kg h^{-1}]$, 2.6M cell mesh)	36
5.16	Plot of the magnitude of the velocity in the disc stack separator ($\omega_{DS} = 8,000 [rpm]$, $\dot{m}_f = 2,500 [kg h^{-1}]$, 2.6M cell mesh)	37
5.17	Plot of the velocity vectors of the relative velocity in the disc stack separator ($\omega_{DS} = 8,000 [rpm]$, $\dot{m}_f = 2,500 [kg h^{-1}]$, 2.6M cell mesh)	38
5.18	Schematic drawing of the geometry of the Viscon nozzles	39

5.19	Inlet and outlet boundary used for the Viscon nozzle simulation	42
5.20	The computational mesh of the Viscon nozzles	43
5.21	Plot of the simulation results for the Viscon nozzle simulation ($\dot{m}_d = 160 [kg h^{-1}]$)	44
5.22	Plot of the simulation results for the Viscon nozzle simulation ($\dot{m}_d = 330 [kg h^{-1}]$)	45
5.23	Plot of the simulation results for the Viscon nozzle simulation ($\dot{m}_d = 520 [kg h^{-1}]$)	46
5.24	Plot of the simulation results for the Viscon nozzle simulation ($\dot{m}_d = 700 [kg h^{-1}]$)	47
5.25	Results for the pressure drop of the Viscon nozzles	48
5.26	Results for the energy dissipation rate of the Viscon nozzles	48
5.27	Schematic drawing of a cut through the radial exit nozzles	49
5.28	Schematic drawing for the estimation of the impact time of a droplet on a wall.	50
5.29	Schematic drawing of the exit velocity of discharged material from the separator	52
6.1	Geometry parameters of the shear device	56
6.2	Computational mesh of the shear device	58
6.3	Plot of the energy dissipation rate	59
6.4	Plot of the magnitude of the velocity	59
6.5	Schematic plot of the particle positions during the particle tracking simulation.	60
6.6	EDR exposure over time for two sample particles	61
6.7	Typical cumulative distribution	61
6.8	Typical frequency distribution chart	62
6.9	Comparison of the effect of the mesh size, frequency distribution (Geom.: $r_{SD} = 40 [mm]$, $h_{SD} = 30 [mm]$)	63
6.10	Comparison of the effect of the mesh size, cumulative distribution (Geom.: $r_{SD} = 40 [mm]$, $h_{SD} = 30 [mm]$)	63
6.11	Geometry: $r_{SD} = 30 [mm]$, $h_{SD} = 20 [mm]$	64
6.12	Geometry: $r_{SD} = 40 [mm]$, $h_{SD} = 30 [mm]$	64
6.13	Geometry: $r_{SD} = 40 [mm]$, $h_{SD} = 40 [mm]$	65
6.14	Geometry: $r_{SD} = 50 [mm]$, $h_{SD} = 30 [mm]$	65
6.15	Geometry: $r_{SD} = 50 [mm]$, $h_{SD} = 40 [mm]$	66
6.16	Geometry: $r_{SD} = 50 [mm]$, $h_{SD} = 50 [mm]$	66
6.17	Low Reynolds number mesh of the shear device ($r_{SD} = 25 [mm]$, $h_{SD} = 20 [mm]$)	70
6.18	Operating parameters of the shear device	71

6.19	Power consumption of the shear device	72
6.20	Geometrical parameters in the Sigma equation of a disc stack separator	73
6.21	Schematic drawing of the shear device assembly	81
6.22	Schematic drawing of the shear device assembly, details shearing chamber (measurements in $[mm]$)	82
6.23	Schematic drawing of the temperature conditions in the shear device . .	87
C.1	Validation of the numerical calculation for a constant drag coefficient c_D after Clift and Gauvin with $D_{drop} = 10^{-3} [m]$ and $v_{exit} = 150 [m s^{-1}]$ [Clift et al., 1978]	128
C.2	Validation of the numerical calculation for Stokes' law ($D_{drop} = 10^{-5} [m]$, $v_{exit} = 1 [m s^{-1}]$)	128

List of Tables

5.1	Window of operation of the disc stack separator	21
5.2	Simulated operating conditions of the disc stack separator	29
5.3	The values for y^+ from the full scale separator mesh (800k cells) . . .	30
5.4	y^+ from the full scale separator simulation (2.6M cells, $\dot{m}_f = 2,500 [kg h^{-1}]$, $\omega_{DS} = 8,000 [rpm]$)	34
5.5	Maximum energy dissipation rate in the separator (2.6M cell mesh) . .	34
5.6	Results of the estimation of the energy dissipation rate in the Viscon nozzles	41
5.7	Maximum energy dissipation rates in the Viscon nozzle simulations . .	47
5.8	Energy dissipation rate of a spherical droplet dependent on the droplet diameter and its velocity	51
5.9	Energy dissipation rate of the impact of a spherical drop on the separator housing considering air resistance	55
6.1	Geometrical configurations of the shear device	57
6.2	Results from the total EDR calculations of the shear device simulations	68
6.3	Geometrical details of Sandoz' disc stack separator	74
6.4	Results of the equivalent settling area and the term $Q_{ds}/C_{ds}\Sigma_{ds}$ of the disc stack separator for different operating points	75
6.5	Specifications of the laboratory centrifuge (Beckman Coulter Avanti J-25)	76
6.6	Specifications of the rotor of the laboratory centrifuge (Beckman Coulter JLA-9.1000)	76
6.7	Specifications of the swing-out analog rotor of the laboratory centrifuge (Beckman Coulter JS-4.0)	76
6.8	Parameter settings at different operating points	78
6.9	Summary of the results of the run time calculations	78
6.10	Comparison of the runtime of the laboratory centrifuge without and with the acceleration and deceleration phases	79
6.11	Specifications of the tube pump	80
6.12	Specifications of the tube pump tubes	81
6.13	Specifications of the Maxon EC 25 motor	84
6.14	Specification of the Maxon DEC 70/10 speed and current controller for the motor	84
6.15	Specifications of the power supply model EA-PS 880-40 R	85
6.16	Specification of the coupling of the motor shaft (MK2 Serie 5 Coupling)	85
6.17	Temperature increase of the fluid flow through the shear device depen- dent on the power output of the motor ($\dot{m}_{USD} = 0.170 [kg min^{-1}]$) . .	86

Nomenclature

Roman Symbols

Symbol	Description	Units
A_D	Reference area for drag	$[m^2]$
B_L	Spacer width	$[m]$
C	Correction factor in the Sigma theory	$[-]$
C	Concentration of broken cell material	$[-]$
c_D	Drag coefficient	$[-]$
c_p	Specific heat capacity	$[J kg^{-1} K^{-1}]$
D	Diameter	$[m]$
E	Energy	$[J]$
f	Damping functions	$[-]$
F_L	Correction factor for the settling area	$[-]$
g	Gravitational acceleration	$[m s^{-2}]$
\mathbf{g}	Gravitational acceleration vector	$[m s^{-2}]$
h	Height	$[m]$
k	Overall thermal heat transfer coefficient	$[W m^{-2} K^{-1}]$
k	Turbulent kinetic energy	$[m^2 s^{-2}]$
K	Loss coefficient	$[-]$
m	Mass	$[kg]$
\dot{m}	Mass flow rate	$[kg s^{-1}]$
n, N	Number variable	$[-]$
Oh	Ohnesorge number	$[-]$
p	Pressure	$[Pa]$ or $[m^2 s^{-2}]$
P	Power	$[W]$
P_k	Production term of k	$[kg m^{-1} s^{-3}]$
Q	Volumetric flow rate	$[m^3 s^{-1}]$
\dot{Q}	Heat transfer rate	$[W]$
q_P	Frequency of particles	$[kg W^{-1}]$
Q_P	Fraction of particles	$[-]$
R, r	Radius	$[m]$
Re	Reynolds number	$[-]$
s_{wall}	Wall thickness	$[m]$
t	Time	$[s]$
t_{res}	Average residence time	$[s]$
T	Temperature	$[K]$
\mathbf{u}	Velocity vector	$[m s^{-1}]$

Symbol	Description	Units
U	Velocity	$[m\ s^{-1}]$
v	Velocity	$[m\ s^{-1}]$
V	Volume	$[m^3]$
\dot{V}	Volumetric flow rate	$[m^3\ s^{-1}]$
V_c	Volume of the contraction zone of one Viscon nozzle	$[m^3]$
w	Velocity	$[m\ s^{-1}]$
Z_L	Number of spacers	$[-]$

Greek Symbols

Symbol	Description	Units
α	Heat transfer coefficient	$[W\ m^{-2}\ K^{-1}]$
ϵ	Energy dissipation rate, turbulent dissipation	$[W\ kg^{-1}]$
θ	Half conical angle of the disc stack	$[rad]$
λ_{wall}	Thermal conductivity of wall material	$[W\ m^{-1}\ K^{-1}]$
μ	Dynamic viscosity	$[Pa\ s]$
ν	Kinematic viscosity	$[m^2\ s^{-1}]$
ρ	Density	$[kg\ m^{-3}]$
Σ	Equivalent settling area	$[m^2]$
σ	Surface tension	$[kg\ s^{-2}]$
ω	Angular velocity	$[rad\ s^{-1}]$

Subscripts

Symbol	Description
\perp	Perpendicular
1,2,3	Position index
<i>cool</i>	Cooling
<i>crit</i>	Critical value
<i>d</i>	Dense phase
<i>d</i>	Rotating disc
<i>ds</i>	Disc stack separator
<i>drop</i>	Droplet
<i>exit</i>	Radial exit nozzles index
<i>f</i>	Feed
<i>fl</i>	Fluid
<i>i</i>	Class indicator
<i>h</i>	Homogenization
<i>h</i>	Separator housing

Symbol	Description
<i>imp</i>	Impact
<i>in</i>	Inlet
<i>kin</i>	Kinetic
<i>l</i>	Light phase
<i>lab</i>	Laboratory centrifuge
<i>m</i>	Mean
<i>motor</i>	Motor of the shear device
<i>P</i>	Particles
<i>RD</i>	Rotating disc
<i>Sample</i>	Sample
<i>SD</i>	Shear device
<i>USD</i>	Ultra scale-down
<i>VN</i>	Viscon nozzles

Abbreviations

CFD	Computational Fluid Dynamics
DNS	Direct Numerical Simulation
EDR	Energy Dissipation Rate
FDM	Finite Differences Method
FEM	Finite Element Method
FVM	Finite Volume Method
LES	Large Eddy Simulation
LSD	Lagrangian Stochastic Deterministic model
OD	Optical Density
PTM	Particle Tracking Method
RANS	Reynolds Averaged Navier-Stokes equation
SD	Shear Device
USD	Ultra Scale-Down

1 Introduction

1.1 Motivation

The motivation for this work is the development of a laboratory-scale process, that mimics the process characteristics of Sandoz' full-scale disc stack separator. The prediction of the performance of the full-scale process is an important factor during the development of new pharmaceutical and biochemical products. A laboratory-scale process requires only minimum amounts of feed material, it reduces the necessary time for the development of the products and hence can save significant development costs.

The classical approach for such a scale-down task is based on a direct scale-down of the device itself. Thus, the laboratory-scale separator has just a smaller throughput and has essentially the same design as the full-scale system. In the classical approach, scaling is often based on equivalent settling area. Such a design does not necessarily guarantee identical flow conditions in the laboratory-scale and the full-scale separator. The correct way would be to identify the key influence parameters on the product quality, and then to keep these parameters constant during the scale-down process. This does not necessarily mean that a disc stack separator has to be used in the laboratory-scale process.

In the laboratory-scale process, the bio-material can be processed in minimal amounts. If an extremely large scale-down ratio is used, one speaks of an "ultra-scale down" approach. This has an additional advantage: the amount of the available feed material of new pharmaceutical substances is no limiting factor any more. Hence, more products can be screened in short time, which can be a driver for innovative products.

1.2 Objectives

The main objective of this work is to design a laboratory-scale process to mimic a full-scale separation process. In the full-scale separation process, shear sensitive bio-material (i.e., microbial cells) is separated from the product stream of an industrial fermenter. Sandoz uses a disc stack separator for this purpose. The design of the laboratory-scale process should be based on a literature study and the simulation of the flow in the separation process.

The work has been divided into the following tasks:

- Review of literature about the ultra scale-down approach of disc stack separators.
- Simulation of the full-scale separator.
- Identification of the key influence parameters on cell destruction in the full-scale process.

- Definition and basic engineering of the components of the ultra scale-down process.
- Simulation of the ultra-scale down device.
- Determination of the operating parameters for the ultra scale-down device.

1.3 Thesis Outline

The review of literature on the ultra scale-down approach of disc stack separators is discussed in Section 2, followed by an introduction to the proposed scale down approach in Section 3. Section 4 describes some basics of computational fluid dynamics relevant for this problem and discusses the models used for our simulations. The simulation results of the full-scale disc stack separator, the inlet pipes and the Viscon nozzles are provided in Section 5. The energy dissipation rate in droplets impacting on surfaces, a situation that occurs when the radial exit nozzles of the disc stack separator are opened, has been estimated (see Subsection 5.5). The design of the ultra scale-down process is described in Section 6, including the simulation of the shear device, the application of the Sigma theory of equivalent settling area, and the specifications of the USD process components. The final section, Section 7, discusses the conclusions drawn from this work and provides an outlook for future tasks.

2 Background

2.1 Basics of Disc Stack Separators

The disc stack separator is a widely used process component in general chemical engineering as well as in the biochemical industry [Chmiel, 2006]. Similar to common centrifuges, it is used to separate liquid-liquid, liquid-solid or liquid-liquid-solid phase mixtures based on density differences of the phases in a centrifugal force field. Due to the stacked discs in the separation region, this separator type has an increased settling area with short settling distances between the discs (see Figure 2.1). This leads to a high separation performance per unit volume. There are several designs of disc stack separators available on the market, e.g., with different discharge mechanisms (continuous or batch discharge), suitable for specific types of feed materials [Westfalia, 2010]. In this project, a Westfalia disc stack separator with a hydro-hermetic feed system and automatic continuous discharge (a Westfalia "HFA 65-01-477" Separator) is used to separate the product stream of an industrial fermentation. The product stream consists of a two phase mixture of *E.coli* cells within a liquid phase. According to Westfalia, its hydro-hermetic feed system should reduce the stress level exposure of the bio-material during the acceleration phase in the entrance region.

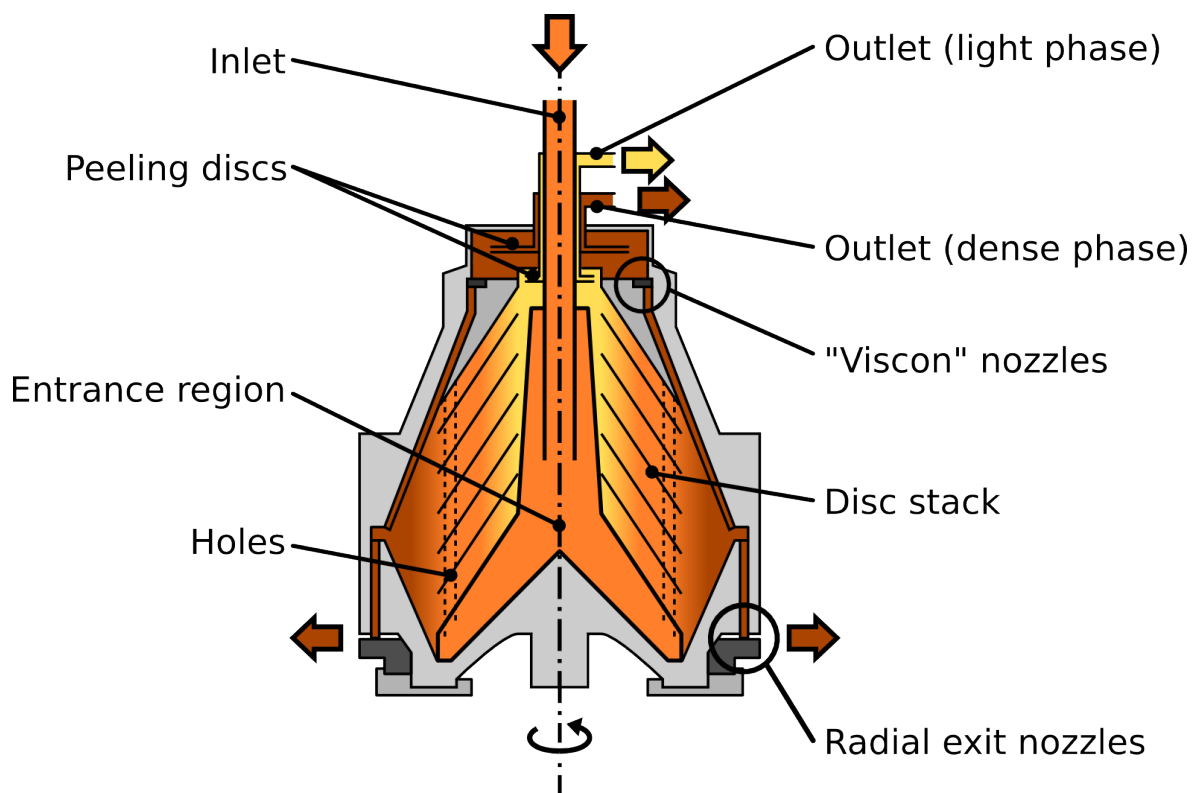


Figure 2.1: Schematic drawing of a disc stack separator with automatic continuous discharge

2.1.1 Analysis of the Flow in Disc Stack Separators

A schematic drawing of a disc stack separator with continuous discharge is shown in Figure 2.1. The feed material enters the rotating separator bowl through a stationary pipe inlet from the top. Then, the feed material is accelerated in the entrance region, which typically leads to a high degree of turbulence and consequently high shear forces. From there, the material flows between the stacked discs inside the separator bowl via channels of vertically positioned holes in the wall of the entrance region and the discs. The fluid rises up through these vertical holes and is being distributed between the discs, where the settling in the centrifugal force field takes place. The light phase flows in inward direction, and exits the bowl via a peeling disc. Then, the light phase flows through a concentric pipe positioned around the inlet pipe. The dense phase is collected on the discs and flows in outward direction. It is finally collected in the outer region of the bowl. From there, the dense phase is transported out of the separator via two different routes. One way is flowing upwards, through channels inside the bowl, passing through the so-called "Viscon" nozzles and a peeling disc. Finally, the dense phase leaves the separator through a pipe. The other route is via automatically opened exit nozzles. This route is activated when the discharge stream through the Viscon nozzles is not sufficient to discharge all the dense phase in the bowl. The opening and closing of the nozzles is hydraulically controlled by pumping operating-water into the opening mechanism. When the exit nozzles are opened, the material is radially ejected from the separator bowl. The circumferential velocity of the exiting jet is very high due to the separator's operation at high rotational speeds (up to 8,000 rpm). The impact of the jet on the surrounding housing (not shown in Figure 2.1), introduces a significant amount of energy dissipation on the discharged dense phase.

Bio-material, as a shear sensitive material, is exposed to high shear forces in a disc stack separator leading to cell breakage. The entrance region, where the acceleration of the fluid takes place, has been reported as a region of high shear stress [Boychyn et al., 2004]. Cell breakage related debris lead to a reduction of the average size of the particles. Since smaller particles have a lower settling velocity, they need more time to settle and cannot be removed from the light phase. Therefore, the separation performance is reduced if cell breakage occurs and the resulting fine cell debris causes problems in downstream processing.

After the separation, the dense phase is exposed to regions with a high potential for cell destruction. Cells in the ejected dense phase, flowing through the radial exit nozzles and impacting on the wall of the housing, are known to be stressed [Chan et al., 2006]. Furthermore, the Viscon nozzles, due to their small nozzle diameter of 0.6 Millimeters, are capable of introducing a significant amount of mechanical cell stress. The effect of cell breakage cannot be mimicked in laboratory centrifuges, due

to the resting fluid inside the centrifuge tubes. Centrifugation processes with shear-insensitive material have been successfully scaled up and down using the Sigma theory of equivalent settling area [Boychyn et al., 2004]. However, cases dealing with shear-sensitive material showed diverging results in the performance prediction, due to the destruction of cells and the consequent formation of debris.

2.2 Droplet Impact on Surfaces

2.2.1 Basic Considerations

The fluid mechanics of droplet impact has been investigated in detail by Mundo et al. with the aim of providing a criterion whether deposition or splashing occurs [Mundo et al., 1995]. When a droplet impinges on a dry surface, there are two possible outcomes: (i) the droplet may deposit on the surface and form a liquid film, or (ii) for higher impact velocities the droplet will splash and secondary droplets form.

A model describing the interaction between impacting droplets and the wall has been set up. Splashing or deposition occurs depending on the dimensionless droplet Reynolds and Ohnesorge numbers, defined as:

$$Re = \frac{\rho_{fl} \cdot v_{imp,\perp} \cdot D_{drop}}{\mu_{fl}} \quad Oh = \frac{\mu_{fl}}{\sqrt{\rho_{fl} \cdot \sigma_{fl} \cdot D_{drop}}} \quad (2.1)$$

The (empirical) critical curve delimiting the splashing and deposition regimes is shown in Figure 2.2 and can be expressed as:

$$Oh_{crit} = 57.7 \cdot Re^{-1.25} \quad (2.2)$$

2.2.2 Cell Stress Associated with Droplet Impingement

Wang et al. investigated the impact-induced cell mechanical stress profile in a cell suspended in a droplet. The mechanical stress was characterized in terms of stress, acceleration, and maximum shear strain component [Wang et al., 2008]. Their work was motivated by bio-material direct-writing technologies. A typical simulation result is shown in Figure 2.3. They described the cell by individual particles and analyzed the stresses on each of these particles. They found that the von Mises stress level is in the order of 10^5 [Pa] and that the peripheral particles were subjected to a higher stress level than the inner particles. Unfortunately, they were not able to record the total energy the cells dissipate when impacting on the surface. They conclude that their stress is one order of magnitude lower than necessary to break up yeast cells (critical stress around 70 [MPa]), however high enough for mammalian cells. Most important, they found that the cells in a droplet impacting on a dry surface experience a three-

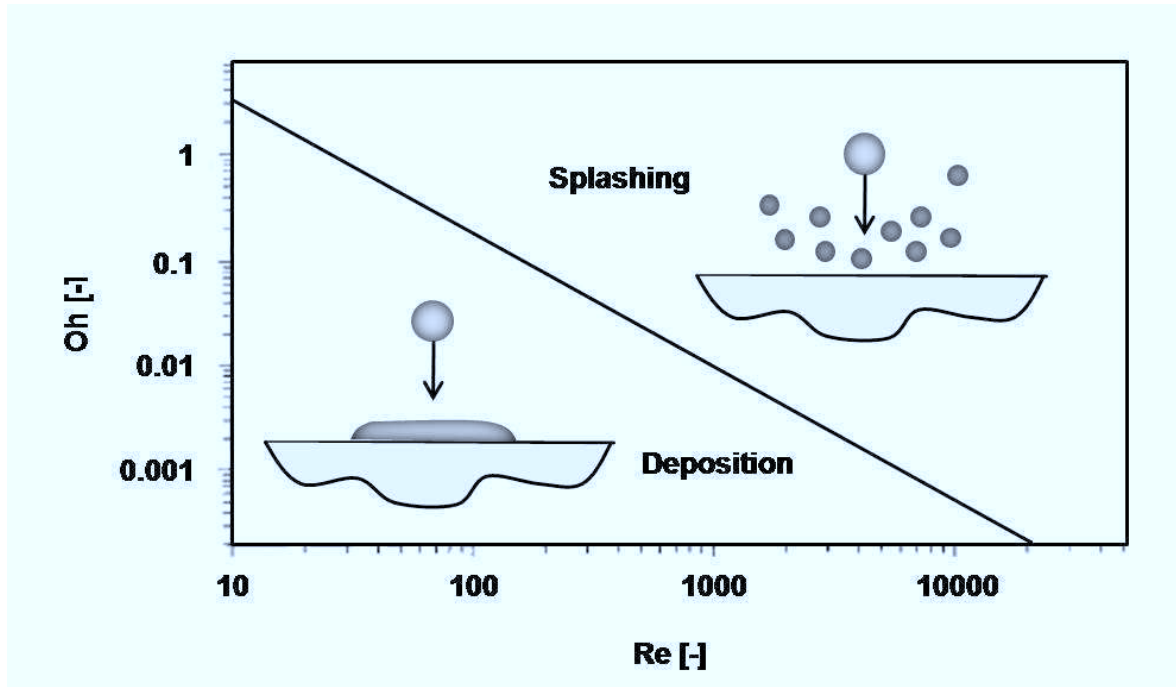


Figure 2.2: Droplets deposition model: critical curve (schematically, after [Mundo et al., 1995])

times higher maximum von Mises stress compared to the case when a liquid layer is present on the surface.

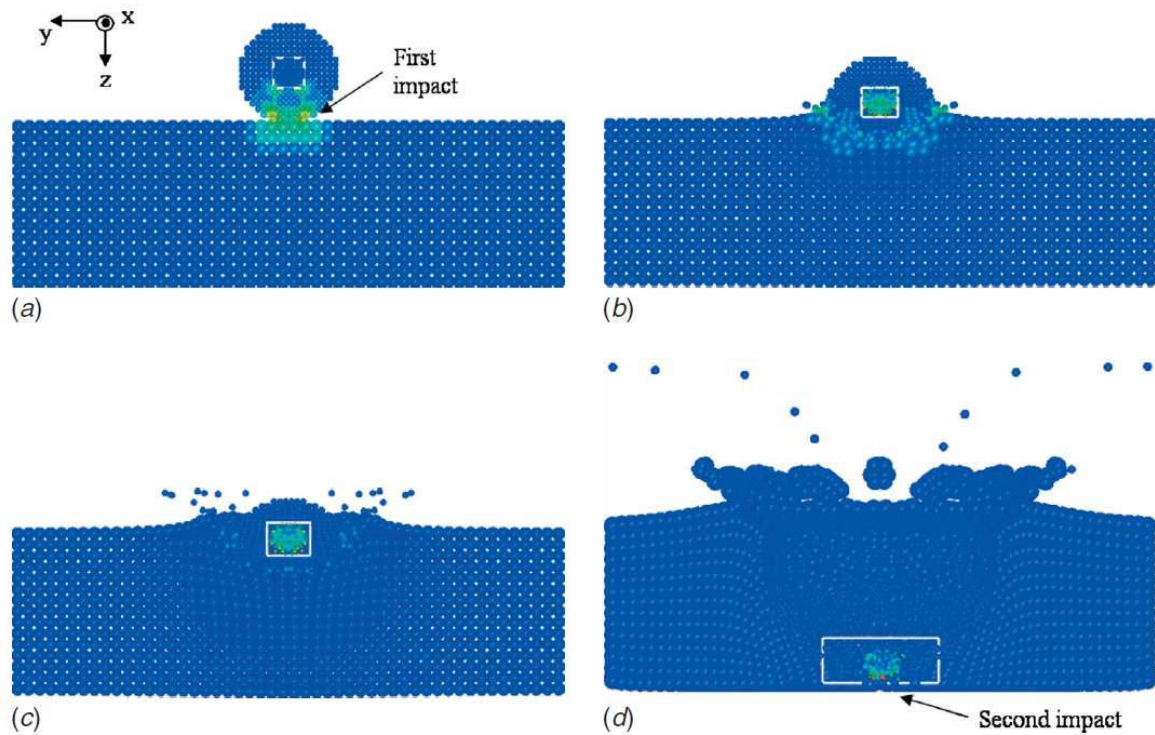


Figure 2.3: Droplet with suspended cells impacting on a liquid layer [Wang et al., 2008]

Cense et al. investigated the effect of impacting water droplets on a bio-film experimentally as well as using numerical simulations [Cense et al., 2006]. They tried to scale the stresses and the impact pressure with the Bernoulli pressure ρU^2 . They also found that stresses are significantly reduced (i.e., by a factor of maximum 6 in case of a ratio between the layer thickness and the droplet radius of 0.2) when a water film is present on the surface.

Hartley and Julien investigated raindrop impact using numerical models [Hartley and Julien, 1992]. They also performed experiments in the laboratory to validate the numerical results, where they found good agreement between the calculations and the experiments. The measured peak boundary shear stresses in the raindrops exceeded $10 [N m^{-2}]$.

2.3 Scale-Down Approaches for Disc Stack Separators

Pilot-Scale Disc Stack Centrifuges

The smallest commercially available scale for disc stack separators is the pilot scale, which still requires a significant amount of feed material typically above $10 [l]$ [Maybury et al., 1998]. Scale-down approaches have been conducted by blocking active discs or using blank discs and reducing the space of the settling region, which can reduce the amount of feed material needed by a factor of 4 to 10 [Maybury et al., 2000]. In case of a running production plant, approaches with an altered configuration of the separator for experiments are not favorable, since they are connected to production halts. Also, the amount of shear stress, which is experienced by the suspended cells, cannot be controlled in pilot-scale disc stack centrifuges. Hence, it is not recommended to perform a scale-down using these centrifuges, and we have excluded this possibility in our subsequent analysis.

Laboratory Scale Centrifuges

The work of Maybury et al. describes the approach of using a laboratory centrifuge to mimic the performance of a pilot scale disc stack centrifuge [Maybury et al., 2000]. The operating parameters of the laboratory centrifuge have been determined according to the conditions in the pilot-scale apparatus using the Sigma theory of equivalent settling area. In the Sigma theory of equivalent settling area, the settling performance of different apparatuses is considered to be equal, if the ratio $Q/\Sigma C$ is the same for each machine. Here, Q denotes the volumetric flow rate through the separator and Σ is the equivalent settling area. C is the correction factor for non-ideal flow (see Equation (2.3)). For a laboratory-scale batch centrifuge, the volumetric flow rate is replaced by $Q = V_{lab}/t_{lab}$, where V_{lab} is the volume of the suspension to be processed and t_{lab} is the

duration of centrifugation.

$$\frac{Q_{ds}}{C_{ds} \cdot \Sigma_{ds}} = \frac{V_{lab}}{t_{lab} \cdot C_{lab} \cdot \Sigma_{lab}} \quad (2.3)$$

The results have been compared by means of the clarification efficiency, which was determined by measurements of the optical density of the supernatant. The experiments of Maybury et al. showed accurate predictions of the clarification performance for polyvinyl acetate particles and yeast cell debris [Maybury et al., 2000]. However, the performance for the shear-sensitive protein precipitates was over predicted. Cell destruction increases the amount of fine particles, which settle slower, and therefore reduce the performance of the centrifuge. Since the fluid in laboratory centrifuges is resting relative to the tubes, shear effects are minimal and cell destruction is negligible. This is the reason for the over-prediction of the clarification performance for the shear-sensitive protein precipitates. Additionally, it was found that the acceleration and deceleration phases during the centrifuging process of the laboratory scale centrifuge have to be considered in the calculation of the operating parameters of the laboratory centrifuge. Settling already occurs during the acceleration and deceleration phase, which contributes to the total time particles can settle in the centrifuge. This effect has a strong influence on short centrifuging times.

Shear-Device and Laboratory Scale Centrifugation

Based on the performance prediction using a laboratory centrifuge, Boychyn et al. modified the process by adding a shear device to mimic the disruption of cells occurring in the entrance region of a pilot scale multichamber-bowl centrifuge [Boychyn et al., 2001]. The shear device consisted of a rotating disc in a cylindrical chamber (diameter of 40 [mm]) with changeable height elements. The configurations of a rotating disc (30 [mm] diameter, 1 [mm] thickness) with a chamber height of 10 [mm] and a rotating cylinder (30 [mm] diameter, 31 [mm] thickness) with a chamber height of 40 [mm] have been analyzed by them. The rotating parts have been made of aluminium alloy coated with a layer of PTFE, which have been mounted on a stainless steel shaft. A battery driven motor (Graupner Speed 500 BB Race, UK) was used to power the rotating objects providing 6 different speeds through changes of voltage. Air has been removed from the chamber through entrance and exit holes, which have been sealed during operation. The energy dissipation rate has been chosen as the parameter for the correlation with the cell destruction. This was motivated by the good results in scale-up and scale-down of mechanically stirred reactors. The operating parameters have been determined according to the results of their computational fluid dynamics (CFD) simulations of the entrance region of the separator. Also, they performed CFD simulations for the shear device. A high Reynolds number k-epsilon turbulence model

has been used by them. The feed flow was considered as a gas-liquid system, which was described by an unknown two-phase model. The simulated region was a quarter of the geometry, due to the symmetry of the baffles in the inlet region.

Cell destruction has been compared by measuring the particle size distribution (PSD) with a particle sizer (Elzone 280 PC, Particle Data UK Ltd.), a dynamic light scattering instrument (Zetasizer 3000, Malvern Instruments) and the clarification after centrifugation with optical density measurements (Beckman DU 650 spectrophotometer).

The results showed that the shear device lead to a shift towards smaller sizes in the particle size distribution. It was shown that the tip speed has a major effect on the clarification performance. However, changes of the residence time in the chamber (5, 10, 20 [s]) showed no significant influence on the results for the clarification. The chamber with a cylinder and a lower maximum tip speed, could not reproduce the cell damage in the continuous centrifuge. Therefore, the chamber with the rotating disc has been used for performance prediction, because this device was able to produced energy dissipation rates similar to those produced in the continuous centrifuge. With a matching maximum energy dissipation rate (flooded conditions were assumed in the centrifuge), the prediction based on the chamber with the rotating disc were excellent. Thus, a relative clarification of 45% was predicted compared to the actual value of 44%. Under non-flooded conditions the extrapolation of the performance prediction gave a clarification of 27% with an actual value of 30%. As can be seen, in both cases the performance prediction was in good agreement with the actual performance of the multichamber-bowl centrifuge.

In addition, Boychyn et al. compared the performance prediction of a multichamber-bowl centrifuge, a disc stack separator and a CARR Powerfuge TM using the shear device [Boychyn et al., 2004]. The maximum occurring EDR in the simulations of the multichamber-bowl centrifuge was $6.0 \times 10^5 [W kg^{-1}]$ for flooded and $12.0 \times 10^5 [W kg^{-1}]$ for non-flooded conditions, $14.0 \times 10^5 [W kg^{-1}]$ for the CARR Powerfuge and $2.0 \times 10^5 [W kg^{-1}]$ for the disc stack separator. The performance prediction based on the shear device was in good agreement. Using the shear device lead to a difference in the clarification performance prediction of approximately -6% for the disc stack centrifuge. Without the shear device, performance was +55% over-predicted for this separator. The performance prediction for the multichamber-bowl centrifuge and the CARR Powerfuge could be improved from up to 400% (without shear device) to about -10% difference (with the shear device) to the actual value on full scale.

Capillary Rheometer

Chan et al. investigated cell destruction of *E.coli* caused by the impact of a liquid jet and droplets on surfaces with an Instron capillary rheometer [Chan et al., 2006]. Cell breakage has been calculated using Equation (2.4), with the concentration of released

intracellular components in the sample C_{Sample} , in the feed C_f and the maximum amount measured after homogenization C_h .

$$Cell\ Breakage = \frac{C_{Sample} - C_f}{C_h - C_f} \quad (2.4)$$

A stainless steel surface has been positioned at a distance of 90 [mm] to the capillary exit, which was used as the impact surface for experiments with changed exit velocity in the range of 0 to 85 [$m\ s^{-1}$]. The results showed a linear relationship between the cell breakage and exit velocity, with a maximum of approx. 7% cell breakage for the highest exit velocity of 85 [$m\ s^{-1}$].

Additionally the effect of the impact distance to the exit of the capillary has been analyzed. For a constant exit velocity of 49 [$m\ s^{-1}$] the distance has been varied from 10 – 300 [mm]. Starting from 10 [mm], the resulting cell breakage showed an increase up to the maximum of 3.5% located at 100 [mm] distance and decreased from there to about 0% at 300 [mm] distance.

3 Proposed Scale-Down Approach for Sandoz' Disc Stack Separator

Based on the results from the approaches detailed in Subsection 2.3, a shear device is a necessary component in the laboratory-scale process for shear sensitive materials. A laboratory centrifuge, due to the circumstance that the particles settle in a resting fluid phase relative to the tubes, shows negligible cell destruction. Therefore, a laboratory centrifuge alone can not produce the shift in the PSD caused by the breakage of cells.

The ultra scale-down approach mentioned in the literature, however, uses only millilitre quantities. This is not suitable for this project, since the amount of feed material required for further downstream processing in a chromatography column is up to 6 liters. Therefore, the approaches discussed in literature have to be modified and adapted for larger quantities of feed material. Batch operation of the shear device (i.e. filling, processing, emptying) would be connected with numerous load changes for liter quantities, and therefore this is unfavorable. Larger sized rotating disc shear devices show disadvantages connected with the difficulties to achieve locally well defined conditions throughout the machine (see Subsection 6.1). Using the shear device in a continuous process is a possibility for a flexible design which allows handling of different amounts of bio-material up to several liters.

The proposed ultra scale-down approach is shown in Figure 3.1. It includes a peristaltic pump, which transports the fluid from a reservoir through the shear device with the rotating disc to a collection vessel. Then, the sheared material is centrifuged in a laboratory centrifuge. The operation can be controlled manually or, if desired, from a central control unit (i.e., additional equipment, such as a personal computer, would be necessary for this purpose).

The operating parameters of the shear device are determined by computational fluid dynamics simulations. The parameters are adjusted such that the conditions in the

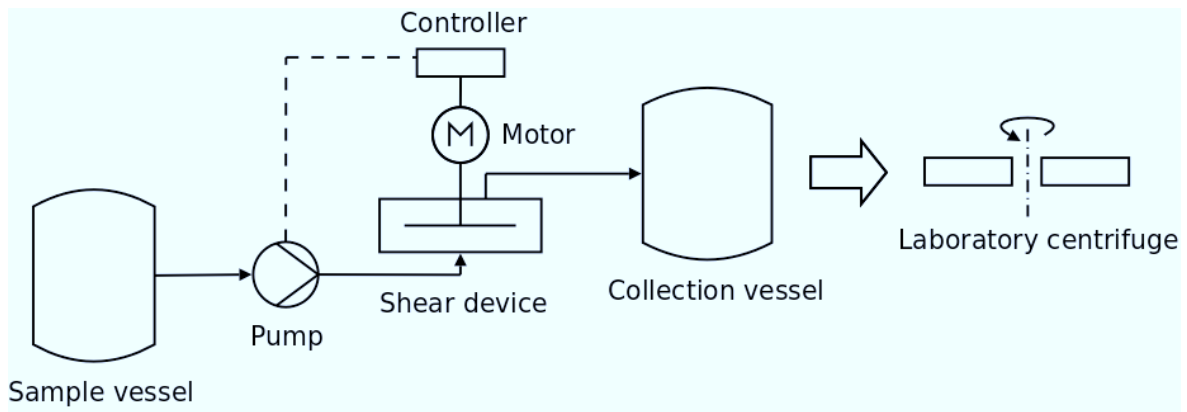


Figure 3.1: Illustration of the proposed ultra scale-down process

shear device match the conditions in the full-scale separator. As a criterion for the stress level comparison, the energy dissipation rate (EDR) has been chosen, since it has been used successfully in other cases (compare Subsection 2.3), and is easy to derive from the simulated flow field.

After shearing, the settling step of the disc stack separator is mimicked by a laboratory centrifuge. Its operating parameters are determined by using the Sigma theory of equivalent settling area.

Mimicking the cell destruction in the dense phase following the separation step (i.e., the radial exit nozzles and the Viscon nozzles) is not included in the ultra scale-down process. The effects related to the radial exit nozzles (i.e., the droplet impact on the housing of the disc stack separator) are complex and difficult to approach. The occurring conditions are not known, which makes the design of a proper device difficult. A CFD analysis of the problem would be a topic on its own, exceeding the possibilities in this work. Therefore it would be a suitable field for research in the future. However, to take the cell breakage in the radial exit nozzles and the Viscon nozzles into account, is possible by a second run of the dense phase material through the shear device with adapted parameter settings. These parameter settings for the radial exit and Viscon nozzles can be determined, for example, by experimental calibration studies using the shear device developed during this project.

4 Simulation of Multiphase Flow

Computational fluid dynamics (CFD) is a scientific approach to calculate the flow, as well as heat and mass transfer including chemical reactions in a certain domain. The underlying partial differential equations are well known since the early 19th century, but the process of solving them for geometrically complex domains remains a challenge. The Navier-Stokes equation describing fluid flow for incompressible fluids with constant density ρ and viscosity μ is given in Equation (4.1) and the corresponding equation of continuity in Equation (4.2) [Bird et al., 2002]. The velocity \mathbf{u} and the gravitational acceleration \mathbf{g} is given in vector notation. Using specialized mathematical algorithms, the governing equations are solved numerically.

$$\rho \left(\frac{\partial \mathbf{u}}{\partial t} + \mathbf{u} \cdot \nabla \mathbf{u} \right) = -\nabla p + \mu \nabla^2 \mathbf{u} + \rho \mathbf{g} \quad (4.1)$$

$$\nabla \cdot \mathbf{u} = 0 \quad (4.2)$$

The basic structure of a CFD analysis starts by defining the flow domain and introducing a geometrical model using appropriate software. Then, the computational mesh (i.e., small sub-volumes that completely fill the flow domain) is generated inside of this geometry. In this step, the requirements of the chosen simulation model in terms of spatial resolution have to be taken into account. To define the physical conditions at the boundaries or to connect the mesh with other domains, proper boundary conditions have to be defined. Boundary conditions include the conditions for the velocity, pressure and the turbulence field. After the setup of the simulation parameters, the simulation can be started with a chosen numerical model. Monitoring the solution gives information on the progress of the simulation, and when the solution is converged, it can be stopped and the results can be analysed. The term "converged" here refers to a time-invariant solution in the case of a steady-state simulation. For transient simulations, one typically speaks of a "developed" solution instead of a "converged" one. "Developed" refers to a situation where the time-averaged quantities in an unsteady simulation do not depend anymore on the range of time over which averaging is performed. Analyzing the results, often referred to as post-processing, is the final step of a CFD analysis. Depending on the results obtained in the post-processing step, some steps of the described process may have to be repeated to achieve an acceptable solution.

4.1 Available Simulation Concepts

Turbulence is a physical effect, leading to chaotic and unsteady flow conditions. In addition, turbulence is an inherently three-dimensional effect. Thus, predicting turbulent

flow requires, in principal, three-dimensional flow studies.

The equations describing turbulent flow are well known and solving requires different amounts of computational resources. In the following paragraphs we detail on the principles behind the most common approaches for simulating turbulent flow. The knowledge behind each of these approaches is fundamental for this study, because the flow in the devices to be studied will be turbulent. Also, the prediction of the local energy dissipation rate may depend on the approach used to describe turbulent flow.

Direct Numerical Simulation

In the Direct Numerical Simulation (DNS) approach, the Navier-Stokes equations are solved directly, without modelling the turbulent flow [Ferziger and Peric, 2002]. This leads to the most accurate result, but requires the spatial and temporal resolution to be fine enough to resolve the smallest eddies, i.e., down to eddies dominated by viscous forces known as the Kolmogoroff scale. The required computational resources are the limits for this approach to be practicable. Flow domains that can be studied by DNS have typically a size of a few Millimeters and therefore cannot, with some exceptions, reflect industrial flow situations.

Large Eddy Simulation

In contrast to the DNS approach, the large eddy simulation (LES) approach uses models for the small-scale eddies. Therefore, LES does not require a mesh as fine as for DNS. Large eddies, however, are fully resolved [Ferziger and Peric, 2002]. The larger eddies contain the major part of the kinetic energy of the flow. LES is used where DNS is too expensive or the computational domain is too large for the use of DNS. Nevertheless, the computational effort is still very high for LES, because these simulations are unsteady, i.e., also require a temporal resolution of turbulent motion. Typical simulation times for a single LES are in the order of several days to a few weeks. Therefore, LES studies are still not commonly used for standard engineering tasks and remain a tool for scientific research.

Reynolds Averaged Navier-Stokes

The RANS (Reynolds Averaged Navier-Stokes) approach is a simulation concept for engineering purposes, where the complex turbulent flow behaviour is essentially time-averaged [Ferziger and Peric, 2002]. Turbulence is modelled by a separate set of equations, so-called "turbulence models". A prominent example for such a model is the two equation k-epsilon model. This approach reduces the computational effort significantly compared to DNS and LES. Depending on the case to be studied, specific turbulence models can be chosen to achieve better results.

The RANS approach has been chosen for our simulations, since the geometries to be analyzed are too complex for DNS, and LES would require too much simulation time. Hence, the governing equations solved in our simulations are the Reynolds-averaged, steady-state continuity and momentum equation shown in Equation (4.4) and Equation (4.5) [Bird et al., 2002]. The equations are given for the x-direction, but the equations for the other directions are similar. Equation (4.3) shows the so-called Reynolds decomposition, where the turbulent behaviour of the velocity u_x is translated into a mean velocity \bar{u}_x and a fluctuation u'_x from it. Then, insertion of the Reynolds decomposition in the Navier-Stokes equations leads to the RANS equations. Details of the turbulence models used in our simulations to enhance the results can be found in Subsection 4.2.3.

$$u_x = \bar{u}_x + u'_x \quad (4.3)$$

$$\frac{\partial \bar{u}_x}{\partial x} + \frac{\partial \bar{u}_y}{\partial y} + \frac{\partial \bar{u}_z}{\partial z} = 0 \quad (4.4)$$

$$\begin{aligned} \frac{\partial}{\partial t} \rho \bar{u}_x = & -\frac{\partial}{\partial x} \bar{p} - \left(\frac{\partial}{\partial x} \rho \bar{u}_x \bar{u}_x + \frac{\partial}{\partial y} \rho \bar{u}_y \bar{u}_x + \frac{\partial}{\partial z} \rho \bar{u}_z \bar{u}_x \right) - \\ & - \left(\frac{\partial}{\partial x} \rho \overline{u'_x u'_x} + \frac{\partial}{\partial y} \rho \overline{u'_y u'_x} + \frac{\partial}{\partial z} \rho \overline{u'_z u'_x} \right) + \mu \nabla^2 \bar{u}_x + \rho g_x \end{aligned} \quad (4.5)$$

4.2 Computational Methods and Models

4.2.1 Numerical Methods for Solving the Governing Equations of Fluid Flow

Finite Differences Method

The finite differences method (FDM) uses a numerical approximation of the partial differential equations [Ferziger and Peric, 2002]. Therefore, the domain is split into a grid, and the calculations are made according to numerical approximations of the differentiation operator on this grid. By doing so, the differential equations are converted to a system of difference equations, which can be solved explicit or implicit. The FDM shows disadvantages in solving cases of complex geometries. It is a method typically used for DNS because it is easy to apply for simple geometry. Also, the equations can be solved much faster because the grid is typically structured. The latter aspect is essential for solving the governing equations: individual points in a structured grid can be easily accessed and do not need a special mesh addressing algorithm searching for neighboring points in the grid.

Finite Element Method

Dividing the volume into a discrete number of elements leads to the finite element method (FEM) [Ferziger and Peric, 2002]. The main difference to other methods is,

that a weight function is used for minimizing the residuals in the approximation of the partial differential equations. Grid refinement can be easily made by splitting the elements. A disadvantage is the difficulty to find efficient solution methods, since this approach uses unstructured grids. The FEM approach is mainly used for solid body calculations, e.g. forces and stress in structural elements.

Finite Volume Method

Based on the FDM, the finite volume method applies a grid on the domain, and divides it into a finite number of control volumes [Ferziger and Peric, 2002]. The partial differential equations are converted to a system of algebraic equations for each of the control volumes. The control volumes define the boundaries of the domain, and the use of unstructured meshes is possible in this approach. Due to the applicability of this method to volumes of arbitrary shape, this method is widely used in computational fluid dynamics.

The FVM is used for our simulations, due to its flexibility with respect to the shape of the computational domain and widespread use CFD. Details of the FVM can be found in [OpenCFD Ltd, 2008].

4.2.2 Particle Tracking Method

The determination of energy dissipation rate (EDR) profiles of different shear device geometries was based on a particle tracking method (PTM). Particle tracking is a method for solving multiphase flow problems with a typically low hold-up of the disperse phase. If the flow field is not affected by the motion of the particles, one speaks of a "one-way" coupling approach. Thus, only particles experience the flow field, but the flow field does not experience the particles. This approach is suitable for extremely low hold-up of the disperse phase and small density differences between the involved phases. Both criteria are thought to be fulfilled for the problem handled within this work.

In the PTM using one-way coupling, particles are injected into a fixed flow field. The particles have been defined to have a negligibly small density difference to the continuous phase, and therefore perfectly follow the flow field. To mimic turbulent fluctuations, random movement of the liquid phase has been introduced. The added fluctuating velocity component delivering randomness is calculated according to the Lagrangian stochastic deterministic (LSD) model, which is related to the turbulent kinetic energy of the flow field (see Subsection B.1).

The exposure of the particles to flow conditions can be recorded during the simulation, hence leading to a data set available to process, e.g., an EDR profile.

4.2.3 Turbulence Models

In order to close the RANS equations described in Subsection 4.1, one needs to introduce an appropriate turbulence model. This model is then solved simultaneously with the RANS equations.

Depending on the Reynolds number and the accuracy of the near-wall resolution, one can distinguish between high- and low-Reynolds-number turbulence models. Both turbulence models have been used for our simulations and are detailed in the following paragraphs.

High-Reynolds-number turbulence models are used for high Reynolds number flow, i.e., a high degree of turbulence, and use wall functions to model the flow in the boundary layer. The first cell near the wall in the computational grid should have a y^+ value of about 30 or above. For details and definition of the y^+ value refer to [Schlichting and Gersten].

Standard k-epsilon Model

The standard k-epsilon model is a widely used two-equation model for turbulence. In this model, the transport equations for the turbulent kinetic energy k and its dissipation ϵ are solved. It shows robust behaviour and is suitable for initialization of complex simulations [Martens, 2008]. Additionally, the standard k-epsilon model is good for parameter studies. The results for complex flow situations with high pressure gradients and for flows that have separated from the walls of the computational domain are inaccurate. The flow close to walls is modeled, instead of calculated, with the standard wall function. Hence, this model is not suitable to resolve the flow close to a boundary.

The transport equations for k and ϵ are shown in Equation (4.7) and Equation (4.8), where k and ϵ are calculated according to Equation (4.6) [Hoffmann and Chiang, 2000]. The turbulent viscosity is modelled according to Equation (4.9). Equation (4.10) shows the production of k . The constants have been derived empirically and are given in Equation (4.11).

$$k = \frac{1}{2} [\overline{u_x'^2} + \overline{u_y'^2} + \overline{u_z'^2}] \quad \epsilon = \nu_t \overline{\left(\frac{\partial u_i'}{\partial x_i} \right) \left(\frac{\partial u_i'}{\partial x_i} \right)} \quad (4.6)$$

$$\rho \frac{Dk}{Dt} = \frac{\partial}{\partial x_j} \left[\left(\mu + \frac{\mu_t}{\sigma_k} \right) \frac{\partial k}{\partial x_j} \right] + P_k - \rho \epsilon \quad (4.7)$$

$$\rho \frac{D\epsilon}{Dt} = \frac{\partial}{\partial x_j} \left[\left(\mu + \frac{\mu_t}{\sigma_\epsilon} \right) \frac{\partial \epsilon}{\partial x_j} \right] + C_{\epsilon 1} P_k \frac{\epsilon}{k} - C_{\epsilon 2} \rho \frac{\epsilon^2}{k} \quad (4.8)$$

$$\mu_t = \rho C_\mu \frac{k^2}{\epsilon} \quad (4.9)$$

$$P_k = -\overline{\rho u'_i u'_j} \frac{\partial u_j}{\partial x_i} \quad (4.10)$$

$$C_{\epsilon 1} = 1.44, \quad C_{\epsilon 2} = 1.92, \quad C_\mu = 0.09, \quad \sigma_k = 1.0, \quad \sigma_\epsilon = 1.3 \quad (4.11)$$

RNG k-epsilon Model

The RNG (Re-Normalization Group) k-epsilon model is a variation of the standard k-epsilon model with a modified equation for ϵ . The transport equation for k is similar to the standard k-epsilon model. The equations of the RNG k-epsilon model and the constants are analytically derived. The RNG k-epsilon model is suitable for complex flow conditions with a high pressure gradient, rotation and local transition [Martens, 2008].

Realizable k-epsilon Model

The realizable k-epsilon model is similar to the standard k-epsilon model. The equations for k and ϵ are the same as in the standard k-epsilon model (see Equation (4.7) and Equation (4.8)), but the coefficients have been modified. Taking into account mathematical requirements for the Reynolds-stress makes this turbulence more realistic than the standard k-epsilon model. The applicability is similar to the RNG k-epsilon model. Simulation of free jets is also possible.

4.2.4 Launder-Sharma Low-Reynolds-Number Turbulence Model

The Launder-Sharma low-Reynolds-number model has been used to describe the flow around the rotating disc in the shear device and in the contraction zone of the Viscon nozzles. Being a low-Reynolds-number turbulence model, the flow in the boundary layers close to walls is resolved. For an accurate resolution of the flow conditions the y^+ value for the computational mesh should be below 1.

The governing equations are given in Equation (4.12) to Equation (4.15) [CFD-Online, 2010]. $C_{1\epsilon}$, $C_{2\epsilon}$, C_μ , σ_k and σ_ϵ are constants (see Equation (4.16), and f_μ , f_1 , f_2 are damping functions (see Equation (4.17)). D and E are relevant for solving k and ϵ down to the viscous sublayer, and are active close to solid boundaries only (see Equation (4.18)).

$$\frac{\partial}{\partial t} (\rho k) + \frac{\partial}{\partial x_j} \left[\rho k u_j - \left(\mu + \frac{\mu_t}{\sigma_k} \right) \frac{\partial k}{\partial x_j} \right] = P - \rho \epsilon - \rho D \quad (4.12)$$

$$\frac{\partial}{\partial t} (\rho \epsilon) + \frac{\partial}{\partial x_j} \left[\rho \epsilon u_j - \left(\mu + \frac{\mu_t}{\sigma_\epsilon} \right) \frac{\partial \epsilon}{\partial x_j} \right] = (C_{1\epsilon} f_1 P - C_{2\epsilon} f_2 \rho \epsilon) + \rho E \quad (4.13)$$

$$\mu_t = C_\mu f_\mu \rho \frac{k^2}{\epsilon} \quad (4.14)$$

$$P = \tau_{ij}^{turb} \frac{\partial u_i}{\partial x_j} \quad (4.15)$$

$$C_\mu = 0.09 \quad C_{1\epsilon} = 1.44 \quad C_{2\epsilon} = 1.92 \quad \sigma_k = 1 \quad \sigma_\epsilon = 1.3 \quad (4.16)$$

$$f_\mu = \exp\left(\frac{-3.4}{(1 + Re_t/50)^2}\right) \quad f_1 = 1 \quad f_2 = 1 - 0.3\exp(-Re_t^2) \quad Re_t = \frac{k^2}{\nu\epsilon} \quad (4.17)$$

$$D = 2\nu \left(\frac{\partial\sqrt{k}}{\partial y}\right)^2 \quad E = 2\nu\nu_t \left(\frac{\partial^2 u}{\partial y^2}\right) \quad (4.18)$$

4.3 Geometry and Grid Generation

The software *Cubit 11.1* by Sandia National Laboratories has been used for the generation of the computational meshes through out the project [Sandia National Laboratories, 2008]. It has a graphical user interface (GUI) as well as a text interface. Additionally, the program allows to run a sequence of commands from a journal file. Editing these text files simplifies the manipulation of details in a large project.

The open-source CFD simulation software *OpenFOAM 1.5* [OpenCFD Ltd, 2008] includes a tool for the generation of the computational mesh called *blockMesh*. This mesh generation tool is based on text file manipulation and has no graphical user interface. Therefore the creation of complex geometries is very difficult, especially geometries consisting of non-flat surfaces. *blockMesh* has been used in the initial stages of this project. It has, however, not been used for final simulation runs.

4.4 Numerical Solution of the Governing Equations

For the simulations in this project, the open-source CFD simulation package *OpenFOAM 1.5* has been used [OpenCFD Ltd, 2008]. *OpenFOAM 1.5* is maintained by the commercial company OpenCFD Ltd. It is the centerpiece of the calculations in this work. The software package includes predefined solvers, but leaves the possibility to modify the code or write own algorithms depending on the case to be simulated. The drawback of this open-source software package, compared to commercial software, is the lack of a systematic documentation of individual solvers.

4.5 Post-Processing

Post-processing of the simulation data has been done using *paraView 3.3.0*. This tool is included in the *OpenFOAM 1.5* software package, and allows to plot specific data sets of the simulation results in the geometry.

For additional calculations of data received as output from the simulations, the mathematical program *Octave* has been used [Octave, 2008].

Gnuplot has been used to prepare graphs of the results [Gnuplot, 2008].

5 Results for Sandoz' Disc Stack Separator

5.1 Operating Parameters and Geometry

Sandoz' disc stack separator is a disc stack separator with automatic continuous discharge (Westfalia HFA 65-01-477). The range of the used operating parameters for Sandoz' disc stack separator is listed in Table 5.1 [Piskernik, 2008]. According to this window of operation, the ultra scale-down process has been designed.

Mass flow rate	$[kg\ h^{-1}]$	1,000 – 2,500
Rotational speed	$[rpm]$	6,800 – 8,000
Temperature range	$[^{\circ}C]$	8 – 20

Table 5.1: Window of operation of the disc stack separator

5.2 Simulation of the Inlet Pipes

Fluid flow through the piping system consisting of several bent elements may result in a rotating, three-dimensional flow at the inlet of the separator. To correctly simulate the flow in a certain domain, an appropriate definition of the inlet conditions is necessary. In case of the disc stack separator, defining the inlet conditions is less important due to the high rotational speed in the entrance region. However, we decided to simulate the flow in the pipe system attached to the inlet of the separator in order to determine how the velocity and turbulence profile looks like. Also, this simple flow situation was an excellent test case for the turbulent flow solver *simpleFoam*.

5.2.1 Generation of the Geometry

The inlet pipe mesh has been separated into two sections (named section1 and section2) to simplify the generation of the mesh and to avoid an excessively large mesh. The basic geometry is displayed in Figure 5.1 and Figure 5.2. The diameter of the inlet pipes has been 34.8 [mm] up to the wider connection to the disc stack separator with a diameter of 44 [mm]. Except for the pressure indicator, the other elements built on to the pipes have been neglected (e.g., inspection windows, etc.). Both meshes have been created with the software *Cubit*, and are designed for a high-Reynolds-number turbulence model. The meshes consisted of 177k cells for section1 and 170k cells for section2. The average y^+ value has been 28 for section1 and 20 for section2.

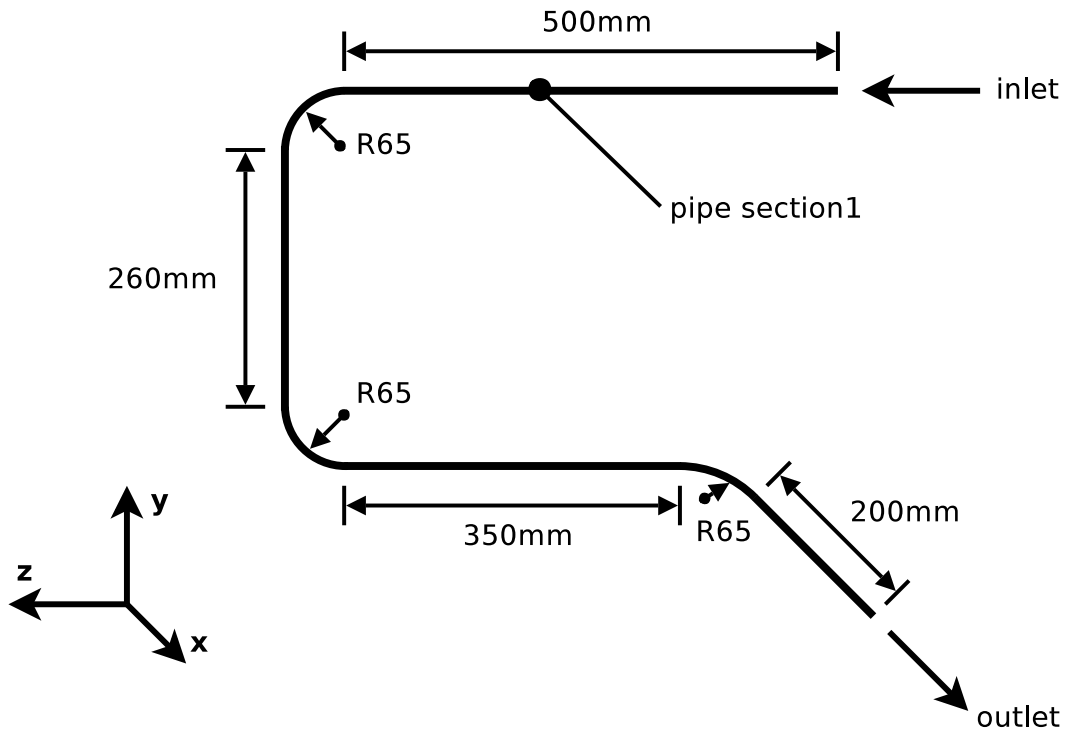


Figure 5.1: Geometry of the first section of the inlet pipe system (section1)

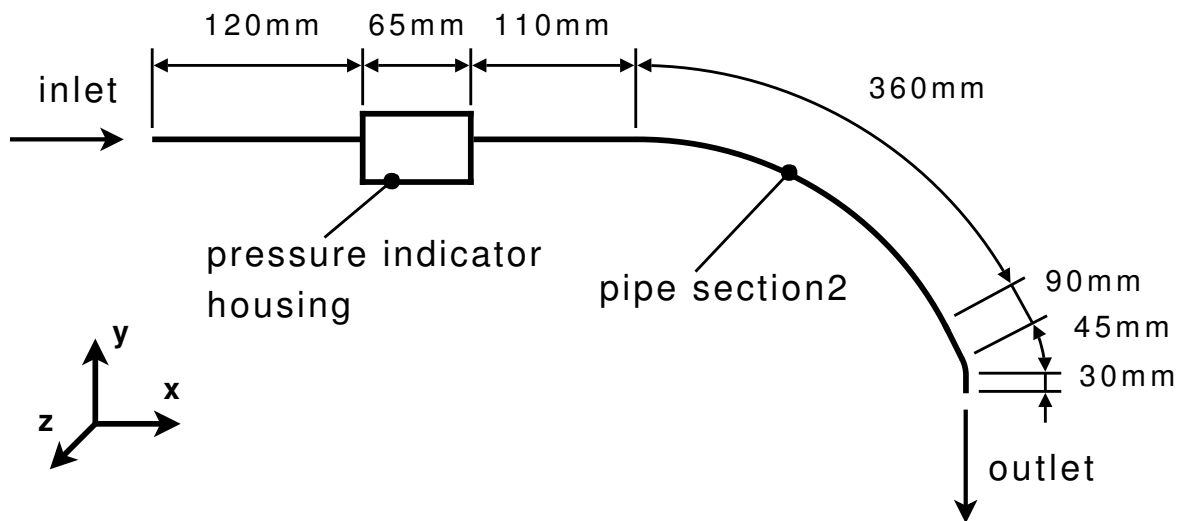


Figure 5.2: Geometry of the second section of the inlet pipe system (section2)

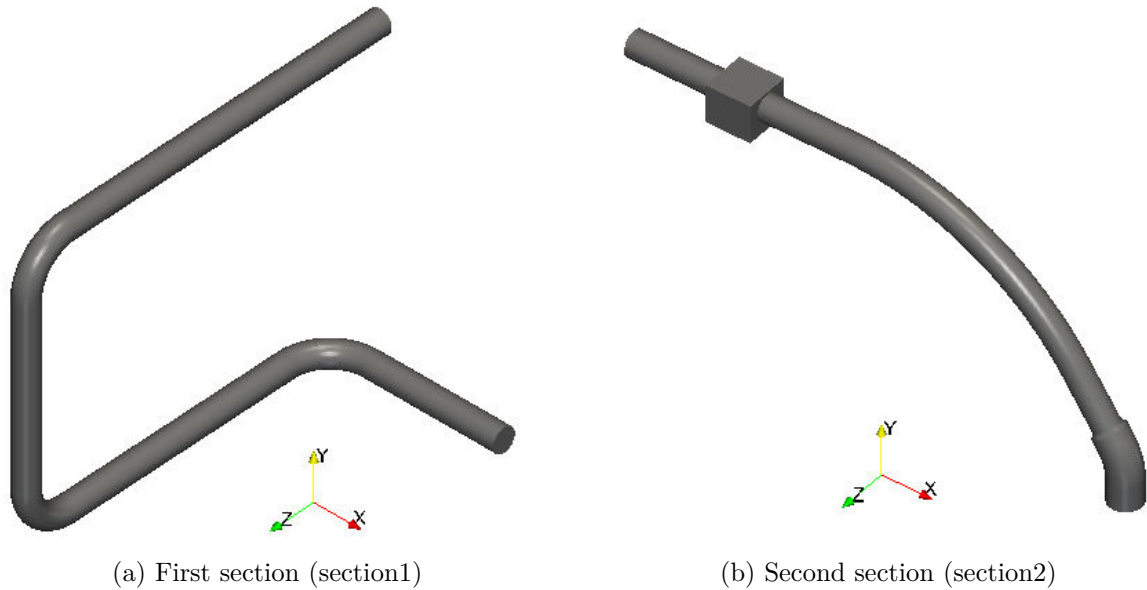


Figure 5.3: Surface plot of the computational mesh of the inlet pipe system

5.2.2 Results of the Simulation

Flow field simulations with the *simpleFoam* solver have been conducted using the standard k-epsilon turbulence model. The velocity at the inlet of section1 has been set to be uniform and equal to $0.73 [m s^{-1}]$. This corresponds to a feed mass flow rate into the disc stack separator of $2,500 [kg h^{-1}]$. Following the fluid flow through the piping system, section1 has been simulated first. The boundary field of the outlet of section1 has been introduced as the boundary condition for the inlet of section2 using *OpenFOAM's* utility *mapFields*.

The resulting velocity distribution at the outlet of section2 (i.e., the inlet to the inlet pipe of the disc stack separator) is given in Figure 5.4. It can be seen that the higher velocity region is concentrated on the right half of the plot and the highest occurring velocity is of the order of $0.75 [m s^{-1}]$. A calculation of the uniform outlet velocity gives $0.46 [m s^{-1}]$. Due to the high rotational speed in the separator bowl of up to $8,000 [rpm]$, the effect of the calculated non-uniform velocity in the inlet pipe is thought to be negligible for the flow in the separator.

5.3 Simulation of the Full-Scale Separator

5.3.1 Grid Generation

Simulations in a complex, three-dimensional geometry typically require a high amount of computational resources. In this case, early tests to generate and mesh the full scale separator geometry pointed out several critical aspects. The grid of the entrance region of the disc stack separator turned out to be very difficult to refine due to its complex

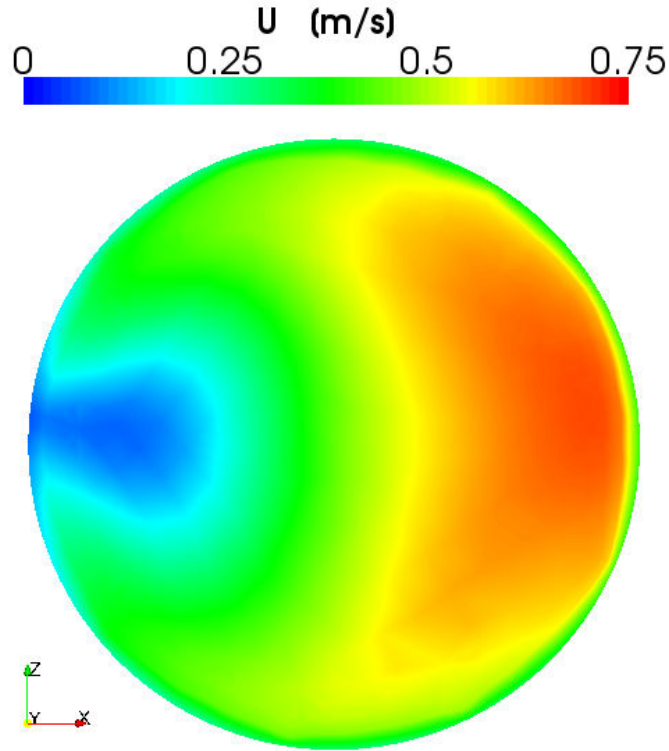


Figure 5.4: Plot of the magnitude of the velocity at the outlet of the second section of the inlet pipes (section2)

shape (see Figure 5.5). Thus, the automated refinement algorithm in *Cubit 11.1* did not lead to an acceptable result for this region. Therefore, refining was done manually for this region and also for most of the other sections of the geometry.

Meshing the full separator with a fine grid would lead to a huge number of grid cells, which is directly connected to an unacceptably high amount of simulation time. Therefore, an attempt to reduce the grid size has been made. Due to the periodic increments of the baffles in the upper region of the separator (compare Figure 5.5), a slice of 60° already includes all features of the separator geometry (see Figure 5.6). This periodicity of the geometry does not necessarily mean that a perfectly periodic flow pattern within the full separator is given as well. However, it can be anticipated that the flow in each region between the baffles is similar. Also, in our work the focus is on the fluid flow close to the baffles in the inlet region of the separator. It can be expected, that this flow is less influenced by an eventually non-periodic flow pattern in the separator. Thus, it is thought that a slice of 60° is sufficient to give accurate results of the flow in the separator. Consequently, such a slice was taken as the basis for our simulations.

Implementing a slice of a symmetric geometry in a simulation requires the definition of a periodic boundary condition. The documentation for a cyclic patch boundary in *OpenFOAM* was insufficient to start with the mesh generation in *Cubit*. As a first step,

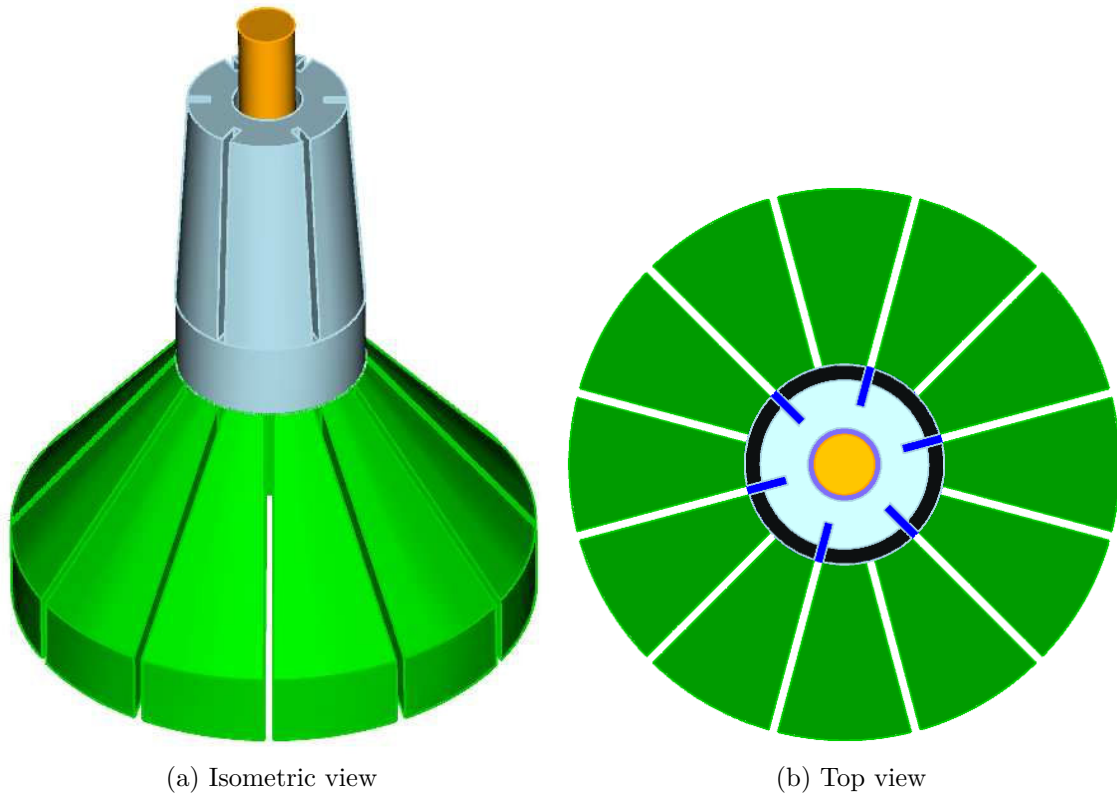


Figure 5.5: Schematic drawing of the full-scale separator geometry

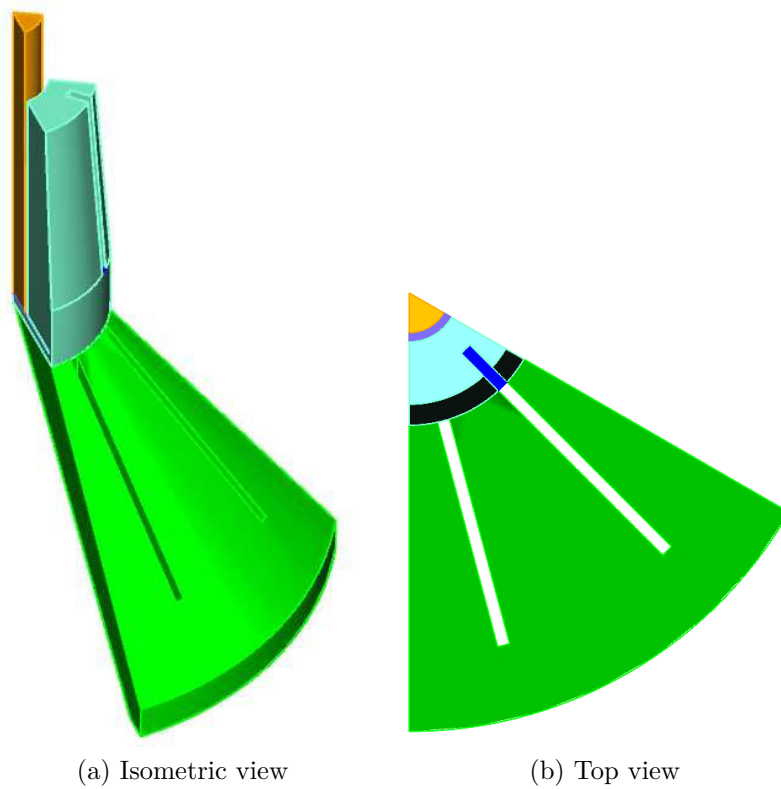


Figure 5.6: Schematic drawing of the periodic slice of the separator geometry

the correct structure and formatting of the geometry and mesh had to be determined, since the *MRFsimpleFoam* solver of *OpenFOAM* requires the definition of a rotating and a stationary zone of the mesh. In comparison to the shear device simulation, the geometry of the disc stack separator had to be split up into several smaller volumes, hence the right ordering of these volumes is crucial for the simulation to work.

Preparation of the Cyclic Patch

The cyclic boundary condition consists of one patch including all cell faces of the corresponding sub-volumes (i.e., cells) making up the mesh. Tests showed that using a cyclic boundary conditions requires a certain order of cell faces within the patch. The correct ordering format had to be found, and then, realized during the mesh generation.

Tests to determine the correct face ordering were performed using a simple cylinder. Figure 5.7 illustrates the ordering pattern of cell faces in the patch. The cell faces in the second half of the cyclic patch (shown in green) have to be ordered in a mirrored fashion of the first half (shown in red). *Cubit*, however, has no tool to influence the order of cell faces within a patch. To ensure the generation of the required ordering of cell faces, the volume has to be meshed as a first step. Then, the mesh on the surface of the second half of the cyclic patch has to be deleted. Using the copy function of *Cubit*, the surface mesh including the correct face ordering is transferred to the surface of the second half of the cyclic patch. With the copied surface the volume is meshed again. The mesh then has the correct face ordering. Finally, the periodic surfaces have to be added to the cyclic patch.

Furthermore, a certain ordering of adding surfaces to the cyclic patch is required if the sides of the patch consist of multiple surfaces. Therefore, another test case including three volumes has been set up. In Figure 5.8 the ordering of multiple surfaces for the cyclic patch is illustrated. Adding surfaces to cyclic patches has to be done by starting to add all surfaces of one half (A, B, C) followed by the surfaces of the second half (a, b, c). The sequence of adding surfaces is crucial and has to be done in the same manner for both halves (e.g., adding C, B, A and then c, b, a). The *OpenFOAM* solver *MRFSimpleFoam* needs separate cyclic patches for the rotating and the stationary cell zone. Therefore two cyclic patches had to be defined in the manner described above.

Details of the Computational Mesh

The turbulence model used for the simulation was the RNG k-epsilon model due to its low requirement on near-wall mesh resolution. Thus, the RNG k-epsilon model does not require a sufficiently fine mesh to resolve the laminar boundary layer near the wall. Also, the RNG k-epsilon model is suitable for rotational flows. Hence, this high-Reynolds-number turbulence model was a possible choice for simulation of the

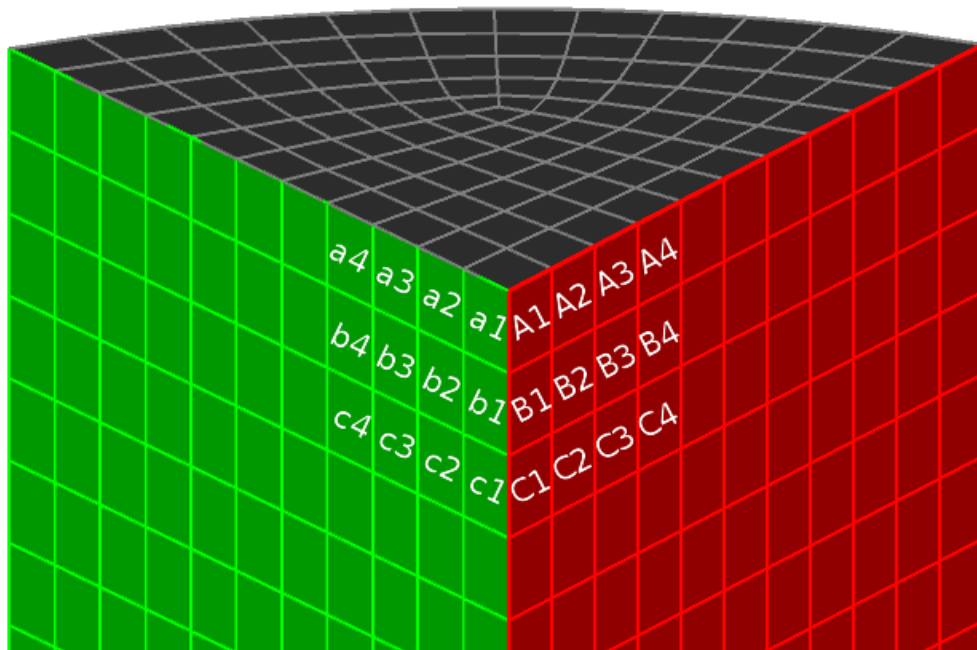


Figure 5.7: Ordering pattern of cell faces for the cyclic patch boundary conditions required by *OpenFOAM*

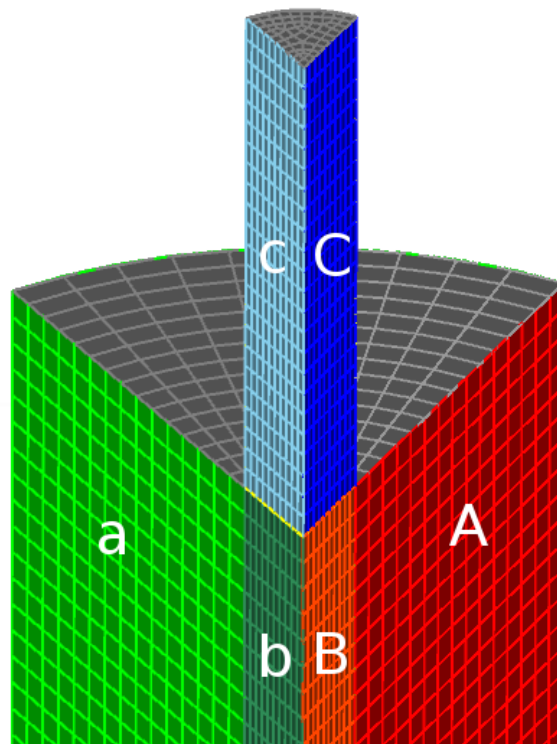


Figure 5.8: Ordering pattern of multiple surfaces in a cyclic patch required by *OpenFOAM*

flow in the entrance region of the disc stack separator.

After several attempts to mesh the geometry, the mesh has been altered and refined in several steps to find an acceptable solution. The simulated geometry had to be slightly changed from the geometry shown in Figure 5.6, due to problems in defining the boundary conditions at the outlet. The final geometry includes the riser holes to the disc stack region at the inside of the disc stack separator bowl (see Figure 5.9). Figure 5.9b shows the inlet patch colored in green and the outlet patch of the simulation domain colored in red. The different colored blocks in between indicate the individual volumes used for mesh generation. By refining the mesh in specific volumes and by using gradients in the mesh spacing, a suitable grid with an acceptable number of cells was generated. It has to be taken into account, that for a three-dimensional geometry, the number of cells increases by a factor of 8 if the mesh resolution is doubled. Several grids have been generated starting with a size of 126k cells up to the final mesh consisting of 2.6M cells. For meshes of this size, a 3.6Ghz Quad-core PC was running already for several days alone to export the data file for the mesh with a size of 436 MB.

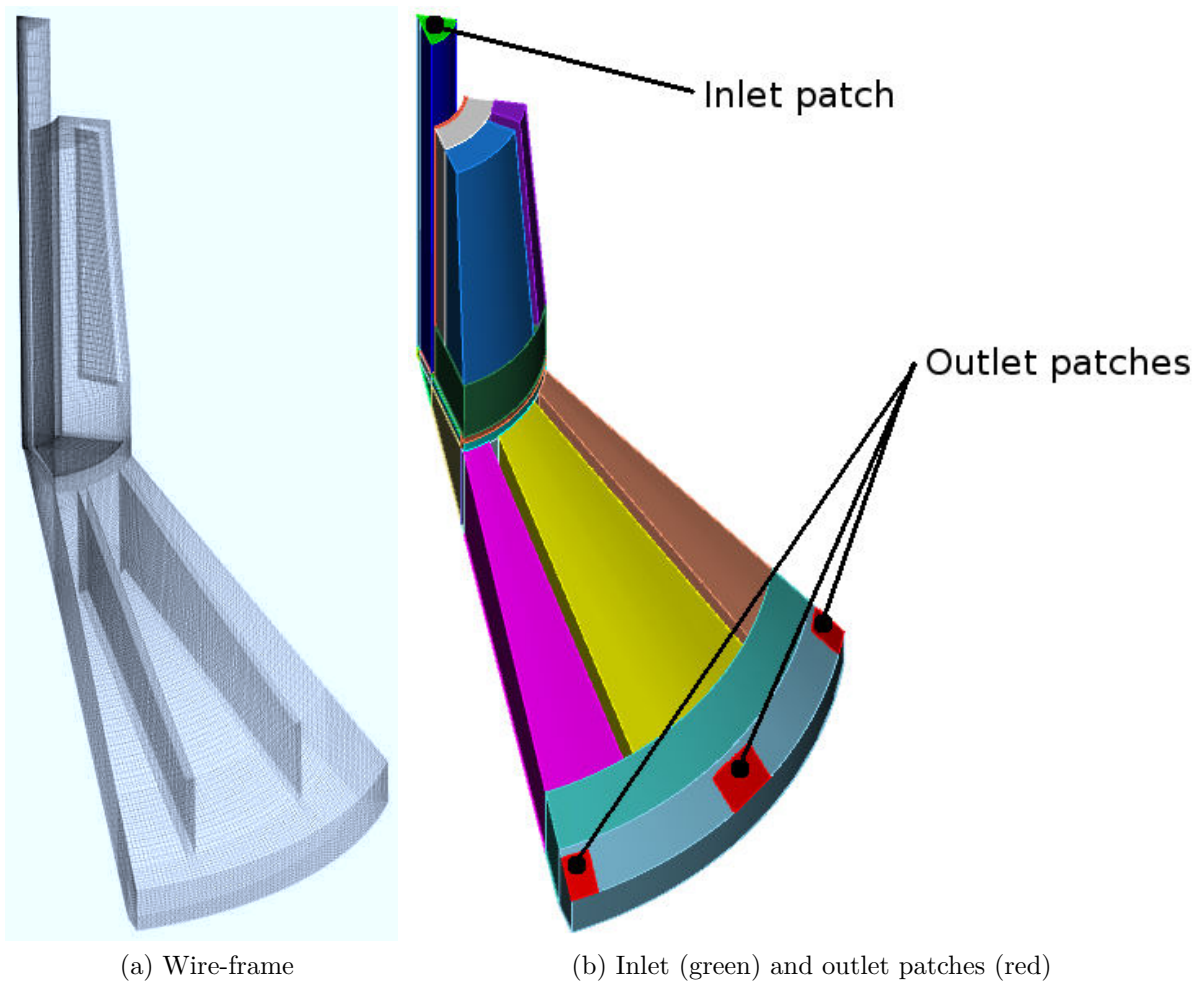


Figure 5.9: Full-scale separator mesh with 800k cells

Simulation	ω_{DS} [rpm]	\dot{m}_f [kg h ⁻¹]
1	6,800	1,000
2	6,800	2,500
3	8,000	1,000
4	8,000	2,500

Table 5.2: Simulated operating conditions of the disc stack separator

5.3.2 Boundary Conditions for the Simulations

The boundary conditions for the full-scale separator have been set according to the given window of operation from Sandoz (Table 5.1). Simulations for the minimum and maximum values of the operating conditions have been performed (see Table 5.2).

In the following, the calculations for the rotational speed and the conditions at the inlet of the separator are detailed for the maximal operating parameters.

Rotational Speed

The rotational speed after conversion to SI-units is:

$$\omega_{DS} = 8,000 \text{ [rpm]} = 837 \text{ [rad s}^{-1}\text{]} \quad (5.1)$$

Velocity

The geometry of the full-scale separator has been reduced to a slice of 60°. This is one of the reasons why the velocity field determined in the inlet pipes simulation (see Subsection 5.2) cannot be used for the simulation of the flow in the separator. Therefore, the mean inlet velocity has been used as the inlet boundary condition. The mean inlet velocity can be calculated from the feed mass flow rate $\dot{m}_f = 2,500 \text{ [kg h}^{-1}\text{]}$. The pipe diameter at the inlet is $D_{in} = 28.5 \text{ [mm]}$. With the fluid density of $\rho_{fl} = 1,000 \text{ [kg m}^{-3}\text{]}$, the inlet velocity v_{in} is:

$$\dot{V}_{in} = \frac{\dot{m}_f}{\rho_{fl}} = 2.500 \text{ [m}^3 \text{ h}^{-1}\text{]} \quad (5.2)$$

$$A_{in} = \frac{D_{in}^2 \pi}{4} = 637.9 \text{ [mm}^2\text{]} \quad (5.3)$$

$$v_{in} = \frac{\dot{V}_{in}}{A_{in}} = 1.089 \text{ [m s}^{-1}\text{]} \quad (5.4)$$

For all walls the no slip boundary condition has been set, i.e., a velocity of 0 [m s⁻¹] at the walls has been specified. At the outlet patch, a zero-gradient boundary condition for the velocity has been used.

Pressure

The pressure in *OpenFOAM* is expressed as a relative pressure, being the pressure divided by the density. Thus, the unit of the pressure is $[m^2 s^{-2}]$. The outlet pressure has been fixed to 0 $[m^2 s^{-2}]$. The remaining patches have been set to have a zero-gradient pressure boundary condition.

Turbulence

The turbulence models used were the standard k-epsilon model for the initialization of the flow field, and the RNG k-epsilon model for production runs. Since a two-equation turbulence model has been used, ϵ and k had to be set at the boundaries. For both values the zero-gradient condition has been set on all walls. ϵ has been set to 20 $[m^2 s^{-3}]$ and k to 1 $[m^2 s^{-2}]$ as the initial condition at the inside of the computational domain. At the inlet and outlet patches, ϵ and k have been set to zero-gradient.

5.3.3 Results

Preliminary Simulations

Preliminary simulations were performed using a mesh consisting of 800k cells (a wire-frame model of this mesh is shown in Figure 5.9). For these simulations the boundary conditions have been set to the maximum values of the operating window (the rotational speed has been set to 8,000 $[rpm]$ and the inlet mass flow rate to 2,500 $[kg h^{-1}]$). Only the standard k-epsilon model has been chosen for turbulence modelling. The simulation had the purpose to gain information about necessary enhancements with respect to the mesh resolution. The $y+$ value is a metric for the resolution of the mesh close to walls and depends on the flow conditions near the wall. For the high- Reynolds-number turbulence models, $y+$ should be 30 or slightly above in regions where an accurate solution is needed. In Table 5.3 the resulting $y+$ value for the 800k mesh is shown. The words "rotor" and "stator" refer to the rotating and static part of the mesh, respectively. Clearly, the results displayed in Table 5.3 indicate a too coarse mesh especially in the rotating part of the mesh.

	minimum	maximum	average
rotor	19	2,479	322
stator	32	314	125

Table 5.3: The values for $y+$ from the full scale separator mesh (800k cells)

In the following, screenshots of the results from the 800k mesh are illustrated. Figure 5.10 shows the absolute velocity (i.e., the velocity in a world-fixed coordinate system)

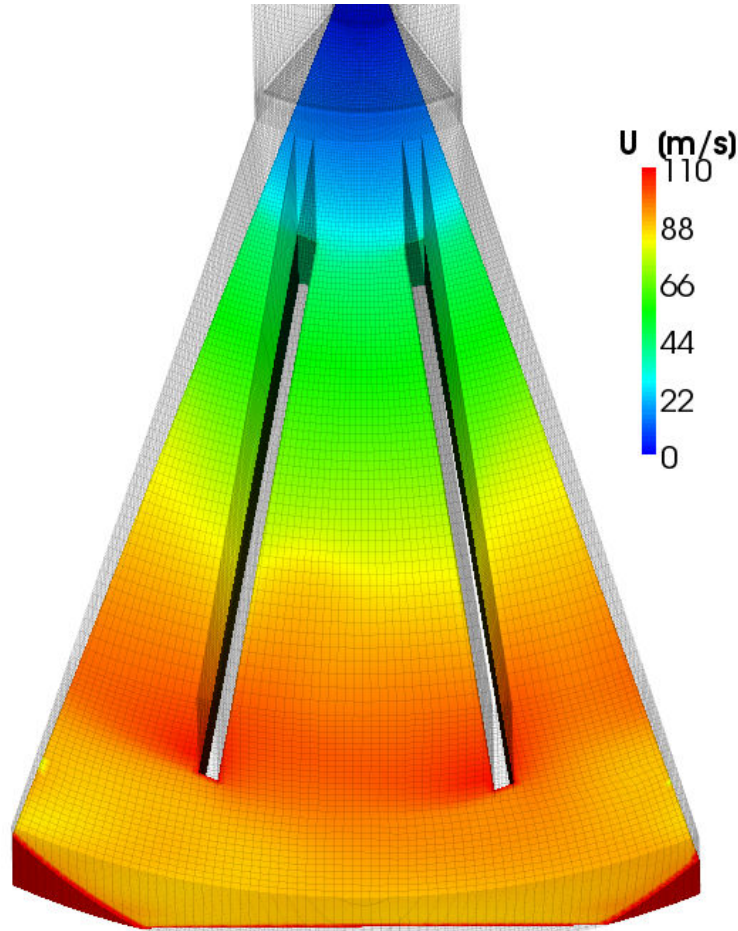


Figure 5.10: Velocity in the 800k cells mesh (plane cut through the baffled region of the separator)

and Figure 5.11 the separator-relative velocity (i.e., the rotational motion of the separator has been subtracted).

The separator-relative velocity of the fluid between the baffles is relatively low compared to the absolute velocity of the separator. This leads to comparably low energy dissipation rates in the region between the baffles (as can be seen in in Figure 5.12). The region of the highest occurring energy dissipation rate is located at the tip of the baffles with an EDR of the order of $1 \times 10^5 [W kg^{-1}]$. Also, we observed significant EDR in the region near the disc attached to the inlet pipe (data not shown). The EDR in this region was of the order of $6 \times 10^4 [W kg^{-1}]$.

Production Runs using a Refined Mesh

A mesh consisting of 2.6M cell showed a suitable range for the y^+ values compared to the 800k mesh (see Table 5.4). The y^+ value is still high in some regions, but it is expected that further refinement of the mesh would have no significant effect on the results. Further refinement would lead to a mesh size which would require excessive simulation time on a single core CPU. This is a limiting argument, since the

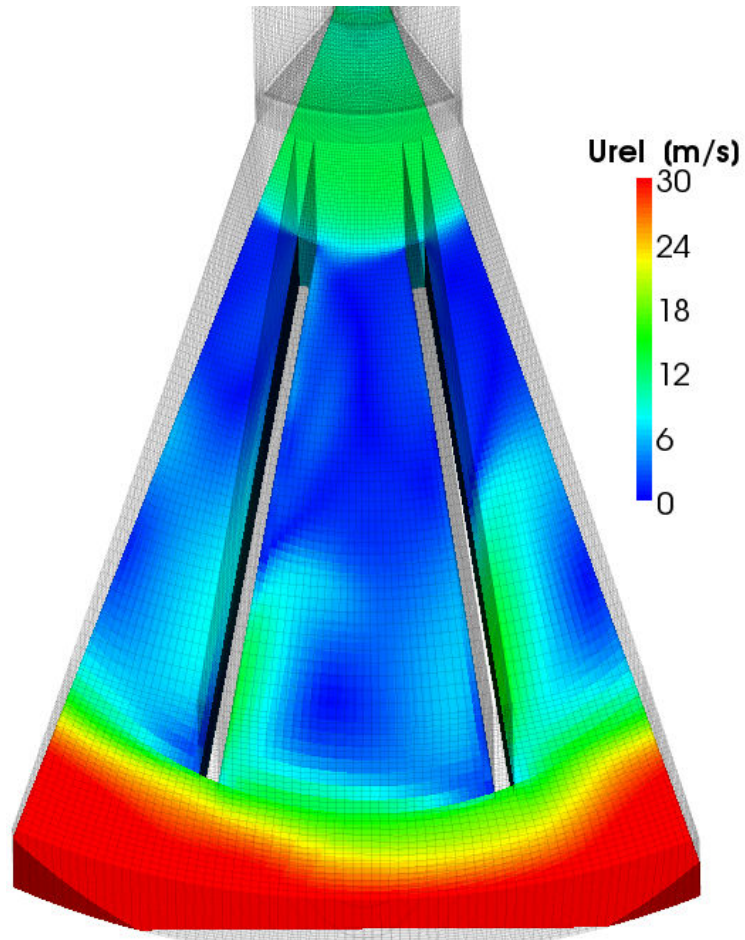


Figure 5.11: Relative velocity to the rotating walls in the 800k cells mesh (plane cut through the baffled region of the separator)

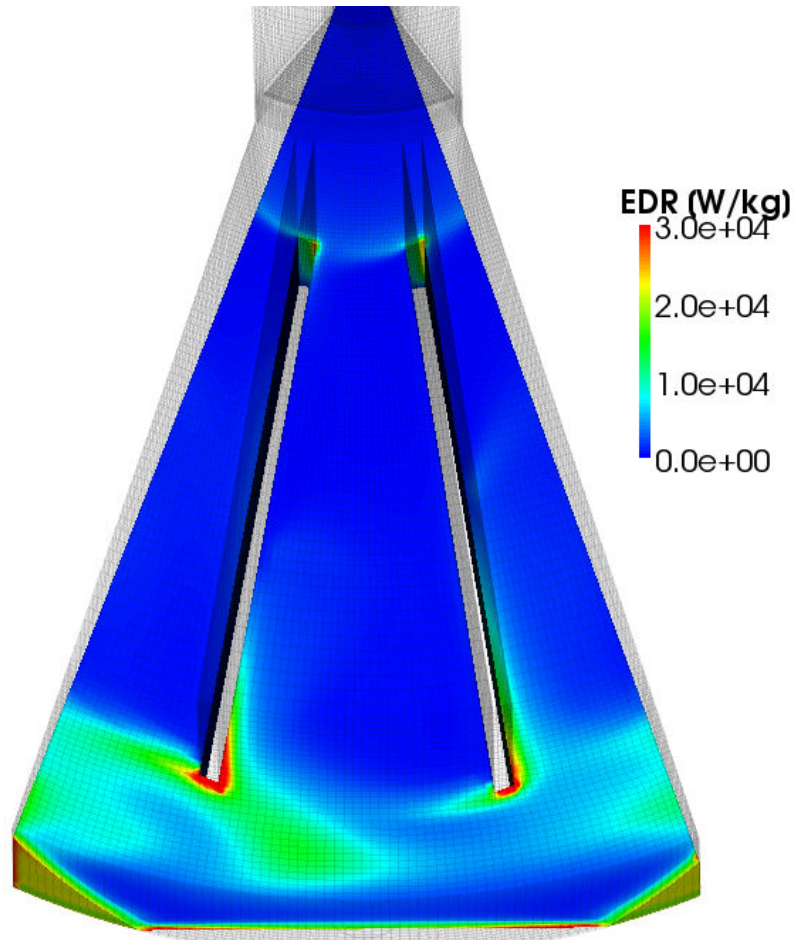


Figure 5.12: Energy dissipation rate (plane cut through the baffled region of the separator)

	minimum	maximum	average
rotor	7	1,265	180
stator	8	163	92

Table 5.4: $y+$ from the full scale separator simulation (2.6M cells, $\dot{m}_f = 2,500 [kg h^{-1}]$, $\omega_{DS} = 8,000 [rpm]$)

Simulation	ω_{DS} [rpm]	\dot{m}_f [kg h ⁻¹]	max.EDR (baffles) [W kg ⁻¹]	max.EDR (<i>global</i>) [W kg ⁻¹]
1	6,800	1,000	7.4×10^4	6.2×10^5
2	6,800	2,500	6.3×10^4	9.7×10^5
3	8,000	1,000	1.1×10^5	5.9×10^5
4	8,000	2,500	9.9×10^4	9.3×10^5

Table 5.5: Maximum energy dissipation rate in the separator (2.6M cell mesh)

MRFsimpleFoam solver is not designed for parallel use on multiple CPUs.

The results for the maximum energy dissipation rate of the simulations with the 2.6M cell mesh are summarized in Table 5.5. Figure 5.13 illustrates the EDR conditions in the entrance region. Two distinct regions of high EDR are visible: around the attached disc of the inlet pipe and at the outlet region. Figure 5.14 shows the EDR of the region around the attached disc, which is the region where the acceleration of the bio-material occurs. There, the highest EDR levels of the inner region are observed. It can be seen that at the location near the edges of the baffles a high EDR can be observed as well. Similar conditions are present at the outer edges of the baffles (see Figure 5.15). The region surrounding the outlet holes showed the highest EDR (max.EDR (*global*) in Table 5.5). This is due to the sharp corners in the mesh structure of the outlet patch, and the close distance to the outlet. The outlet patch had to be approximated as a rectangle, due to geometric limitations in the meshing process. Therefore, only the EDR of the inner region (max.EDR (baffles) in Table 5.5), reaching up to the outer edges of the baffles, has been considered as being a reliable result of the simulation.

Vector plots of the relative velocity vectors show regions of circulation between the baffles (see Figure 5.17). The results for the mesh containing 2.6M cells are similar to the mesh having 800k cells. This indicates a mesh-insensitive result.

As can be seen, the influence of the feed mass flow rate is insignificant. The major factor influencing the maximum EDR is the rotational speed of the separator. From these simulation results, it can be anticipated that this influence is super-linear, as expected.

However, the results showed significantly lower EDR than can be expected from literature data. In comparison, an EDR up to $10^6 [W kg^{-1}]$ occurred in pilot scale separators described in literature [Boychyn et al., 2004]. Thus, the statement from

Westfalia, that this type of disc stack separator with a hydro-hermetic feed system produces low stress level in the entrance region, can be confirmed.

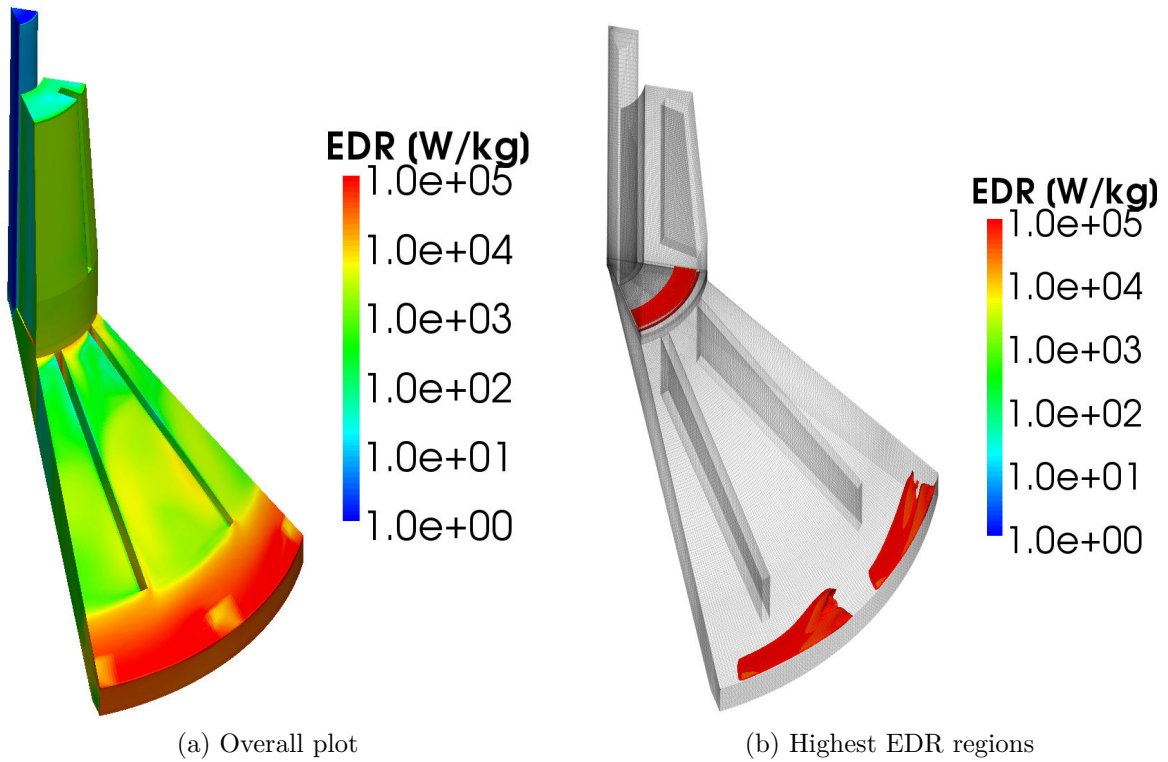


Figure 5.13: Plot of the EDR in the disc stack separator ($\omega_{DS} = 8,000 [rpm]$, $\dot{m}_f = 2,500 [kg h^{-1}]$, 2.6M cell mesh)

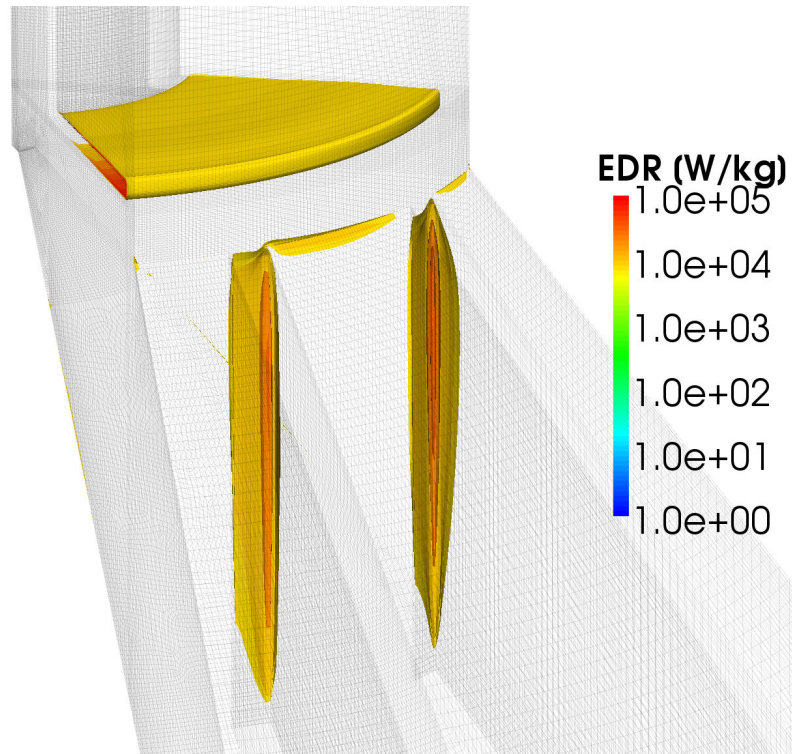


Figure 5.14: Plot of the EDR at the disc attached to the inlet pipe exit and at the edges of the baffles ($\omega_{DS} = 8,000$ [rpm], $\dot{m}_f = 2,500$ [kg h⁻¹], 2.6M cell mesh)

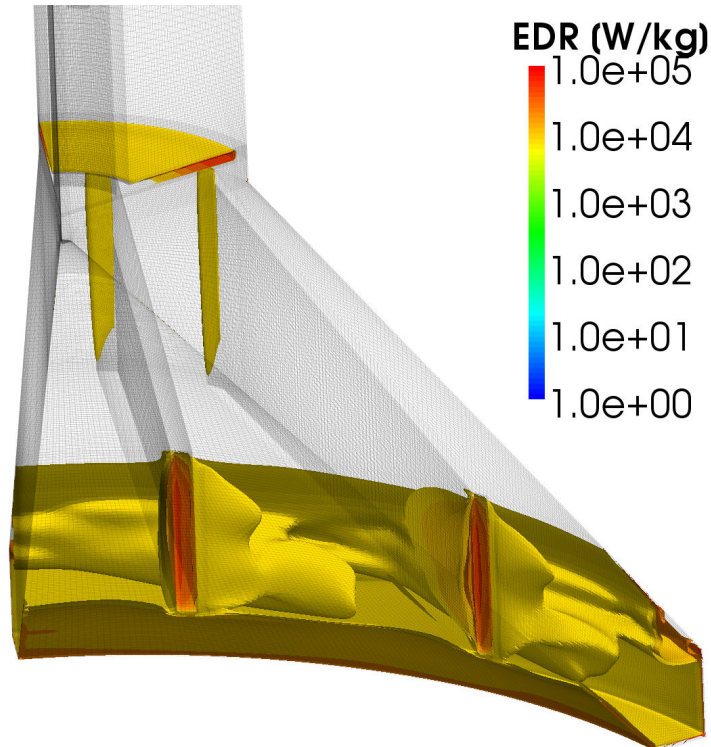


Figure 5.15: Plot of the EDR at the outer edges of the baffles ($\omega_{DS} = 8,000$ [rpm], $\dot{m}_f = 2,500$ [kg h⁻¹], 2.6M cell mesh)

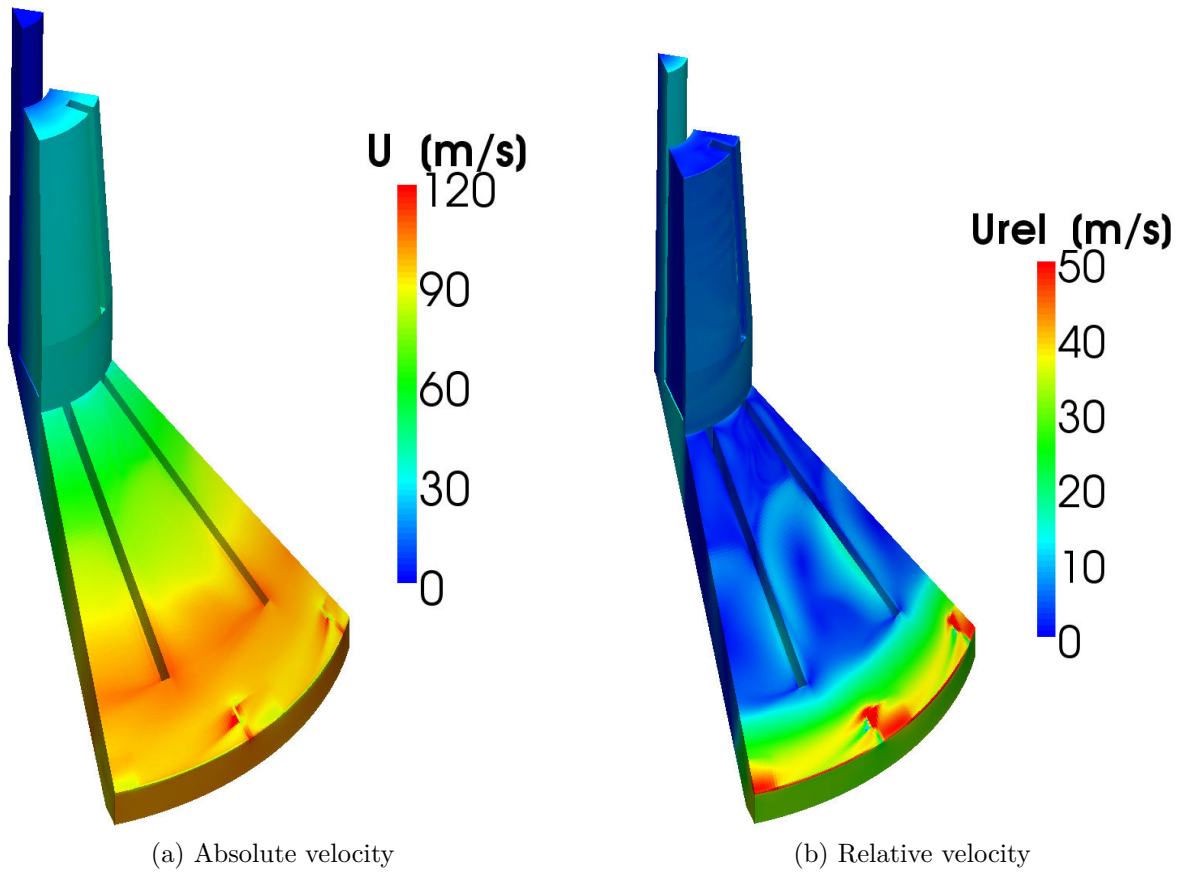


Figure 5.16: Plot of the magnitude of the velocity in the disc stack separator ($\omega_{DS} = 8,000$ [rpm], $\dot{m}_f = 2,500$ [$kg\ h^{-1}$], 2.6M cell mesh)

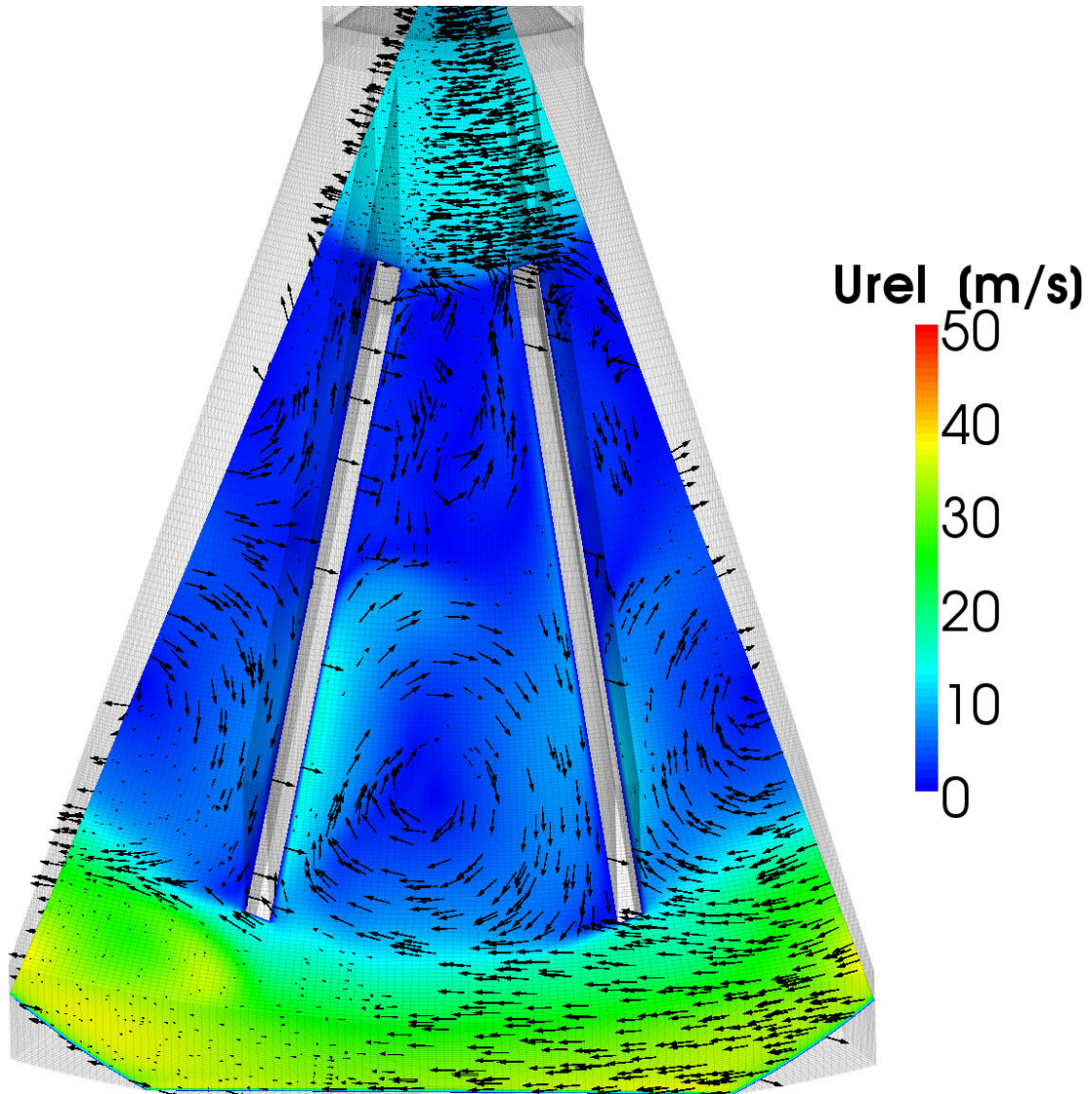


Figure 5.17: Plot of the velocity vectors of the relative velocity in the disc stack separator ($\omega_{DS} = 8,000$ [rpm], $\dot{m}_f = 2,500$ [kg h⁻¹], 2.6M cell mesh)

5.4 Viscon Nozzles

After the bio-material has passed the separation region of the disc stack separator, the dense phase is collected in the separator bowl and transported further through a two-way system (see Figure 2.1). One way is a continuous flow leading upwards through a separator-internal piping and passing through the so-called "Viscon" nozzles. After the Viscon nozzles, a peeling disc transports the material out of the apparatus via an exit pipe. The other way is leading through a radial discharge, which is hydraulically controlled (see Subsection 5.5).

The geometry of the Viscon nozzles is illustrated in Figure 5.18. The Viscon nozzles are described by Westfalia as being "viscosity controlled", and should allow constant discharge concentrations even for variations in the feed concentration. Scientific back-

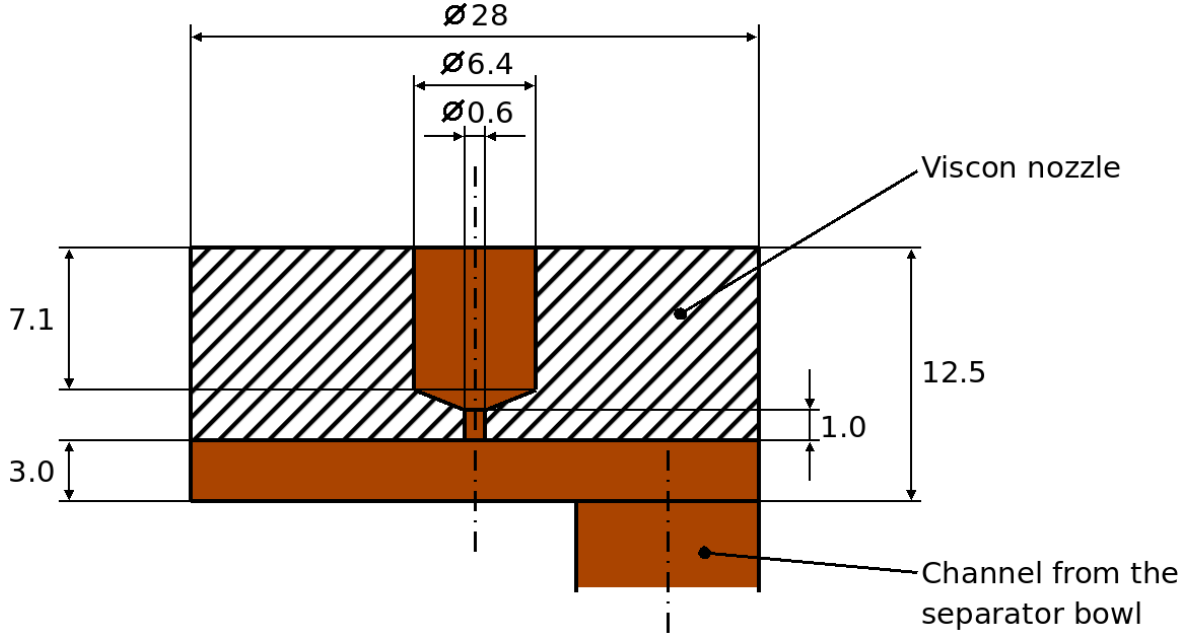


Figure 5.18: Schematic drawing of the geometry of the Viscon nozzles

ground describing the design of the Viscon nozzles was not available. Since the channels through the Viscon nozzles are narrow, the fluid flow is considered to have a strong impact on cell destruction. Therefore, the flow conditions in these nozzles have been analysed.

5.4.1 Estimation of the Energy Dissipation Rate in the Viscon Nozzles

The energy dissipation rate in the Viscon nozzles can be estimated by calculating the pressure drop in the contraction zone of the nozzles. The energy dissipated in the nozzles is the product of the pressure drop and the volumetric flow rate. By calculating the ratio of this energy dissipation and the volume of the contraction zone, an estimation for the energy dissipation rate in the nozzle can be obtained.

Calculation of the Pressure Drop in the Viscon Nozzles

The total number of Viscon nozzles is $N_{VN} = 12$. The following calculation uses the values according to the first centrifuge run from the data set provided by Sandoz (refer to Subsection D.1, [Piskernik, 2008]). The feed mass flow rate was $\dot{m}_f = 1,931.6 [kg h^{-1}]$ and the mass flow rate of the light phase $\dot{m}_l = 1,260.2 [kg h^{-1}]$. The mass flow rate of the dense phase can be calculated from the difference in these two mass flow rates and is equal to:

$$\dot{m}_d = \dot{m}_f - \dot{m}_l = 671.4 [kg h^{-1}] \quad (5.5)$$

The fluid density is assumed to be equal to the density of water $\rho = 1,000 [kg m^{-3}]$. Furthermore, it is assumed that the amount of dense phase material is only exiting

through the Viscon nozzles. Thus, the mass flow rate through the radial exit nozzles is neglected. The volumetric flow rate of the dense phase through a single nozzle is given by:

$$\dot{V}_{VN} = \frac{\dot{m}_d}{\rho \cdot N_{VN}} = 1.55 \cdot 10^{-5} \text{ [m}^3 \text{ s}^{-1}] \quad (5.6)$$

The diameter of the wider zone is $d_1 = 28 \text{ [mm]}$ and has a cross sectional area of $A_1 = 6.16 \cdot 10^{-4} \text{ [m}^2]$. The diameter of the nozzle (i.e., the contraction) is $d_2 = 0.6 \text{ [mm]}$ and a cross sectional area of $A_2 = 2.8 \cdot 10^{-7} \text{ [m}^2]$. The average fluid velocities in the wider zone u_1 and in the contraction zone u_2 can be calculated using Equation (5.7).

$$u_1 = \frac{\dot{V}_{VN}}{A_1} = 0.025 \text{ [m s}^{-1}] \quad u_2 = \frac{\dot{V}_{VN}}{A_2} = 55.4 \text{ [m s}^{-1}] \quad (5.7)$$

The flow conditions in the nozzles are determined by the Reynolds number. The fluid viscosity has been measured and is equal to $\eta = 6.33 \text{ [mPas]}$. The kinematic viscosity can be calculated from $\nu = \eta/\rho$ and is equal to $\nu = 6.33 \cdot 10^{-6} \text{ [m}^2 \text{ s}^{-1}]$. The Reynolds number is given by:

$$Re = \frac{d \cdot u}{\nu} = \frac{d_2 \cdot u_2}{\nu} = \frac{0.6 \cdot 10^{-3} \cdot 55.4}{6.33 \cdot 10^{-6}} = 5,251 \text{ [-]} \quad (5.8)$$

The Reynolds number is above the critical Reynolds number for laminar pipe flow of $Re_{crit} = 2,300 \text{ [-]}$, and therefore, the flow condition is considered to be turbulent. The Bernoulli equation for incompressible flow is given in Equation (5.9). The loss coefficient K for the entrance loss for turbulent flow is calculated by Equation (5.10) [Perry, 1997]. The loss coefficient gives $K = 0.50 \text{ [-]}$.

$$p_1 - p_2 = \Delta p = \alpha_2 \frac{\rho u_2^2}{2} - \alpha_1 \frac{\rho u_1^2}{2} + \rho g (z_2 - z_1) + K \frac{\rho u_2^2}{2} \quad (5.9)$$

$$K = 0.5 \left(1 - \frac{A_2}{A_1} \right) \quad (5.10)$$

The difference in height $z_2 - z_1$ is neglected and the flow is assumed to be uniform ($\alpha_1 = \alpha_2 = 1$). This results in a pressure drop related to the contraction zone:

$$\Delta p = 2.27 \cdot 10^6 \text{ [Pa]} \quad (5.11)$$

Calculation of the Energy Dissipation Rate in the Viscon Nozzles

The term $\Delta p \dot{V}_{VN}$ expresses an energy loss per unit time in the Viscon nozzle. By taking the ratio of this energy loss and the total mass in which the energy is dissipated, one obtains an estimate for the energy dissipation rate in the Viscon nozzles ϵ_{VN} (see Equation (5.12)). The corresponding volume is assumed to be the volume of the contraction zone of the nozzle V_c . With a diameter of $d_2 = 0.6 \text{ [mm]}$ and a length

\dot{m}_d [kg h ⁻¹]	ϵ_{VN} [W kg ⁻¹]
1,000	$2.74 \cdot 10^8$
900	$2.00 \cdot 10^8$
800	$1.40 \cdot 10^8$
700	$9.41 \cdot 10^7$
600	$5.93 \cdot 10^7$
500	$3.43 \cdot 10^7$
400	$1.76 \cdot 10^7$
300	$7.41 \cdot 10^6$
200	$2.19 \cdot 10^6$
100	$2.74 \cdot 10^5$
50	$3.43 \cdot 10^4$

Table 5.6: Results of the estimation of the energy dissipation rate in the Viscon nozzles

of the contraction of $h_c = 1.5$ [mm], the volume of the contraction zone becomes $V_c = 0.424$ [mm³]. Table 5.6 shows the results of the estimation of the EDR for different total mass flow rates of the dense phase \dot{m}_d through the Viscon nozzles.

$$\epsilon_{VN} = \frac{\Delta p \dot{V}_{VN}}{\rho V_c} = 8.3 \cdot 10^7 \text{ [W kg}^{-1}\text{]} \quad (5.12)$$

5.4.2 Simulation of the Viscon Nozzles

The flow in the Viscon nozzles has been simulated using the Launder-Sharma low-Reynolds-number model to resolve the flow of the contraction zone. For this purpose, the mesh has been generated with an extremely high resolution. The region in the inlet region of the Viscon nozzles shows rotational symmetry at the contraction zone. Only the piping at the bottom enters the domain off-centered. To reduce the size of the mesh, a slice of the symmetric region has been picked for the simulation. Since the diameter of the piping from the separator bowl is large compared to the contraction diameter, the flow velocity is comparably low in the region in front of the Viscon nozzles. Hence, the effect of the piping on the flow field in front and directly in the nozzle can be neglected. Consequently, the inlet condition has been set as shown in see Figure 5.19).

The mesh has been designed for the case with the highest inlet velocity, which typically requires the highest resolution. The same mesh has been used for the other cases with a lower inlet velocity (see Figure 5.20). The number of grid cells for the slice was 283k with an average $y+$ value of approximately 0.1. The region near the contraction zone has been refined, especially at the entrance of the contraction zone. All simula-

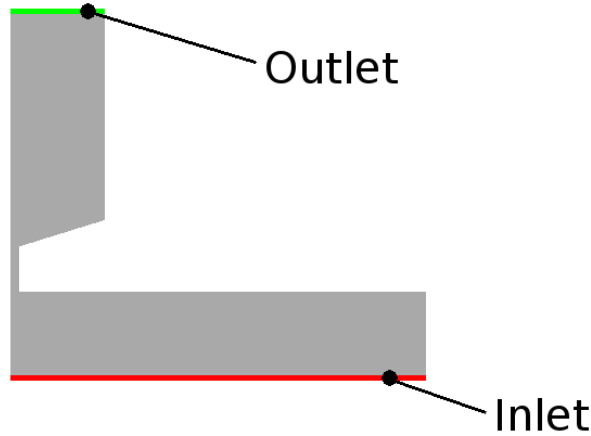


Figure 5.19: Inlet and outlet boundary used for the Viscon nozzle simulation

tions have been started with a high Reynolds number model for turbulence (standard k-epsilon model). Then, the solution obtained with the high-Reynolds-number model has been used as the initial condition for the Launder-Sharma low-Reynolds-number turbulence model.

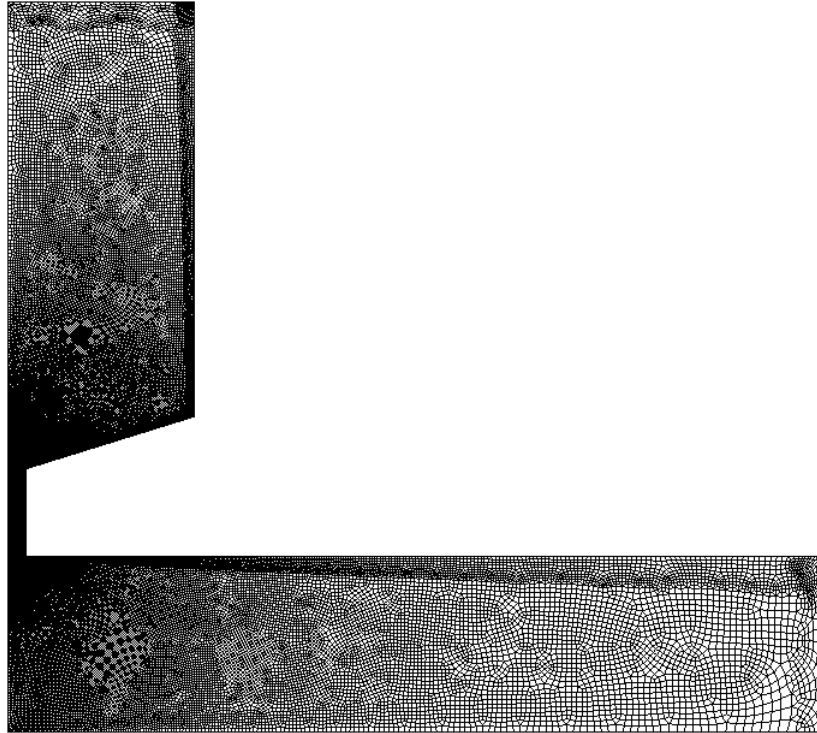
Boundary Conditions

The inlet velocity has been calculated according to the calculation of w_1 (shown in Subsection 5.4.1) for different dense phase flow rates ($\dot{m}_d = 160; 330; 520; 720 [kg h^{-1}]$). The velocity on wall patches has been set to 0 [$m s^{-1}$] (no-slip condition). The pressure has been set to zero gradient at the inlet and to be 0 [$m^2 s^{-2}$] at the outlet. On walls, k and epsilon have been set to be $10^{-20} [m^2 s^{-2}]$ to prevent problems due to divisions by 0, and zero gradient on the inlet and outlet patches.

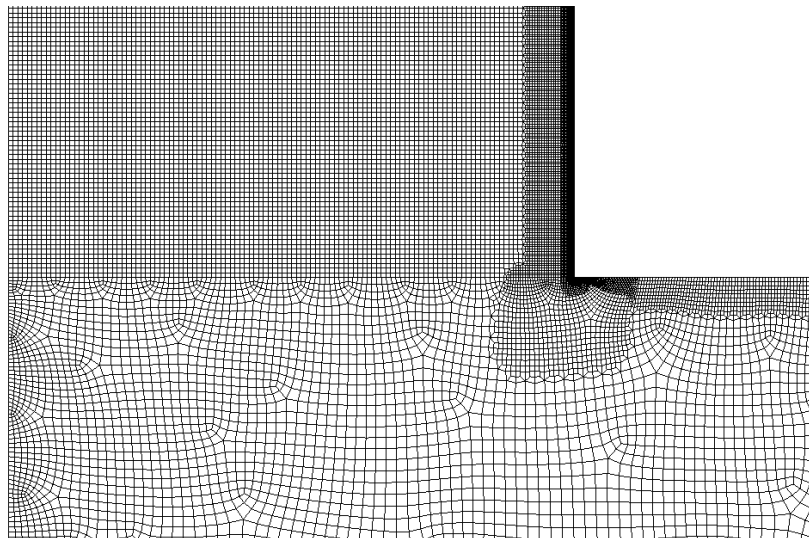
5.4.3 Results

Both, calculations as well as the simulations of the Viscon nozzles showed that the energy dissipation rate in these nozzles is extremely high. The plots from the simulations with different flow rates of the dense phase through the nozzles are shown in Figure 5.21 to Figure 5.24. The maximum occurring energy dissipation rate in the simulations is located in a small region close to the edge at the entrance of the contraction zone. A list of the maximum EDR values is given in Table 5.7. A comparison of the pressure drop from the calculation and from the simulations is shown in Figure 5.25. In Figure 5.26 the estimated EDR is illustrated and compared with the results from the simulations. For this purpose, we show the minimal and maximal values for the simulated EDR near the entrance of the contraction zone.

The maximum EDR-level observed in the simulations is very high. This is due to the non-uniform velocity distribution in the nozzle, which causes extremely high velocity



(a) Unzoomed



(b) Zoom of contraction

Figure 5.20: The computational mesh of the Viscon nozzles

gradients near the wall.

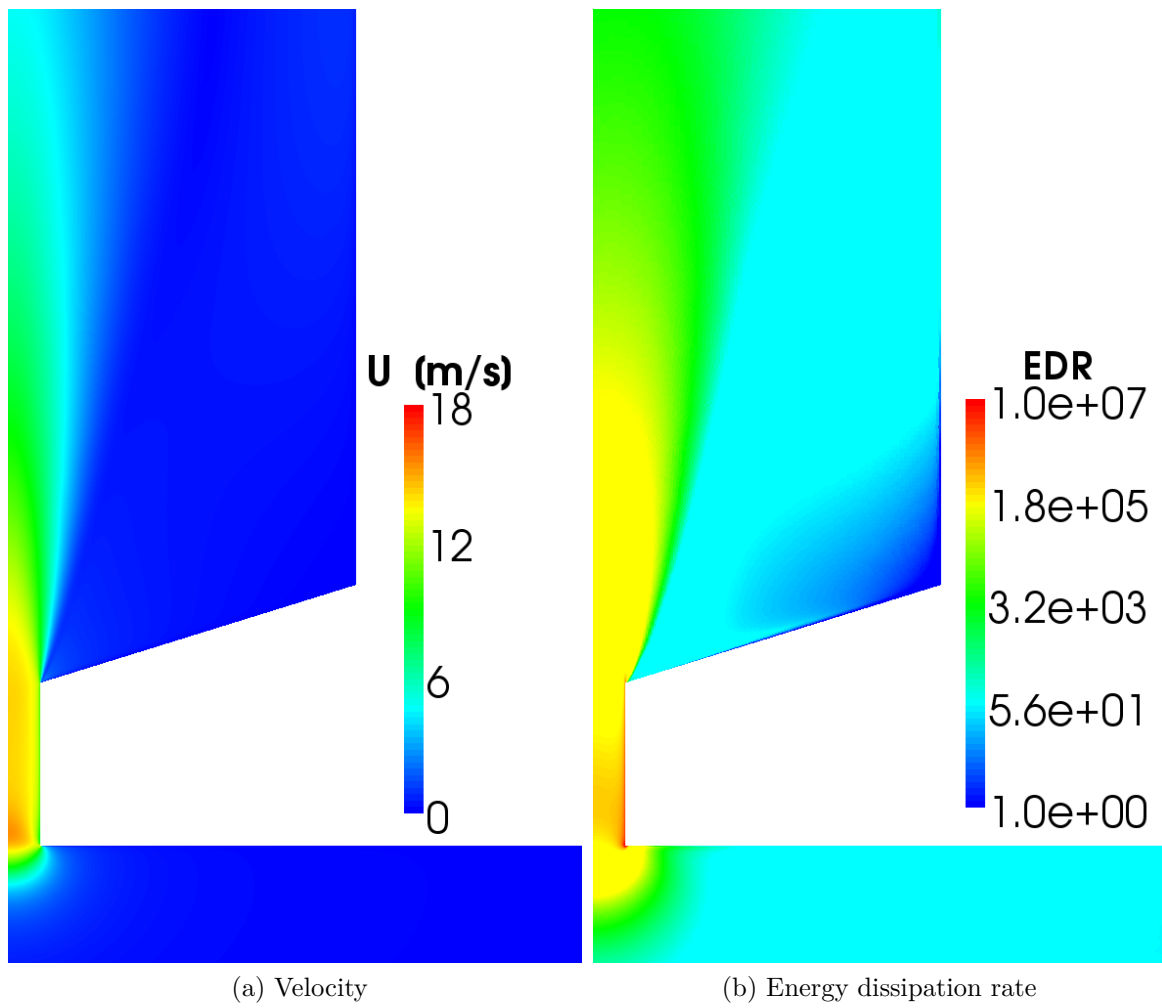


Figure 5.21: Plot of the simulation results for the Viscon nozzle simulation ($\dot{m}_d = 160 [kg h^{-1}]$)

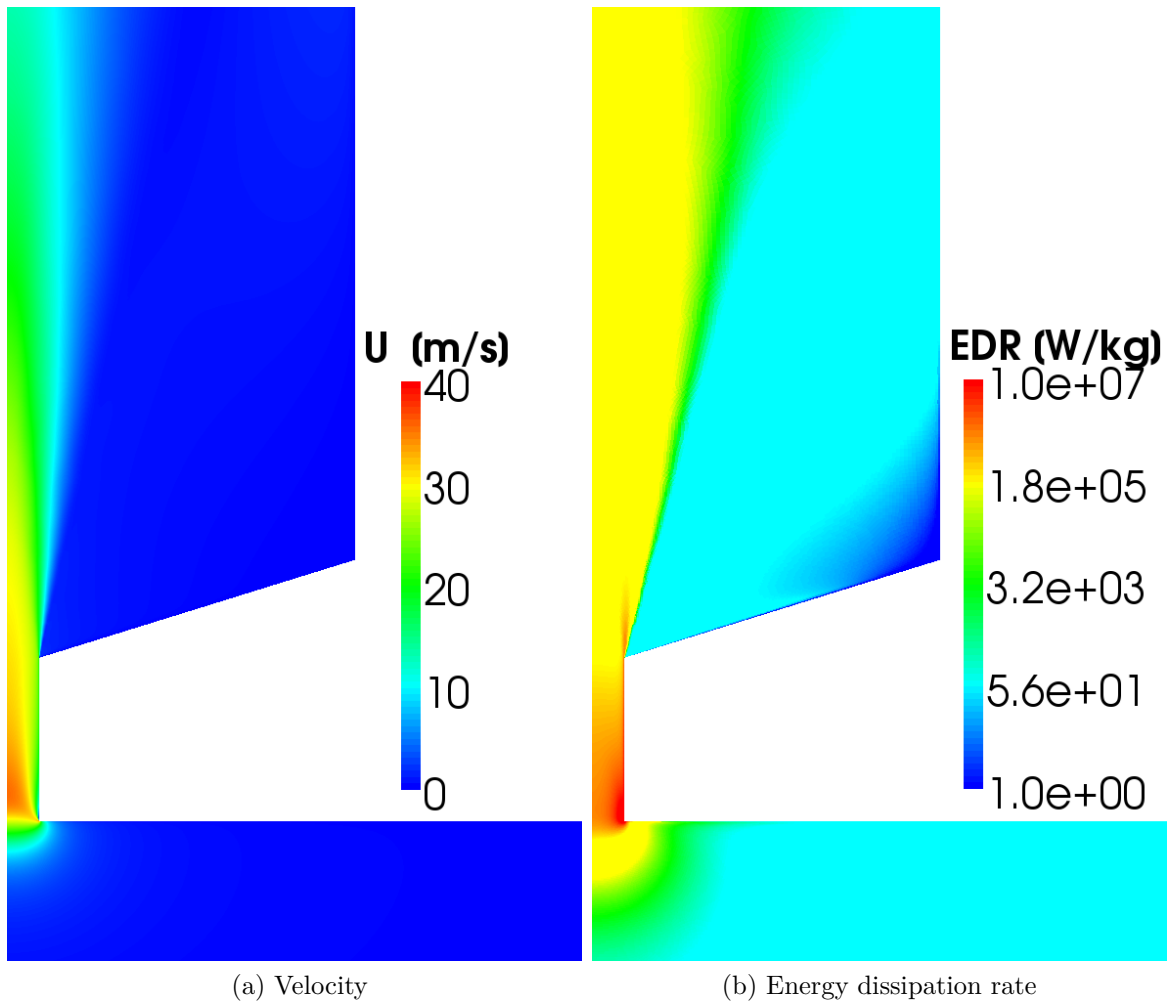


Figure 5.22: Plot of the simulation results for the Viscon nozzle simulation ($\dot{m}_d = 330 [kg h^{-1}]$)

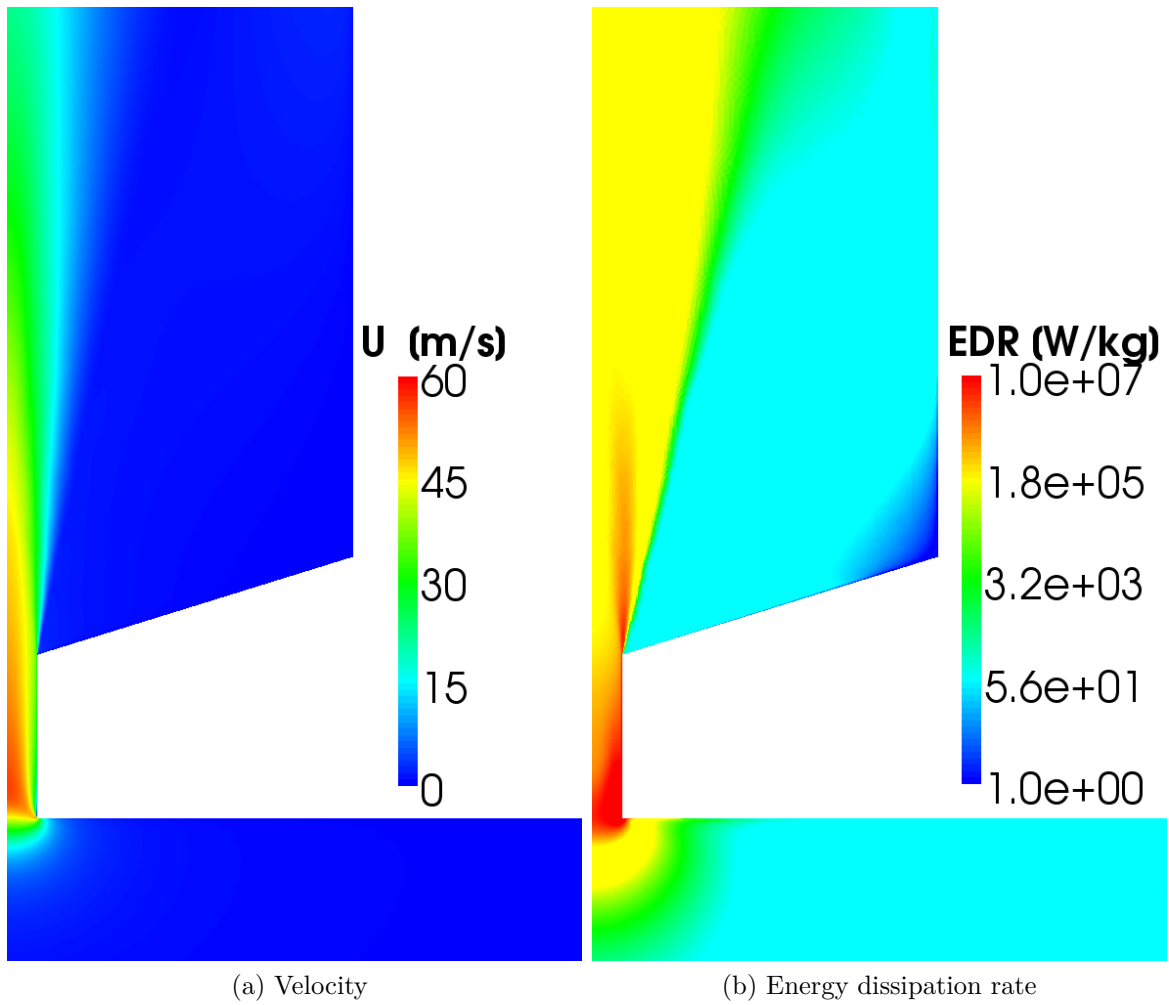
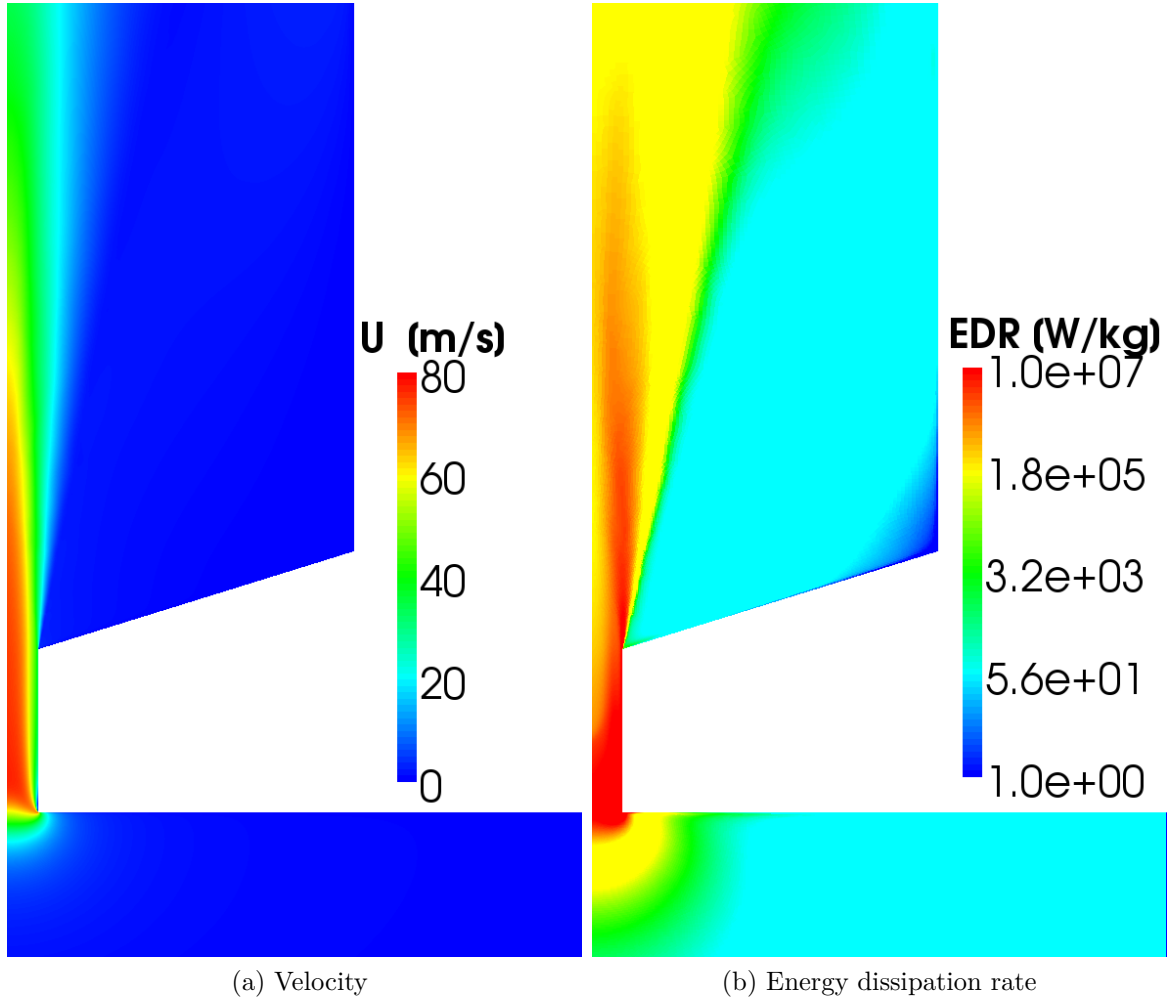


Figure 5.23: Plot of the simulation results for the Viscon nozzle simulation ($\dot{m}_d = 520 [kg h^{-1}]$)

\dot{m}_d [$kg\ h^{-1}$]	max. EDR [$W\ kg^{-1}$]
160	7.4×10^7
330	1.8×10^8
520	8.1×10^8
700	2.6×10^9

Table 5.7: Maximum energy dissipation rates in the Viscon nozzle simulations

Figure 5.24: Plot of the simulation results for the Viscon nozzle simulation ($\dot{m}_d = 700$ [$kg\ h^{-1}$])

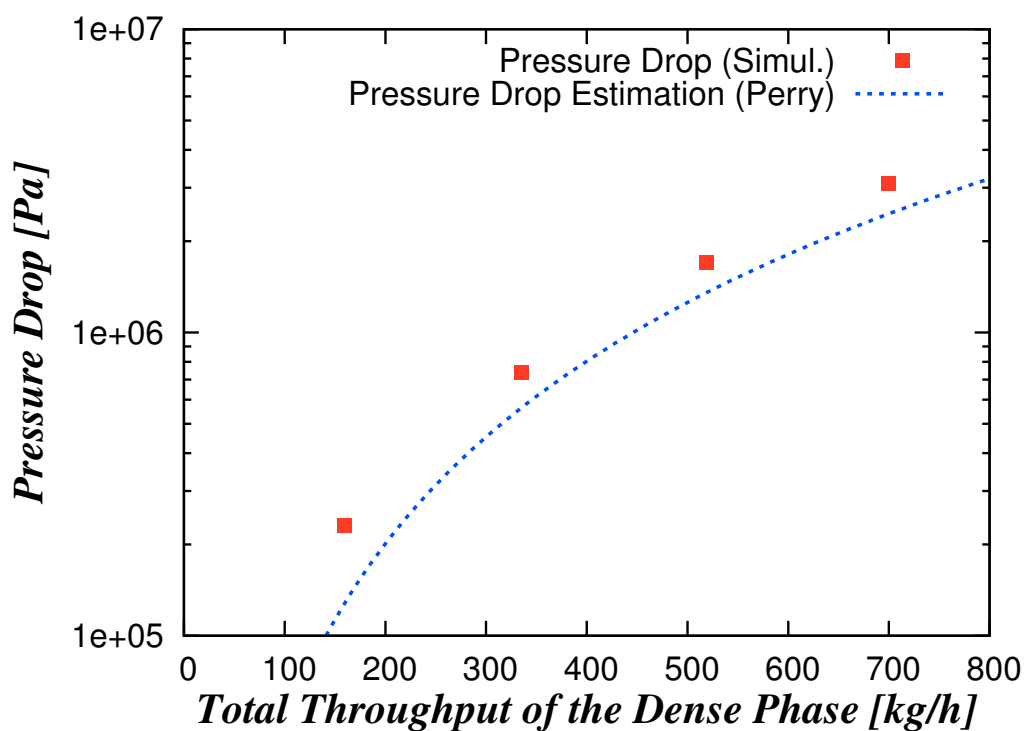


Figure 5.25: Results for the pressure drop of the Viscon nozzles

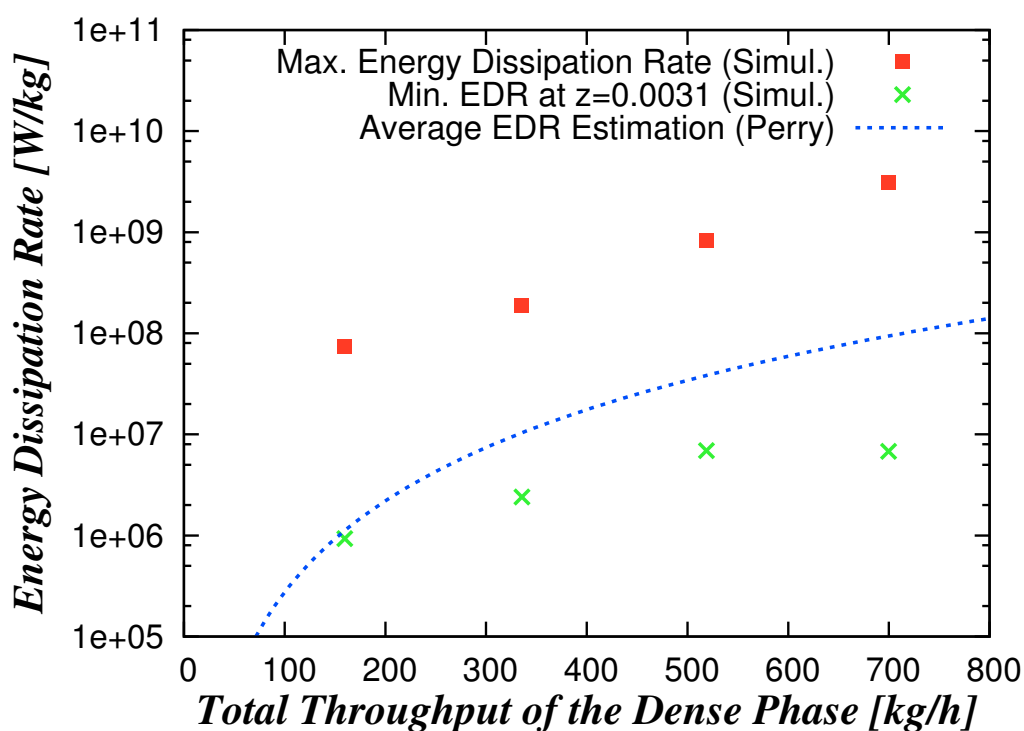


Figure 5.26: Results for the energy dissipation rate of the Viscon nozzles

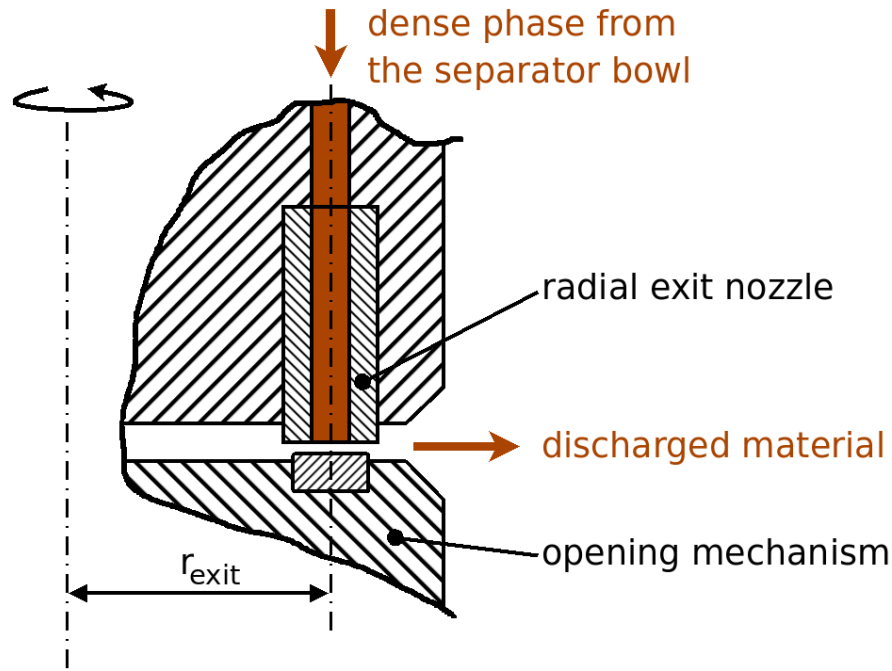


Figure 5.27: Schematic drawing of a cut through the radial exit nozzles

5.5 Radial Exit Nozzles

During the release of the dense phase through the radial exit nozzles of the disc stack separator bowl, a liquid jet is formed. This liquid jet then impacts on the surrounding separator housing which may cause significant cell damage. Furthermore, the liquid jet formation as well as the impact on the separator housing is influenced by the air in the housing. Due to the high rotational speed of the separator, the air flow in the housing will be turbulent. Thus, the interaction of the circulating air and the jet will be complex and cannot be easily quantified. There is very few literature dealing with this kind of gas-liquid interaction as well as its impact on cell breakage or the energy dissipation rate induced in the jet.

It has been shown that the exit velocity and the distance to impact are influencing cell destruction [Chan et al., 2006]. The highest exit speed in the experiments of this study was $85 [m s^{-1}]$ which lead to 6-7% of cell breakage of *DH5 α -E.coli* cells at $90 [mm]$ impact distance.

In case of the disc stack separator of Sandoz, opening of the nozzles happens in axial direction, i.e., only a minimal radial velocity of the discharged material is expected (see Figure 5.27). Therefore, the velocity in radial direction is neglected in the calculation and the velocity of the discharged material is assumed to be in tangential direction only. The exit velocity can be estimated by calculating the circumferential velocity at the distance of the exit nozzles from the rotation axis (see Figure 5.29).

With a given distance of the radial exit nozzles from the center of rotation of $r_{exit} = 242 [mm]$ and a rotational speed of $8,000 [rpm]$, the circumferential velocity

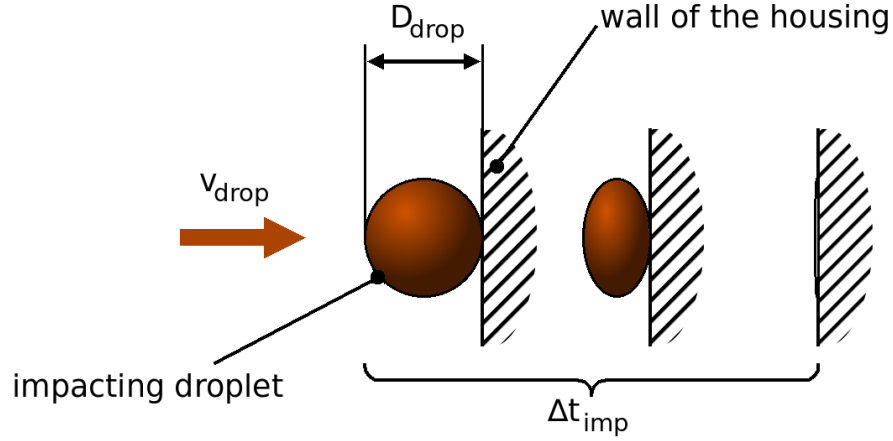


Figure 5.28: Schematic drawing for the estimation of the impact time of a droplet on a wall.

becomes $v_{exit} = 203 [m s^{-1}]$. There is a substantial difference of the resulting exit speed compared to the $85 [m s^{-1}]$ from the study of [Chan et al., 2006]. Thus, the high exit velocity in Sandoz' separators has a much higher potential for cell destruction, since the kinetic energy is proportional to the velocity squared (see Equation (5.14)). Literature data describing the effect of such high impact velocities on cell stress or the energy dissipation during the impact of droplets could not be found.

The energy dissipation rate can be seen as a specific energy loss (i.e. energy per unit volume or mass) per unit time (see Equation (5.13)). To estimate the energy dissipation rate during the impact of the droplets, the following calculations have been made.

5.5.1 EDR Estimation Neglecting Air Resistance

In this scenario the drag force exhibited by the surrounding atmosphere on the discharged material is neglected. This means that the velocity of a droplet is constant between discharge and impact (i.e., $v_{drop} = v_{exit}$). Furthermore, the amount of energy dissipated by a droplet is approximated by the kinetic energy of the droplet at the nozzle exit (Equation (5.14)). The time it takes to dissipate the kinetic energy during the impact, Δt_{imp} , has to be estimated. In this approach, this time is taken to be equal to the time it takes the droplet to move a distance of one droplet diameter D_{drop} (see Figure 5.28):

$$\epsilon = \frac{E}{\Delta t_{imp} \cdot m_{drop}} \quad (5.13)$$

$$E = E_{kin} = \frac{m_{drop} \cdot v_{drop}^2}{2} \quad (5.14)$$

$$\Delta t_{imp} = \frac{D_{drop}}{v_{drop}} \quad (5.15)$$

Inserting Equation (5.14), Equation (5.15) and m_{drop} in Equation (5.13) gives an estimate for the energy dissipation rate that occurs during impact ϵ_{imp} (Equation (5.16)).

$$\epsilon_{imp} = \frac{v_{drop}^3}{2 \cdot D_{drop}} \quad (5.16)$$

Therefore the energy dissipation rate ϵ_{imp} can be expressed by the two variables v_{drop} and D_{drop} in this approach.

The results are shown in Table 5.8. The energy dissipation rate for droplet impact, in the operating range of the disc stack separator of 6,800–8,000 [rpm] (i.e. $v_{exit} = 172 - 203$ [$m s^{-1}$]), is of the order of 10^9 [$W kg^{-1}$] and above for smaller droplet diameters. This result indicates a high potential for cell destruction, which is substantially higher than inside of the entrance region of the disc stack separator (EDR of the order of 10^5 [$W kg^{-1}$], compare Subsection 5.3.3).

It can be seen that this approach leads to smaller energy dissipation rates for larger particles. Since air resistance has a stronger effect on smaller sized particles, the results are possibly reversed, when drag is considered in the calculation. Therefore, estimations for the EDR during droplet impact have been also performed taking the drag force exhibited by the surrounding air into account.

v_{exit}	[$m s^{-1}$]	50	100	150	200	250
<hr/>						
$D_{drop} = 0.1$	[mm]					
v_{imp}	[$m s^{-1}$]	50	100	150	200	250
ϵ_{imp}	[$W kg^{-1}$]	$6.3 \cdot 10^8$	$5.0 \cdot 10^9$	$1.7 \cdot 10^{10}$	$4.0 \cdot 10^{10}$	$7.8 \cdot 10^{10}$
<hr/>						
$D_{drop} = 0.5$	[mm]					
v_{imp}	[$m s^{-1}$]	50	100	150	200	250
ϵ_{imp}	[$W kg^{-1}$]	$1.3 \cdot 10^8$	$1.0 \cdot 10^9$	$3.4 \cdot 10^9$	$8.0 \cdot 10^9$	$1.6 \cdot 10^{10}$
<hr/>						
$D_{drop} = 1.0$	[mm]					
v_{imp}	[$m s^{-1}$]	50	100	150	200	250
ϵ_{imp}	[$W kg^{-1}$]	$6.3 \cdot 10^7$	$5.0 \cdot 10^8$	$1.7 \cdot 10^9$	$4.0 \cdot 10^9$	$7.8 \cdot 10^9$
<hr/>						
$D_{drop} = 5.0$	[mm]					
v_{imp}	[$m s^{-1}$]	50	100	150	200	250
ϵ_{imp}	[$W kg^{-1}$]	$1.3 \cdot 10^7$	$1 \cdot 10^8$	$3.4 \cdot 10^8$	$8.0 \cdot 10^8$	$1.6 \cdot 10^9$

Table 5.8: Energy dissipation rate of a spherical droplet dependent on the droplet diameter and its velocity

5.5.2 EDR Estimation Including Air Resistance

In the following approach, air resistance has been taken into account. The flow around the separator bowl is complex and can not be easily described. As a simplification, the surrounding atmosphere is considered to be stationary. A schematic sketch of this situation is illustrated in Figure 5.29. The effect of gravity has been neglected, which leads to a one dimensional problem.

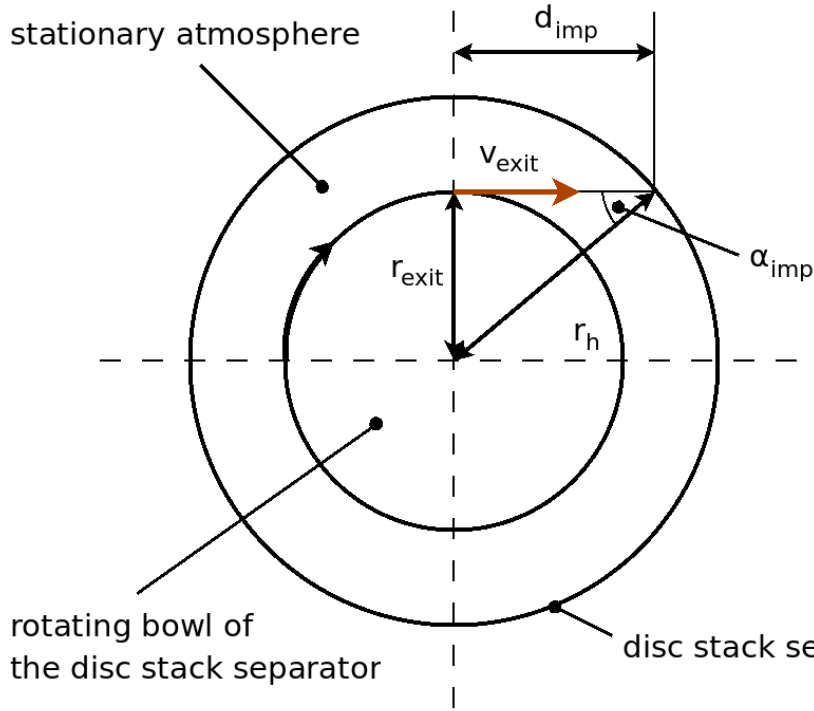


Figure 5.29: Schematic drawing of the exit velocity of discharged material from the separator

Newton's second law of motion, including the effect of drag, is given in Equation (5.17).

$$m_{drop} \cdot \ddot{x}_{drop} = -\frac{\rho_h}{2} \cdot c_D \cdot A_D \cdot \dot{x}_{drop}^2 \quad (5.17)$$

Here \ddot{x}_{drop} and \dot{x}_{drop} denote the acceleration a_{drop} and the velocity v_{drop} of the droplets, respectively. The drag coefficient c_D has been calculated for rigid spherical particles using Equation (5.18) after Clift and Gauvin for $Re < 3 \cdot 10^5$ [Clift et al., 1978].

$$c_D = \frac{24}{Re} \cdot (1 + 0.15 \cdot Re^{0.687}) + \frac{0.42}{1 + 4.25 \cdot 10^4 \cdot Re^{-1.16}} \quad Re < 3 \cdot 10^5 \quad (5.18)$$

The drag coefficient depends on the Reynolds number and therefore on the velocity of the droplets, which leads to a non-linear differential equation of second order.

In this estimation, the solution of this non-linear differential equation has been calculated numerically using the software *Octave* (see Section C of the appendix). In Figure

C.1 the validation of the numerical algorithm is shown, where the solution has been calculated numerically and analytically for a constant drag coefficient c_D , calculated at the initial velocity v_{exit} (see Equation (5.19) and Equation (5.20)).

$$v_{drop}(t) = \frac{2 \cdot m_{drop} \cdot v_{exit}}{2 \cdot m_{drop} + \rho_h \cdot A_D \cdot c_D \cdot v_{exit} \cdot t} \quad (5.19)$$

$$t(d) = \frac{2 \cdot m_{drop}}{\rho_h \cdot A_D \cdot c_D \cdot v_{exit}} \left(\exp\left(\frac{\rho_h \cdot A_D \cdot c_D}{2 \cdot m_{drop}} \cdot d\right) - 1 \right) \quad (5.20)$$

To solve Newton's second law of motion with variable c_D , the differential equation has been approximated with a difference equation:

$$a_{drop} = \frac{\Delta v_{drop}}{\Delta t_{drop}} \quad (5.21)$$

$$m_{drop} \cdot \frac{\Delta v_{drop}}{\Delta t} = -\frac{\rho_h}{2} \cdot c_D(v_{drop,old}) \cdot A_D \cdot v_{drop,old}^2 \quad (5.22)$$

The velocity difference Δv_{drop} has been calculated by starting from the exit velocity $v_{drop,old} = v_{exit}$, the drag coefficient with the initial velocity $c_D(v_{exit})$ and the fixed time-step $\Delta t = 10^{-8}$ [s]. From there, the following velocity $v_{drop,new}$ for the next time-step can be calculated:

$$v_{drop,new} = v_{drop,old} + \Delta v_{drop} \quad (5.23)$$

The new position of the droplet $d_{drop,new}$ can be calculated by Equation (5.24) with an initial position from the exit of 0 [m].

$$d_{drop,new} = d_{drop,old} + v_{drop,old} \cdot \Delta t \quad (5.24)$$

The impact distance d_{imp} can be calculated from the distance of the radial exit nozzles $r_{exit} = 242$ [mm] and the distance from the disc stack separator housing $r_h = 440$ [mm] from the center of rotation (see Equation (5.25)). Transforming Equation (5.25) leads to $d_{imp} = 367$ [mm].

$$d_{imp}^2 = r_h^2 - r_{exit}^2 \quad (5.25)$$

The stationary atmosphere inside of the housing of the disc stack separator has been considered as air at a temperature of 10 [°C] with a density of $\rho_h = 1.23$ [kg m⁻³] and a kinematic viscosity of $\nu_h = 1.44 \cdot 10^{-5}$ [m² s⁻¹] [VDI, 2006]. The Reynolds number for the droplets has been calculated according to Equation (5.26).

$$Re = \frac{D_{drop} \cdot v_{drop}}{\nu_h} \quad (5.26)$$

The highest occurring Reynolds number in the calculation is $Re = 8.68 \cdot 10^4 [-]$ for a droplet diameter of $D_{drop} = 5 [mm]$ and an exit velocity of $v_{exit} = 250 [m s^{-1}]$. Therefore, the equation for the drag coefficient is valid for the Reynolds number range in this calculation (see Equation (5.18)). For low Reynolds numbers $Re < 0.1$, Stokes law has been applied in the calculation, which leads to Equation (5.29) [Perry, 1997]. The equation with air resistance described by Stokes law has been integrated in the numerical calculation, but it can be solved analytically as well (see Equation (5.27) and Equation (5.28)).

$$v(t) = v_{exit} \cdot \exp\left(-\frac{3 \cdot \pi \cdot \mu_h \cdot D_{drop}}{m_{drop}} \cdot t\right) \quad (5.27)$$

$$t(d) = -\frac{m_{drop}}{3 \cdot \pi \cdot \mu_h \cdot D_{drop}} \cdot \ln\left(1 - \frac{3 \cdot \pi \cdot \mu_h \cdot D_{drop}}{v_{exit} \cdot m_{drop}} \cdot d\right) \quad (5.28)$$

The validation for the numerical solution of Stokes law is shown in Figure C.2. Here, μ_h is the dynamic viscosity of air ($\mu_h = \nu_h \cdot \rho_h$).

$$m_{drop} \cdot \frac{\Delta v_{drop}}{\Delta t_{drop}} = -3 \cdot \pi \cdot \mu_h \cdot D_{drop} \cdot v_{drop} \quad (5.29)$$

The results are shown in Table 5.9. The table indicates that considering air resistance leads to inverted results in EDR. Smaller droplets are decelerated stronger by air resistance, and a droplet with $D_{drop} = 0.1$ at an initial speed of $v_{exit} = 50 [m s^{-1}]$ loses speed drastically and would not hit the wall of the housing. Larger droplets are less affected by air resistance, showing a result, which is closer to the result from the calculation without consideration of air resistance (see Table 5.8).

The calculations performed in this work are a first attempt to quantify the conditions during the impact of droplets. Due to the complicated physical effects involved in the discharge process (e.g. jet breakup, turbulent air flow in the separator, etc.), several challenges are remaining for future research.

5.5 Radial Exit Nozzles

v_{exit}	$[m s^{-1}]$	50	100	150	200	250
$D_{drop} = 0.1$ $[mm]$						
v_{imp}	$[m s^{-1}]$	0.0	5.6	16.8	29.9	44.3
ϵ_{imp}	$[W kg^{-1}]$	0.0	$9.0 \cdot 10^5$	$2.3 \cdot 10^7$	$1.3 \cdot 10^8$	$4.3 \cdot 10^8$
$D_{drop} = 0.5$ $[mm]$						
v_{imp}	$[m s^{-1}]$	17.7	44.6	72.7	100.7	128.3
ϵ_{imp}	$[W kg^{-1}]$	$1.4 \cdot 10^7$	$2.2 \cdot 10^8$	$9.6 \cdot 10^8$	$2.5 \cdot 10^9$	$5.3 \cdot 10^9$
$D_{drop} = 1.0$ $[mm]$						
v_{imp}	$[m s^{-1}]$	43.9	87.5	130.3	172.8	215.0
ϵ_{imp}	$[W kg^{-1}]$	$4.2 \cdot 10^7$	$3.3 \cdot 10^8$	$1.1 \cdot 10^9$	$2.5 \cdot 10^9$	$4.9 \cdot 10^9$
$D_{drop} = 5.0$ $[mm]$						
v_{imp}	$[m s^{-1}]$	48.5	96.8	145.1	193.5	241.8
ϵ_{imp}	$[W kg^{-1}]$	$1.1 \cdot 10^7$	$9.1 \cdot 10^7$	$3.1 \cdot 10^8$	$7.2 \cdot 10^8$	$1.4 \cdot 10^9$

Table 5.9: Energy dissipation rate of the impact of a spherical drop on the separator housing considering air resistance

6 Design of the Ultra Scale-Down Device

6.1 Designing the Shear Device

The design of the shear device has been made according to the proposed scale-down approach (see Section 3). It consists of a rotating disc inside of a cylindrical vessel. A schematic view of the geometry parameters of the shear device is shown in Figure 6.1. The two geometrical parameters of the device, i.e., the radius r_{SD} and height h_{SD} of the cylindrical vessel, have been varied to find an adequate configuration. The rotating disc has been positioned in the center of the vessel, i.e. $h_d = h_{SD}/2$. The thickness of the disc has been fixed with $s_d = 1$ [mm], and the distance between the radius of the disc r_d and the radius of the vessel r_{SD} has been fixed with 5 [mm].

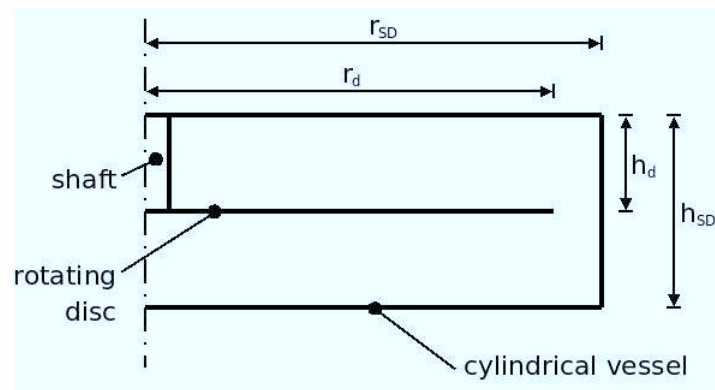


Figure 6.1: Geometry parameters of the shear device

The decision on the final geometrical configuration has been influenced by two criteria. One criterion was the size of the shearing chamber. A complete run through the USD process has to be finished within the given time span of 2 hours in total, including shearing and centrifuging [Piskernik, 2008]. The size of the shearing chamber and a certain residence time in the shear device lead to the required time for shearing. If configurations show too long processing times, leaving not enough time for centrifuging and handling, they can not be considered. Therefore, the time needed for shearing in the shear device is a key factor for the geometry of the device, and is discussed in Section 6.1.1. Additionally, the available motors on the market have an influence on the size of the shear device as well, since suitable motors have only a limited range in the power output.

Another criterion is how the bio-material is exposed to the energy dissipated in the shearing chamber. This exposure determines the cells' EDR profile, i.e., the distribution of EDR experienced by the cells. Different configurations have been simulated and analysed. The results of the EDR profile analysis are given in Subsection 6.1.2.

6.1.1 Geometrical Configurations of the Shear Device

The amount of the sample material to be processed by the ultra scale-down device has to be in the range of $V_{Sample} = 1 - 6 [L]$. The maximum value for the volume of the sample material $V_{Sample} = 6 [L]$ has been chosen as the design parameter to calculate the processing time. The average residence time in the shear device has been fixed with $t_{res} = 20 [s]$ based on literature data. For a continuous process, the volumetric flow rate \dot{V}_{USD} through the shear device V_{SD} can be calculated according to the average residence time t_{res} (Equation (6.1)). The total time for the shearing process t_{SD} is calculated according to Equation (6.2).

$$\dot{V}_{USD} = \frac{V_{SD}}{t_{res}} \quad (6.1)$$

$$t_{SD} = \frac{V_{Sample}}{\dot{V}_{SD}} \quad (6.2)$$

The results for the studied geometries are listed in Table 6.1. The results show that smaller geometries lead to longer processing times, which is due to the fixed residence time in the shearing chamber. Therefore, the limitation in the process time defines a lower limit for geometrical parameters. The studied geometries starting from a size of $r_{SD} = 30 [mm]$, $h_{SD} = 20 [mm]$ and up are considered to leave sufficient time required for further steps in the USD process. Due to the capacity of the available laboratory centrifuge (Beckman Coulter Avanti J-25 with a JLA-9.1000 rotor), the maximum amount of bio-material for one run of the centrifuge is limited to 4 [L]. Thus, a total amount of feed material larger than 4 [L] requires two runs of the centrifuge.

r_{SD} [mm]	h_{SD} [mm]	V_{SD} [ml]	\dot{V}_{USD} [ml min ⁻¹]	t_{SD} [min]
20	15	19	57	106.1
30	20	57	170	35.4
40	30	151	452	13.3
40	40	201	603	9.9
50	30	236	707	8.5
50	40	314	942	6.4
50	50	393	1,178	5.1

Table 6.1: Geometrical configurations of the shear device

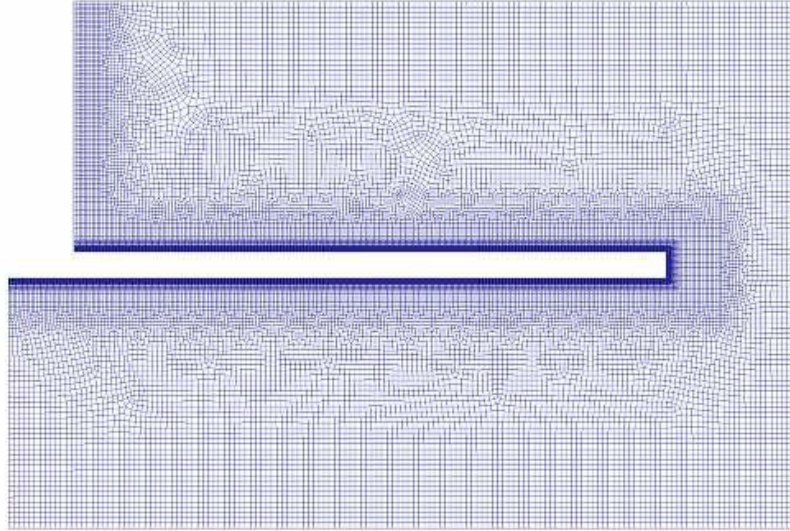


Figure 6.2: Computational mesh of the shear device

6.1.2 EDR Profiles

Simulation Setup

The EDR profiles have been determined by CFD simulations for the geometrical configurations shown in Table 6.1. The generated mesh of the shear device has been reduced to a slice of 5° , due to rotational symmetry, and prepared for the use with a high-Reynolds-number model to save computation time.

To generate the computational meshes for the different configurations, a *m4* script file has been written, which includes explicit parameter settings for the geometry and mesh specifications (see Subsection B.2.1). Adjusting parameters of a such a *m4* script file simplifies the generation of multiple meshes with the same geometrical structure. The mesh has been built for the use with the *OpenFOAM* solver *MRFSimpleFoam*, which requires the definition of a rotating zone and a stationary zone. The different zones take the rotating zone around the rotating disc and the stationary zone with the surrounding walls into account. For a given set of parameters, the *m4* script file exports a journal file, which is formatted for the use with the meshing software *Cubit*. Then, the mesh can be generated with *Cubit* by running the journal file. From there, the exported mesh is prepared for the use in *OpenFOAM* by the *makeMesh* shell script including the final command sequences to generate the slice-shaped geometry (see Subsection B.2.2). A screenshot of the computational mesh is given in Figure 6.2, in which the refined mesh close to the rotating disc is illustrated.

The simulations have been conducted using the standard k-epsilon turbulence model, which is a high-Reynolds-number model. The boundary conditions include a specific rotational speed for the rotating disc and the no-slip condition at the walls (i.e., the velocity relative to the wall equals zero). To allow a comparison of the EDR profiles

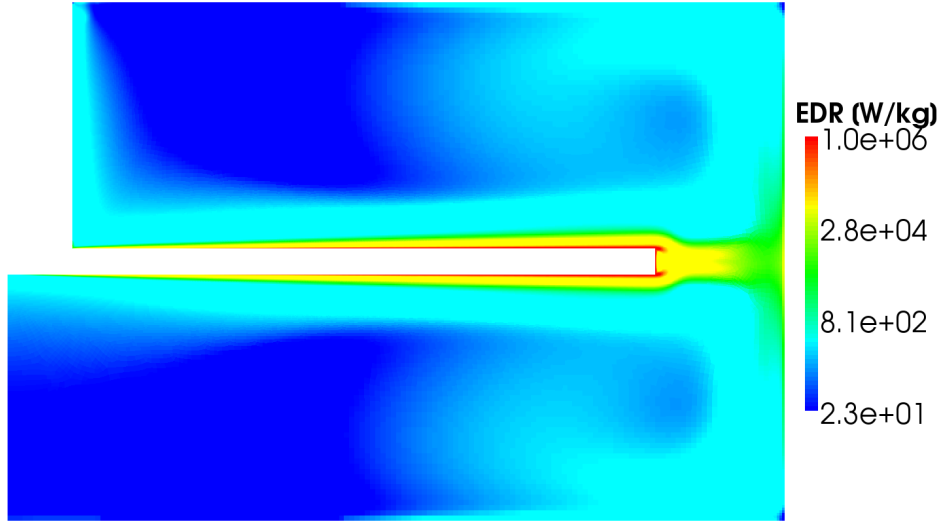


Figure 6.3: Plot of the energy dissipation rate

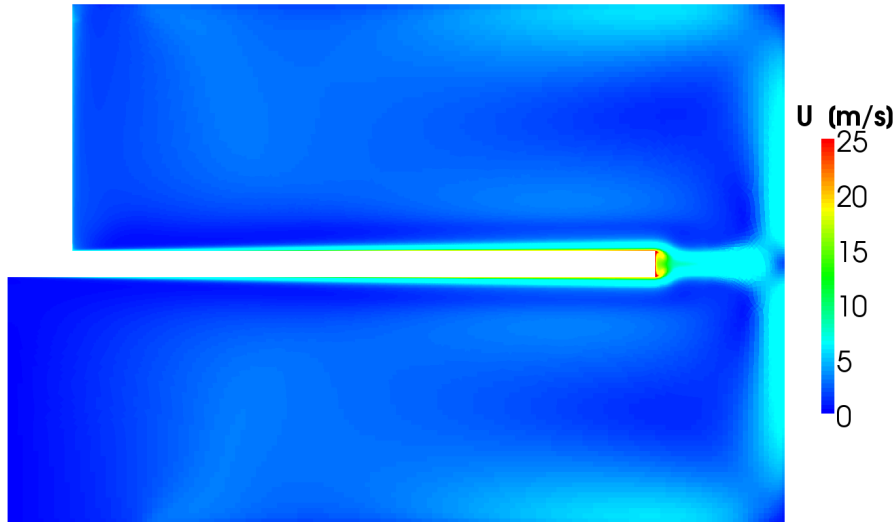


Figure 6.4: Plot of the magnitude of the velocity

of different geometries, the rotational speed of the disc has been set accordingly to achieve a maximum energy dissipation rate (EDR) of the same order. In this comparison, the maximum EDR ranged from 3.8×10^6 to 5.6×10^6 [$W kg^{-1}$] for the different configurations.

After simulating the flow field of the shear device, the Lagrangian particle tracking has been used to determine the EDR profile of the cells in each geometrical configuration (see Subsection 4.2.2). For this purpose, 300 particles have been injected uniformly into the simulation domain.

The simulation runtime for the particle tracking has been fixed to be 1 [s], since the particle tracking simulations took significant time, partly due to the use of the LSD model (see Subsection B.1). The EDR information has been recorded for each particle at every time step in a data file. After the simulation, the output to the particle tracking

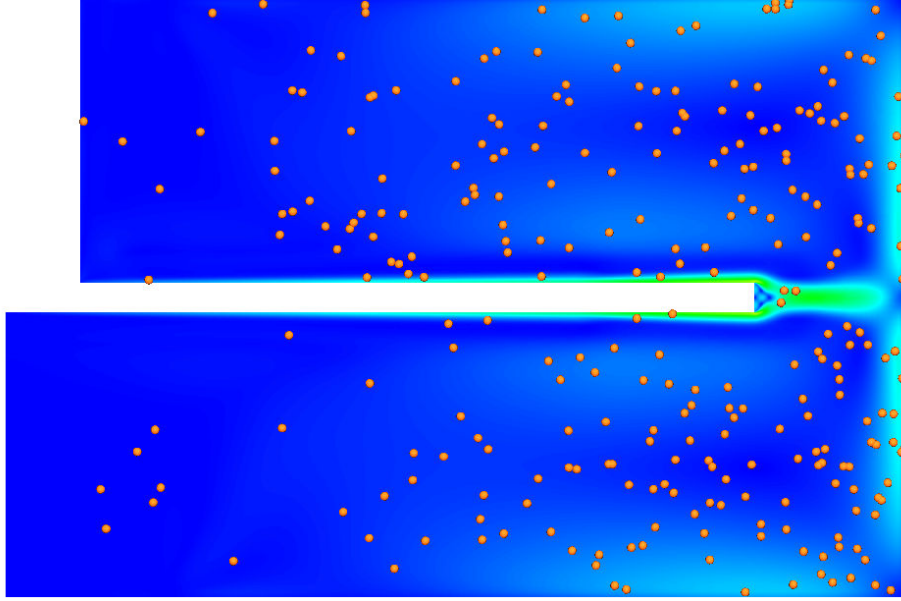


Figure 6.5: Schematic plot of the particle positions during the particle tracking simulation.

data file was processed by using scripts (see Subsection B.2.3). Figure 6.6 illustrates the EDR exposure over time for two particles in the particle tracking simulation. The highest EDR a particle experienced during the particle tracking simulation was filtered out for further analysis. The EDR-range from 0 to 10^7 [$W kg^{-1}$] has been divided into 100 classes using a logarithmic distribution to determine the EDR profiles the cells where exposed to.

Cumulative Distribution

The cumulative distribution chart (compare Figure 6.7) indicates the fraction of particles Q_P which has been exposed to a maximum EDR below a certain EDR level ϵ . It has been calculated using Equation (6.3). N_ϵ is the amount of particles with a maximum EDR below the EDR level of ϵ , and N_{tot} is the total amount of particles.

$$Q_P(\epsilon) = \frac{N_\epsilon}{N_{tot}} \quad (6.3)$$

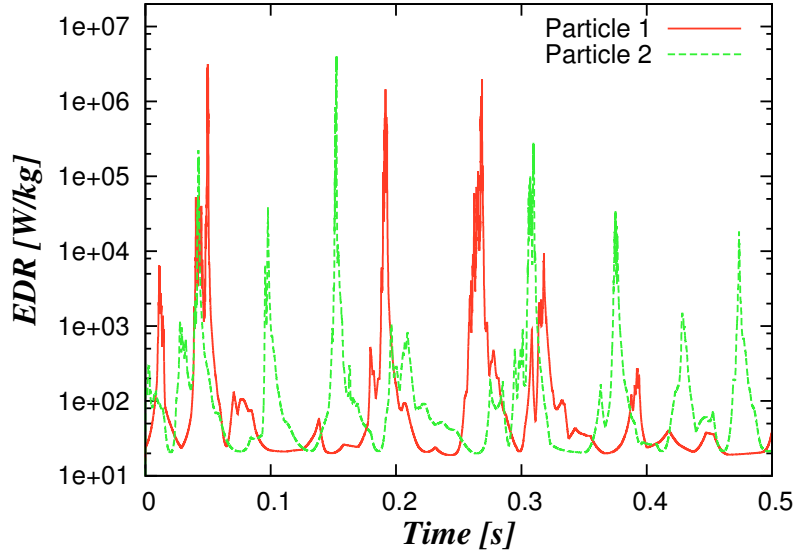


Figure 6.6: EDR exposure over time for two sample particles

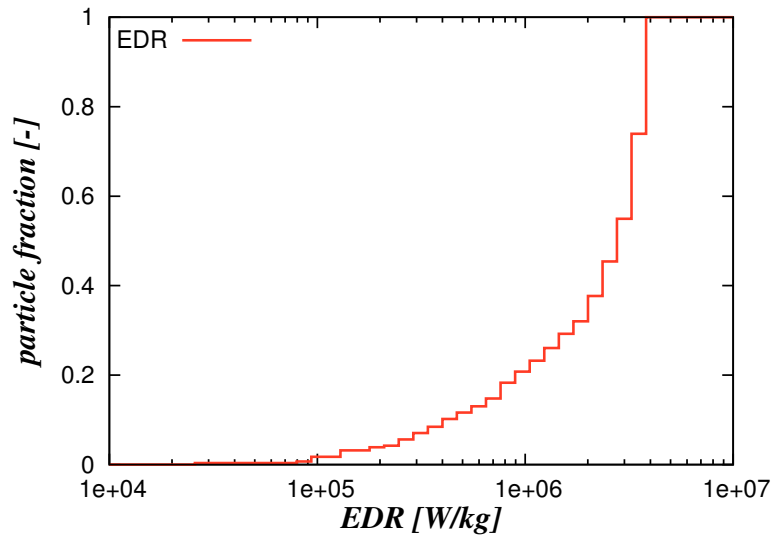


Figure 6.7: Typical cumulative distribution

Frequency Distribution

The frequency distribution chart corresponds to the probability that a cell is exposed to a certain maximum EDR (see Figure 6.8). It has been calculated using Equation (6.4). N_i equals the amount of particles with a maximum EDR within the EDR class i , and $\Delta\epsilon_i$ is the size of the EDR class i .

$$q_P(\epsilon) = \frac{N_i}{N_{tot} \cdot \Delta\epsilon_i} \quad (6.4)$$

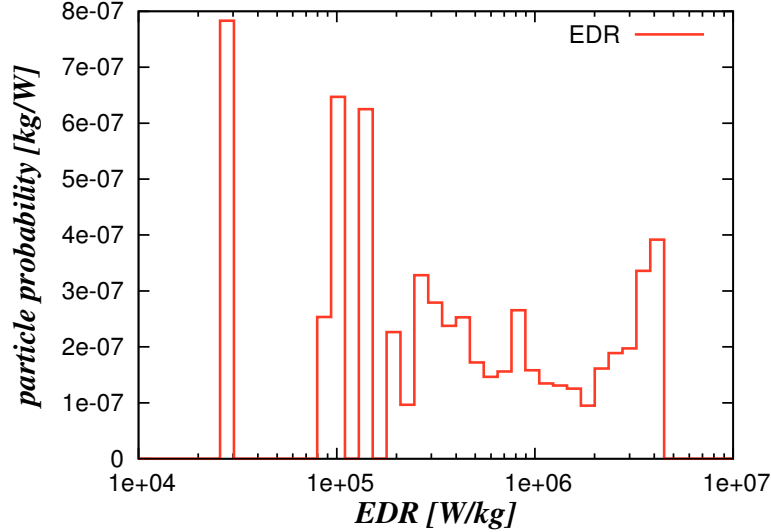


Figure 6.8: Typical frequency distribution chart

6.1.3 Influence of the Computational Mesh

Figure 6.9 and Figure 6.10 show the effect of the grid size on the EDR profile. The cumulative chart indicates that the range of EDR classes containing particles is the same for both meshes (ranging from 2×10^6 to 4×10^6 [$W kg^{-1}$]). The region with the highest occurring EDR is smaller in the mesh with refined cells. This is due to the smaller cells close to the rotating disc in case of a refined mesh and the fact that the EDR level decreases drastically with wall distance. Therefore it is harder for the particles to reach cells with high EDR levels in the refined mesh. This is the reason why the graphs show a shift to the high EDR classes for the unrefined mesh. The peak shifts from 1×10^6 [$W kg^{-1}$] in the simulation with the refined mesh to 4×10^6 [$W kg^{-1}$] for the simulation with the unrefined mesh. 50% of particles are below 1×10^6 [$W kg^{-1}$] for the refined mesh and below 3×10^6 [$W kg^{-1}$] for the unrefined mesh. Thus, it has a strong effect whether a refined or unrefined mesh is used for the analysis of the EDR. Consequently, the following simulations have been performed using an identical mesh spacing to be comparable among each other.

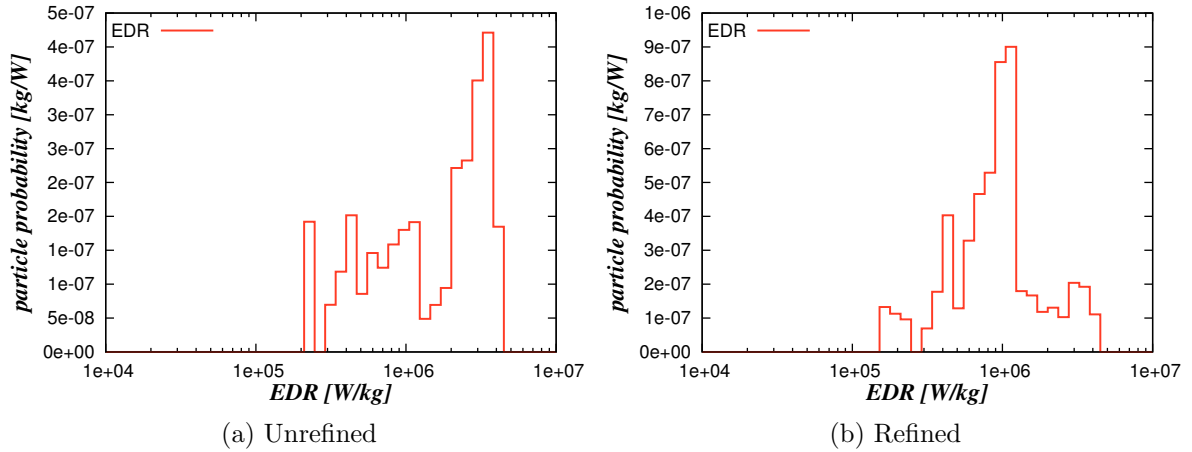


Figure 6.9: Comparison of the effect of the mesh size, frequency distribution (Geom.: $r_{SD} = 40$ [mm], $h_{SD} = 30$ [mm])

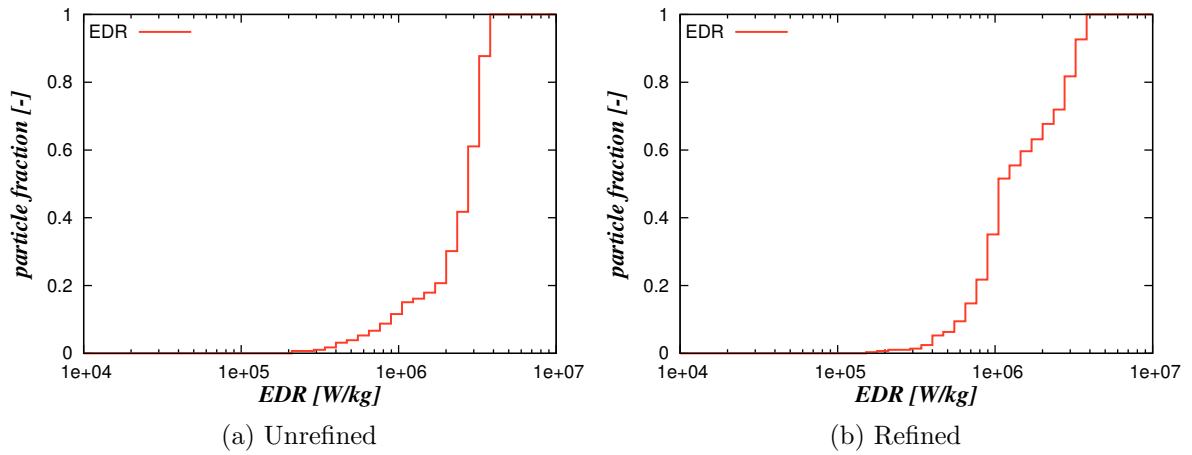
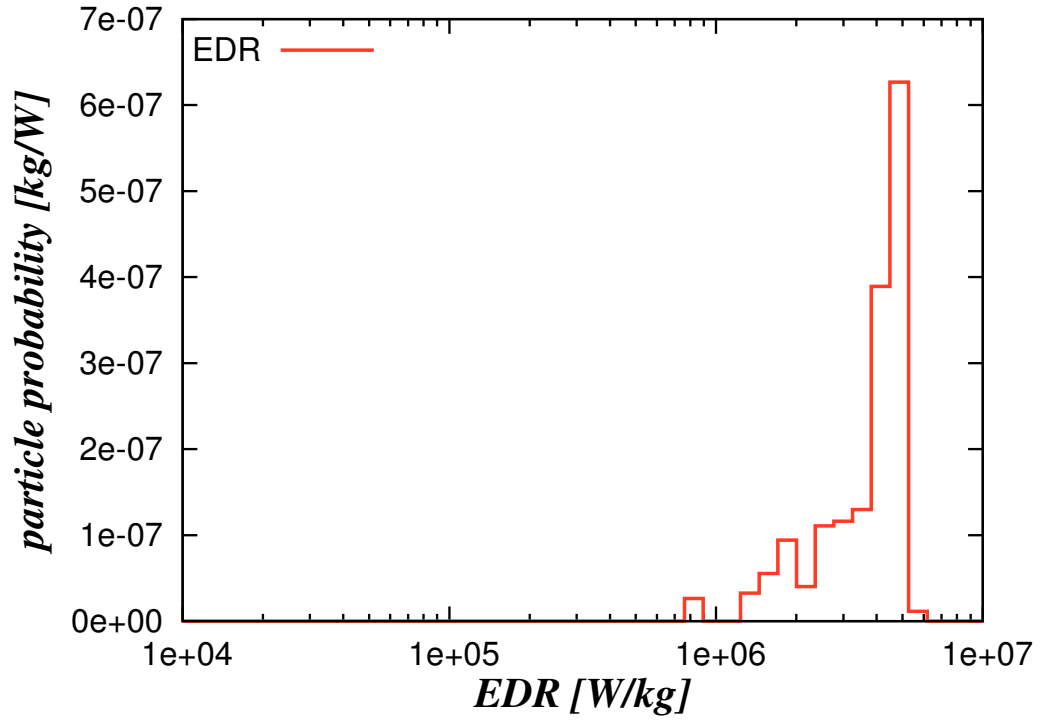
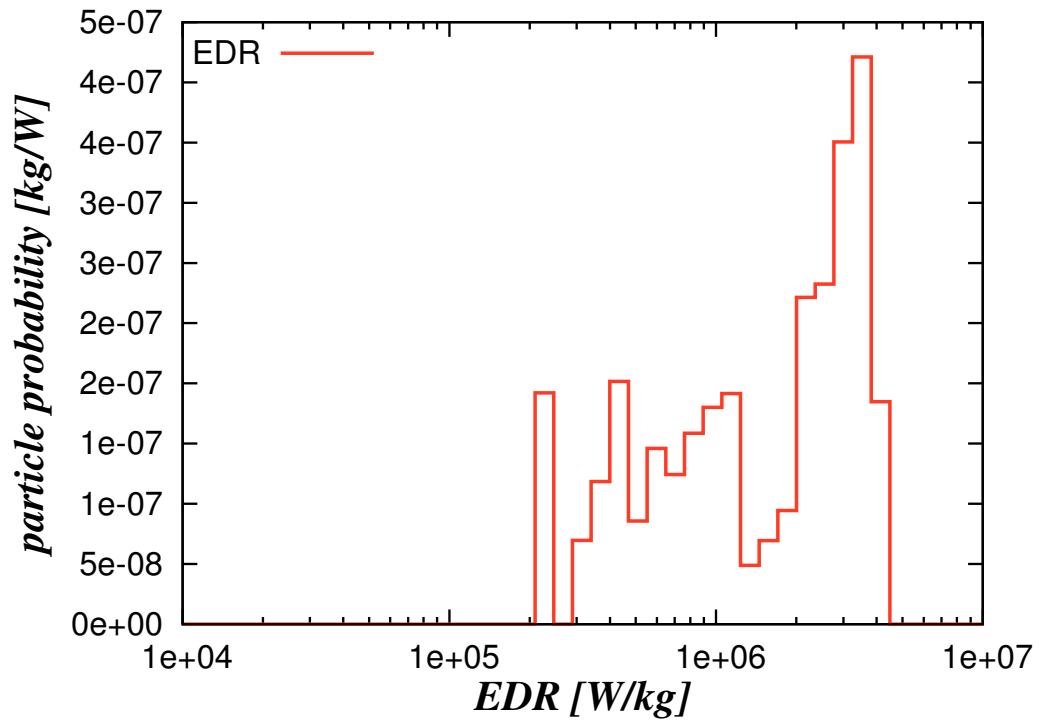
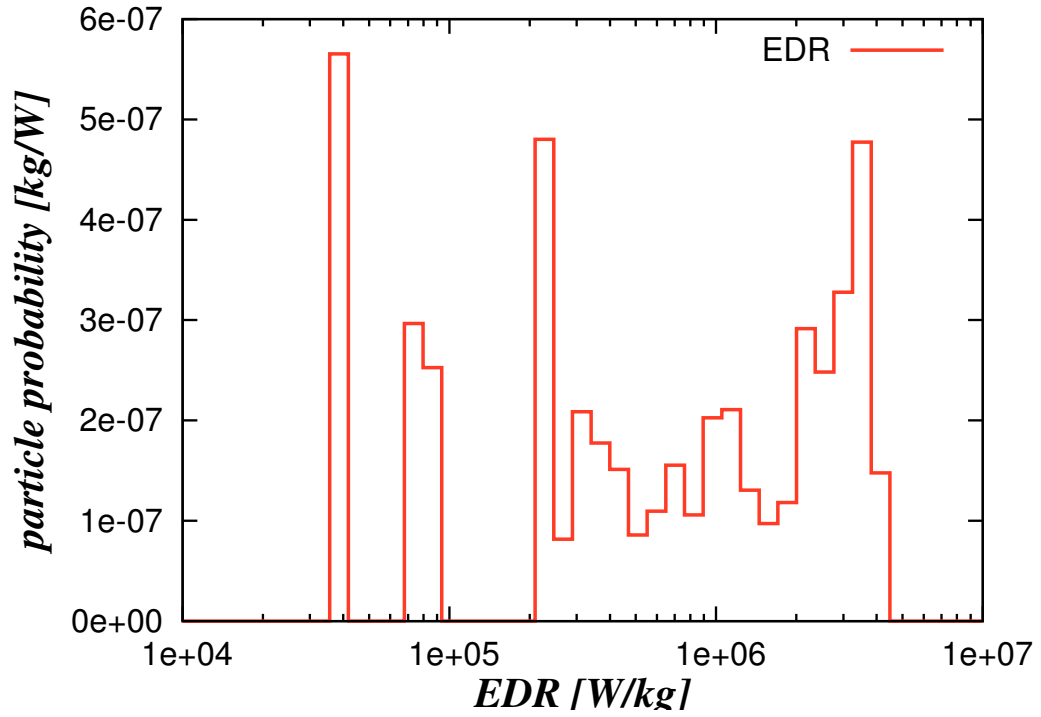
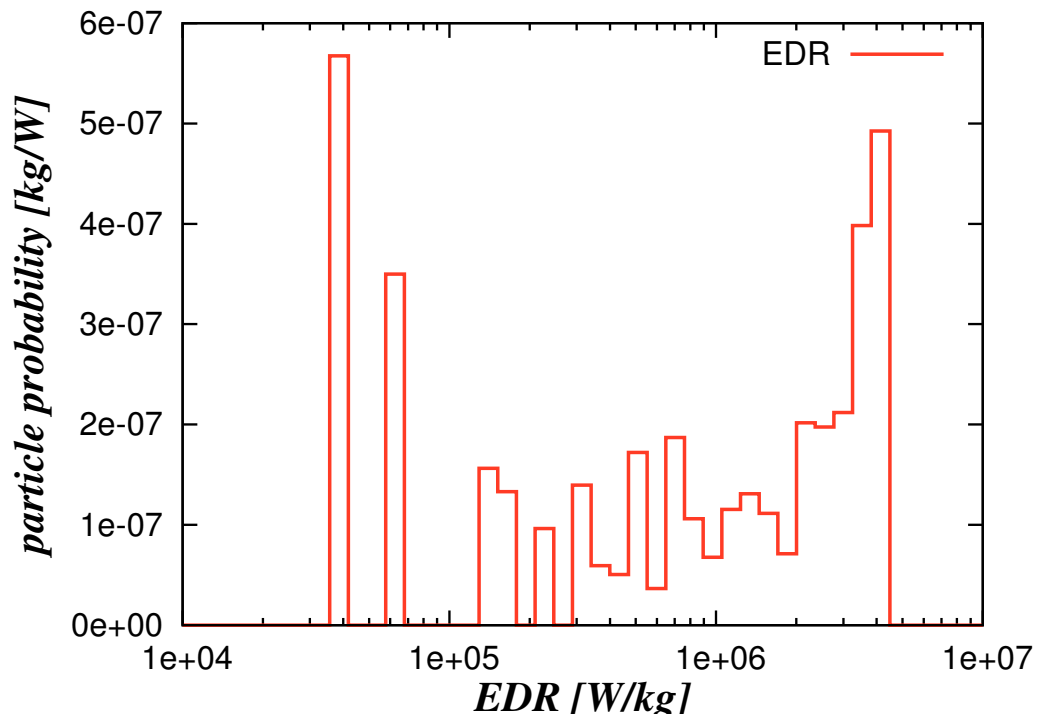


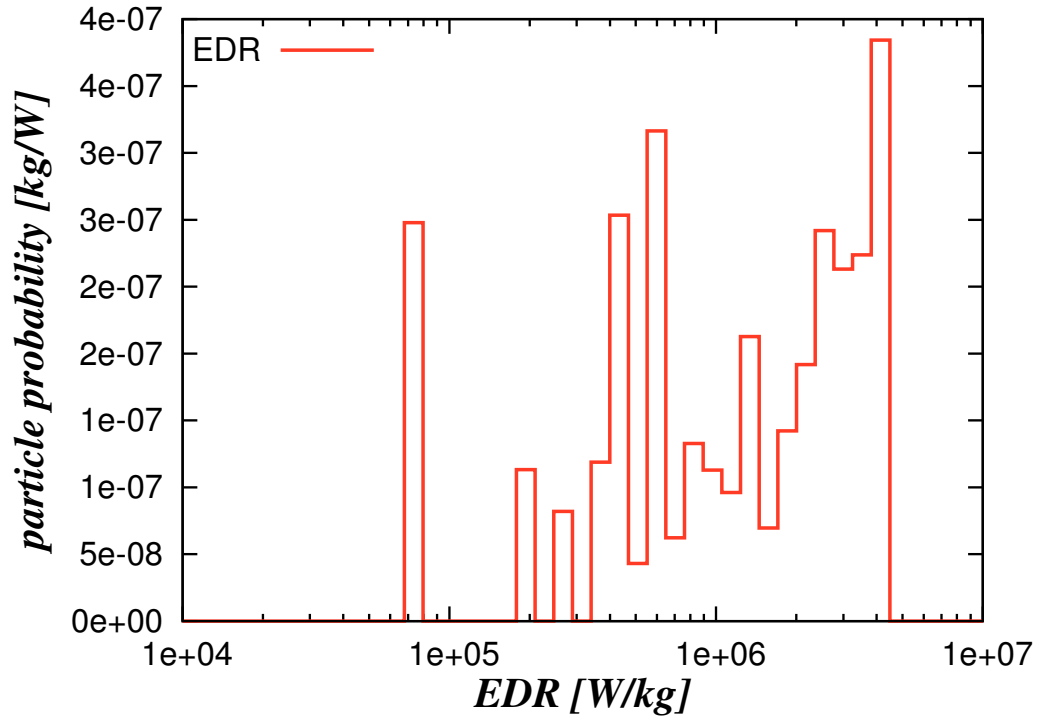
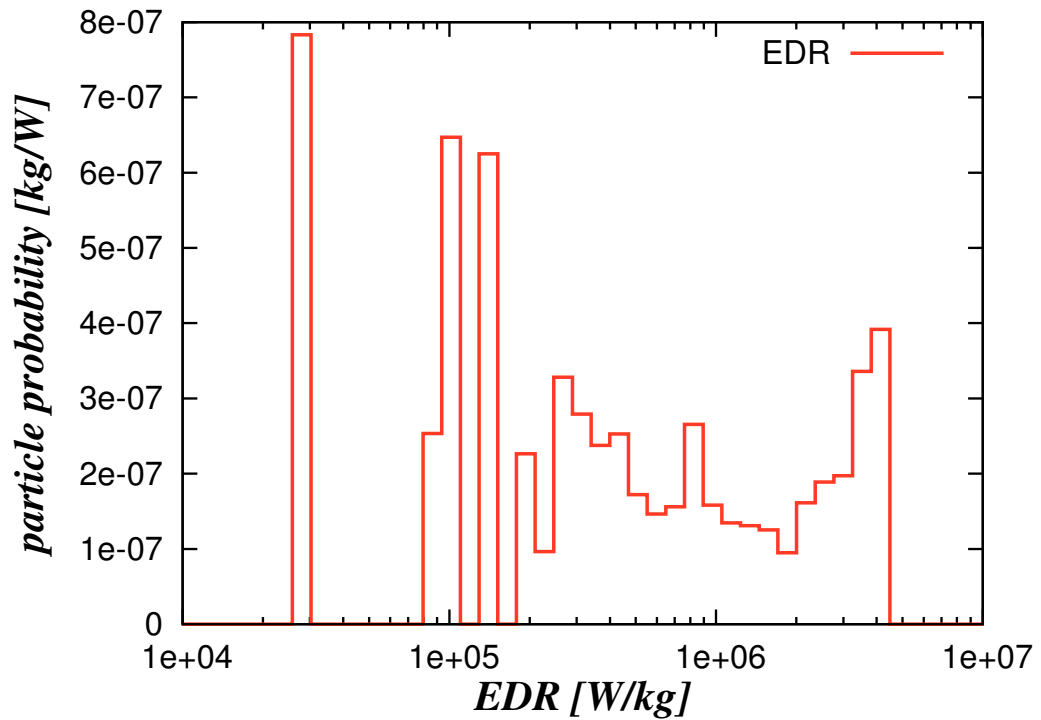
Figure 6.10: Comparison of the effect of the mesh size, cumulative distribution (Geom.: $r_{SD} = 40$ [mm], $h_{SD} = 30$ [mm])

6.1.4 Comparison of Different Geometries

The following charts show the effect of the geometry parameters of the USD on the EDR profile. The EDR profile of smaller geometries is sharper and shifted towards the highest occurring EDR (Figure 6.11). Simulations with a larger geometry (Figure 6.12 to Figure 6.16) showed that the EDR profiles have a wider EDR distribution and a shift towards lower EDR levels. Therefore, smaller geometries show advantages to establish defined conditions in the bio-material.

Figure 6.11: Geometry: $r_{SD} = 30$ [mm], $h_{SD} = 20$ [mm]Figure 6.12: Geometry: $r_{SD} = 40$ [mm], $h_{SD} = 30$ [mm]

Figure 6.13: Geometry: $r_{SD} = 40$ [mm], $h_{SD} = 40$ [mm]Figure 6.14: Geometry: $r_{SD} = 50$ [mm], $h_{SD} = 30$ [mm]

Figure 6.15: Geometry: $r_{SD} = 50$ [mm], $h_{SD} = 40$ [mm]Figure 6.16: Geometry: $r_{SD} = 50$ [mm], $h_{SD} = 50$ [mm]

6.1.5 Geometry of the Shear Device

The final geometrical configuration should give a sharp EDR profile and a short processing time span. The comparison of different sized shear devices indicated that smaller configurations are providing a sharp, more defined energy dissipation rate distribution in the EDR profiles. Nevertheless, the time given for the total process does not allow the use of too small geometries, since there would be not enough time left for handling and centrifugation. The geometry of $r_{SD} = 30 [mm]$ and $h_{SD} = 20 [mm]$ has been chosen as a suitable configuration, since it fulfills the requirements. The plot of the EDR profile (Figure 6.11) shows that the EDR distribution is sharp and concentrated at higher EDR levels. Furthermore, a continuous operated process is possible within the available processing time ($t_{SD} = 35.4 [min]$).

Sensitivity to the Turbulence Model

Since the geometrical configuration of $r_{SD} = 30 [mm]$ and $h_{SD} = 20 [mm]$ has been chosen, a suitable motor has to be found. The required motor output has been determined by running simulations at the same rotational speed using different turbulence models.

The standard k-epsilon, the RNG k-epsilon and the realizable k-epsilon model, all high-Reynolds-number turbulence models, have been used with a coarse mesh. For this purpose, a mesh with a $y+$ close to 30 or higher has been designed. Creating a mesh with an accurate $y+$ alongside all walls is hardly possible for rotating disc cases. Due to slow velocities in the center and high velocities at the tip of the disc some areas are lacking in mesh resolution. The mesh design has been concentrated to be accurate on the region at the tip of the disc. This region shows the highest velocities and energy dissipation rates (EDR), which is the main point of interest. The number of cells in the mesh for the high-Reynolds-number models was about 45,000 cells.

Additionally, the Launder-Sharma low-Reynolds-number model has been used, since it resolves the boundary layer flow in more detail. A different mesh with a high mesh resolution close to the wall is necessary for this model. The used mesh consisted of 362,000 cells, and had an average $y+$ of 0.22 for the walls of the disc and 3 for the cylinder walls. Thus, the resolution in the critical region around the disc is sufficient to resolve the laminar boundary level.

The rotational speed has been set to a rotational speed of $2,500 [rad s^{-1}]$ and the kinematic viscosity was set to $10^{-6} [m^2 s^{-1}]$. In Table 6.2 the results of the simulations involving different turbulence models are summarized. As can be seen, the simulations of the high-Reynolds-number models lead to insignificant differences in the EDR results. However, the low-Reynolds-number model had a more than three times higher maximum EDR. This is due to the fact, that for the low-Reynolds-number model the

mesh resolution was finer and the maximum EDR occurrences were located just in regions close to the tip of the disc.

To determine the required motor output for a particular speed of the disc, the total amount of energy dissipated in the rotating disc device has been calculated. Equation (6.5) gives the required power input for the disc at a certain rotational speed. The multiplication of the volume of a cell V_i with the EDR of the cell ϵ_i and the density of the fluid ρ gives the amount of energy dissipated in the cell. Since the slice has a 5° opening angle, a multiplication by 72 gives the total amount of energy dissipated in the full shear device. A C-program has been written to get the cell information from the simulation (see Subsection B.2.4). Summation over all cells gives the amount of energy dissipated in the slice of the computational mesh.

$$total\ EDR = 72 \times \sum V_i \cdot \epsilon_i \cdot \rho \quad (6.5)$$

As one can see from the results, the low-Reynolds-number model showed an approximately 50% higher value of the total EDR. As a consequence the motor was designed to meet the highest total EDR calculated. Thus, a motor had to be found capable of delivering a power output of at least 262 [W] at a rotational speed of 2,500 [$rad\ s^{-1}$].

	standard k- ϵ	realizable k- ϵ	RNG k- ϵ	Lauder-Sharma
max. EDR [$W\ kg^{-1}$]	$4.7\ 10^6$	$4.7\ 10^6$	$4.4\ 10^6$	$1.6\ 10^7$
total EDR [W]	170	175	174	262

Table 6.2: Results from the total EDR calculations of the shear device simulations

Considerations in Respect to the Motor Output

This requirement of the power output for a continuous process can not be fulfilled with standard DC-motor. The extremely high rotational speeds required cause a very high current (up to 80 [A]) to deliver the necessary power output. Problems are related to the runtime under this high current, because those motors are not designed for long continuous runs. Therefore, the size of the shear device has to be reduced to a size suitable for the power output and rotational speed specifications of the available DC motors. The chosen size of the shear device of $r_{SD} = 30$ [mm] and $h_{SD} = 20$ [mm] had to be replaced by a slightly smaller configuration of $r_{SD} = 25$ [mm] and $h_{SD} = 20$ [mm]. Following the calculations from Section 6.1.1 for this new geometry leads to a total shearing time of $t_{SD} = 50.9$ [min], which leaves enough time for handling and centrifuging.

6.2 Operating Parameters of the Shear Device

6.2.1 Generating the Computational Mesh

To calculate the operating parameters of the shear device, multiple simulations at varied rotational speeds are necessary. The operating parameters for the shear device have been determined by CFD simulations using the Launder-Sharma low-Reynolds-number model to resolve the boundary regions in more detail. The required mesh resolution depends on the flow conditions in the simulated region. Typically, high rotational speeds require a higher resolution of the mesh than slower rotational speeds to achieve an accurate result. Therefore, generating one mesh for a case with a high rotational speed would be appropriate for use with all cases at lower rotational speeds as well. This approach saves time during the generation of the mesh for all cases, but takes more time for running the simulations, since the mesh resolution is higher than necessary for lower rotational speeds.

The mesh has been generated using a *Cubit* journal script, which includes all command sequences for the mesh generation. The mesh has been generated as a slice with a 5° opening angle (compare Subsection 6.1.2). It consists of 325k cells and is refined towards the walls and further refined around the rotating disc (see Figure 6.17). The average y^+ value is below 0.15 for a rotational speed of 24,000 [rpm].

6.2.2 Running the Simulations

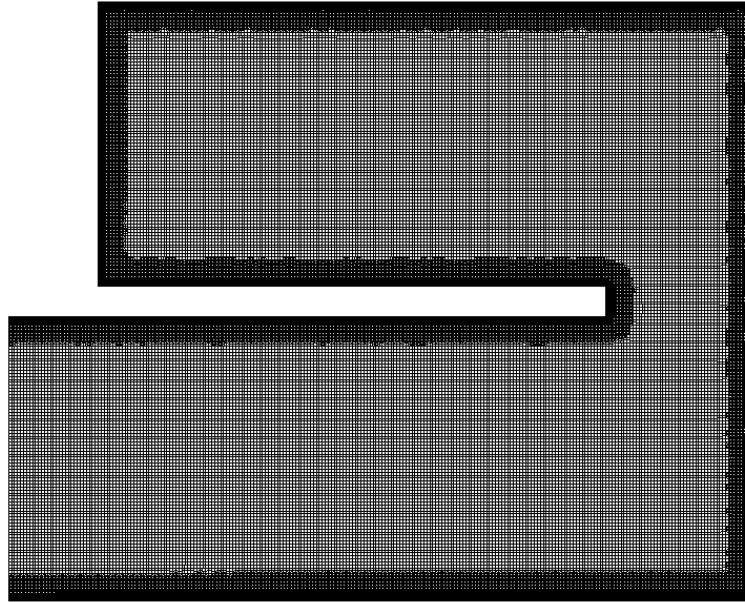
All simulations have been run with the standard k-epsilon turbulence model first to achieve a starting point of the flow field for the low-Reynolds-number model. From there, the Launder-Sharma low-Reynolds-model has been used.

For the low-Reynolds-number model, the velocity on wall patches has been set to $0 [m s^{-1}]$. The pressure has been set to zero gradient for all patches, since this case is a cavity. The wall boundary conditions for k and epsilon have been set to be $10^{-20} [m^2 s^{-2}]$ and $10^{-20} [m^2 s^{-3}]$ to prevent problems due to divisions by 0.

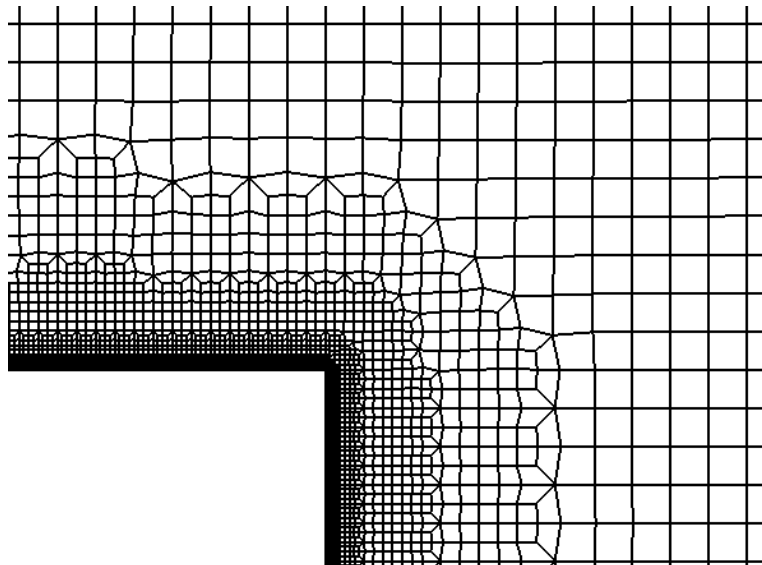
6.2.3 Results of the Simulations

The results from the simulations with the different rotational speeds allow the characterization of the shear device with respect to the power draw characteristic. The operating points for the energy dissipation rate with the corresponding rotational speed are given in Figure 6.18. A smooth curve has been added to the graph by data fitting. The result shows that all points line up close to the data fitted curve.

The power draw of the shear device is shown in Figure 6.19. Also, the power output of the recommended motor is illustrated (Maxon Motor / EC 25 Motor, see Subsection 6.4.2). According to the motor specifications sheet (see Subsection A.1), the power



(a) Unzoomed



(b) Zoomed at the tip of the disc

Figure 6.17: Low Reynolds number mesh of the shear device ($r_{SD} = 25$ [mm], $h_{SD} = 20$ [mm])

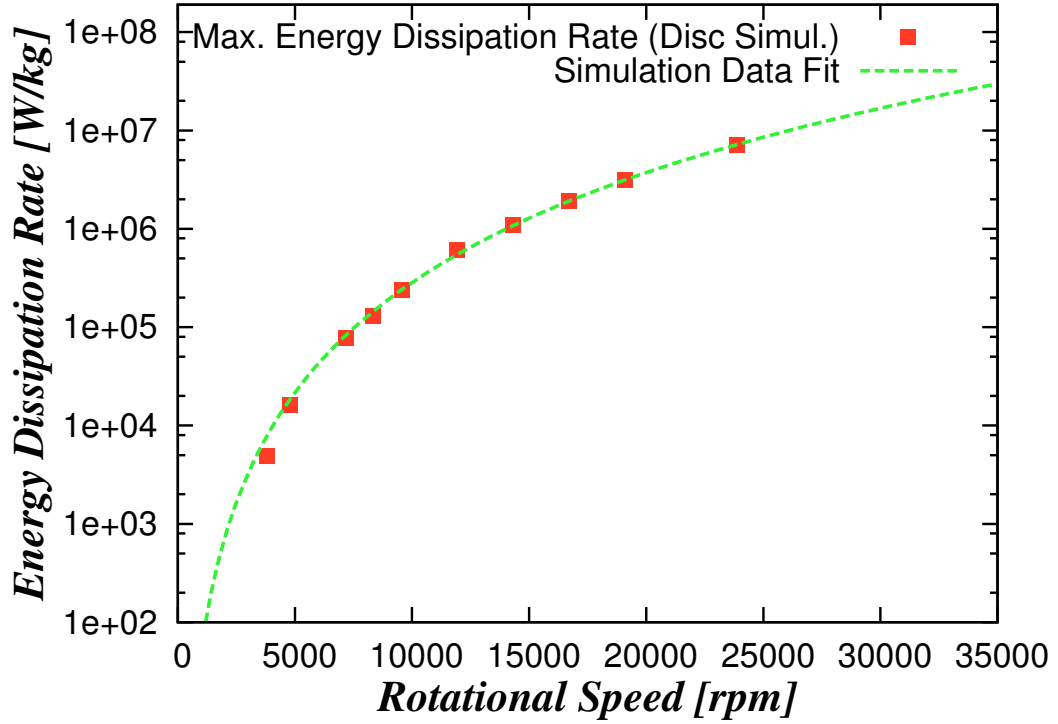


Figure 6.18: Operating parameters of the shear device

output of the motor for continuous operation is characterized by an approximately constant torque of 42 [mNm] for the rotational speeds of interest. Hence, the curve for the power output of the motor can be calculated by multiplication of the torque of the motor with the rotational speed of the motor (see Equation (6.6)).

$$P_{motor}(\omega_{motor}) = 0.042 [Nm] \times \omega_{motor} \quad (6.6)$$

Comparing both lines indicates the range of possible operation, i.e., the region of rotational speeds showing a smaller power consumption of the rotating disc than the motor can deliver.

6.3 Sigma Theory of Equivalent Settling Area

The operating parameters of the laboratory centrifuge have to be determined to match that of the disc stack separator. The performance of the laboratory centrifuge and the separator can be compared by applying the sigma theory of equivalent settling area (Equation (6.7)) [Maybury et al., 2000, Boychyn et al., 2001, 2004].

$$\frac{Q_{ds}}{C_{ds}\Sigma_{ds}} = \frac{V_{lab}}{t_{lab}C_{lab}\Sigma_{lab}} \quad (6.7)$$

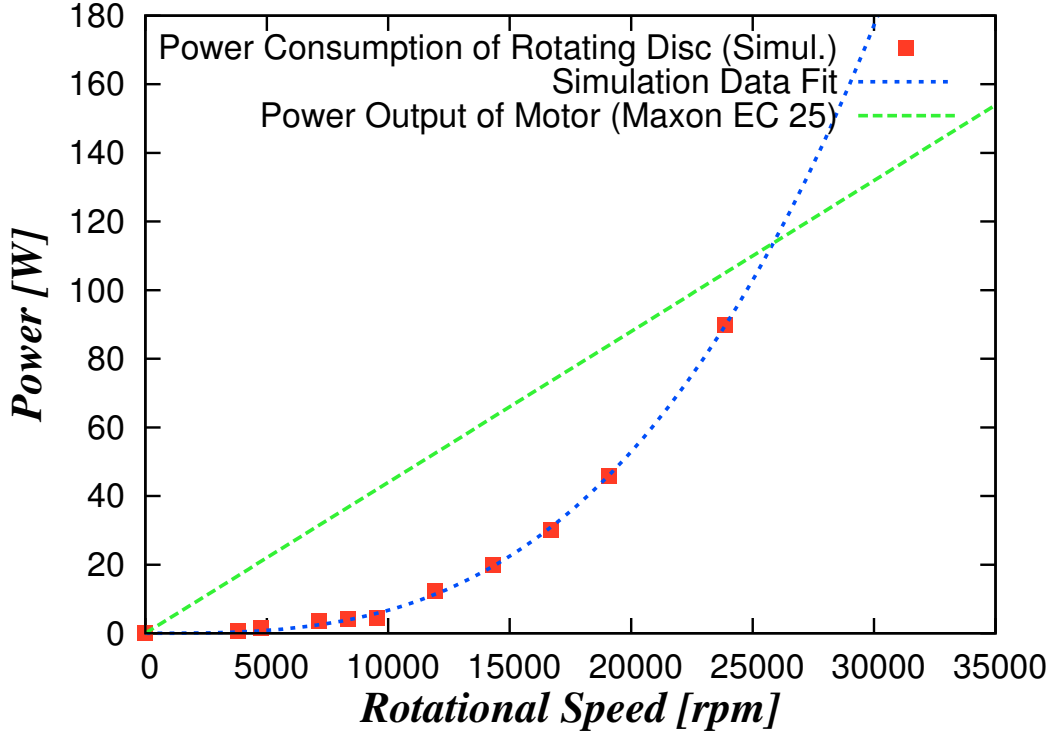


Figure 6.19: Power consumption of the shear device

The left hand side of Equation (6.7) is determined by the volumetric flow rate of the disc stack separator Q_{ds} , the equivalent settling area of the disc stack separator Σ_{ds} and a correction factor for non-ideal flow conditions in the disc stack separator C_{ds} . The right hand side is given by the volume of the sample for laboratory centrifugation V_{lab} , the equivalent settling area of the laboratory centrifuge Σ_{lab} and a correction factor for non-ideal flow conditions. The operating time of the laboratory centrifuge t_{lab} , that gives an identical separation performance as the disc stack separator, can be calculated by transformation of Equation (6.7).

Several assumptions have been made in the derivation of the Sigma theory [Boychyn et al., 2004]. It is assumed that the settling behaviour is laminar, the concentration of the particles is low and therefore hindered settling is not occurring. Furthermore, all particles starting from the lower half of the settling distance will be removed from the suspension. The two correction factors (C_{ds} , C_{lab}) take non-ideal behaviour into account, but they are considered as constants and independent of the varying flow conditions. As a consequence, the Sigma theory should be used only in the linear range of a plot of the clarification against the term $Q/C\Sigma$ in a logarithmic chart. The clarification of a test sample can be calculated by measuring the optical density (OD) of the suspensions of the feed material, the centrifuged test sample and a reference sample Equation (6.8). The reference sample is clear feed material produced by extensive

centrifugation.

$$\text{clarification} = \frac{OD_{feed} - OD_{sample}}{OD_{feed} - OD_{reference}} \quad (6.8)$$

6.3.1 Applying the Sigma Theory to Sandoz' Disc Stack Separator

The settling performance of a separator depends on operational and geometrical parameters. The equivalent settling area of a disc stack separator Σ_{ds} is given by Equation (6.9) [Maybury et al., 1998]. Operational parameters are the angular bowl speed ω_{ds} and the volumetric flow rate of the feed material Q_{ds} . The geometrical parameters are shown in Figure 6.20, where r_1 and r_2 are the inner and outer radii of the discs, n is the number of gaps between the discs and θ is the half conical angle of the discs. The factor F_L takes the reduction of the settling area due to mounting and distance elements between the discs into account (see Equation (6.10)). Z_L is the number of spacers per disc and B_L is the width of a spacer.

$$\Sigma_{ds} = \frac{2\pi n \omega_{ds}^2 (r_2^3 - r_1^3)}{3g \tan \theta} F_L \quad (6.9)$$

$$F_L = 1 - \left(\frac{3Z_L B_L}{4\pi r_2} \right) \left(\frac{1 - (r_1/r_2)^2}{1 - (r_1/r_2)^3} \right) \quad (6.10)$$

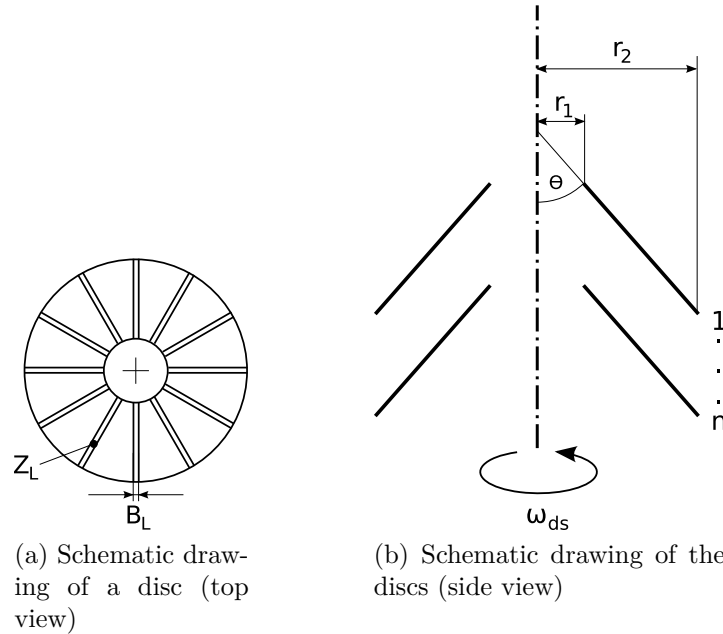


Figure 6.20: Geometrical parameters in the Sigma equation of a disc stack separator

Geometry of Sandoz' Disc Stack Separator

The geometrical parameters have been measured on site at Sandoz in Kundl during a maintenance stop of the disc stack separator [Felber and Radl, 2008]. The results of

D_1	D_2	n	θ	Z_L	B_L
[mm]	[mm]	[$-$]	[$^\circ$]	[$-$]	[mm]
131.5	356	114	35	12	6

Table 6.3: Geometrical details of Sandoz' disc stack separator

the measurements are shown in Table 6.3. The outer diameter of the discs is 360 [mm] including a horizontally bent edge of 2 [mm]. Therefore the outer diameter of the conical shape is $D_2 = 356$ [mm]. The inner diameter is 127.5 [mm] with a horizontally bent edge of 2 [mm] resulting in an inner diameter of the conical shape of $D_1 = 131.5$ [mm]. The total number of discs in the separator is 116, including one gap-less disc, resulting in a number of $n = 114$ [$-$] gaps between the discs. The half conical angle of the discs is $\theta = 35$ [$^\circ$].

Results

Sigma, i.e., the equivalent settling area, can be calculated using the measurements listed above and the given operational parameters. The disc stack separator runs with a rotational speed between 6,800 and 8,000 [rpm] and a mass flow rate of the feed material between 1,000 and 2,500 [$kg h^{-1}$] [Piskernik, 2008]. The correction factor for a disc stack separator ranges from 0.4 to 0.73 [Maybury et al., 2000]. Since the correction factor for Sandoz' separator is not known, it is assumed that it is equal to $C_{ds} = 0.5$. A description for an experimental protocol to determine the correction factor is given in Subsection 6.3.3.

The geometrical details of Sandoz' disc stack separator with Equation (6.10) leads to the factor $F_L = 0.912$ [$-$]. Furthermore the equivalent settling area of the disc stack separator Σ_{ds} [m^2] can be expressed solely depending on the rotational speed ω_{ds} [$rad s^{-1}$] (Equation (6.11)). Table 6.4 shows the equivalent settling area of the disc stack separator and the term $Q_{ds}/C_{ds}\Sigma_{ds}$ (left hand side from Equation (6.7)) for different volumetric feed flow rates and rotational speeds.

$$\Sigma_{ds}(\omega) = 0.170 \cdot \omega_{ds}^2 \quad (6.11)$$

Operating Point	ω_{ds} [$rad\ s^{-1}$]	Σ_{ds} [$10^4\ m^2$]	Q_{ds} [$10^{-4}\ m^3\ s^{-1}$]	$Q_{ds}/C_{ds}\Sigma_{ds}$ [$10^{-9}\ m\ s^{-1}$]
1			2.78	6.45
2	712	8.61	4.86	11.3
3			6.94	16.1
4			2.78	5.45
5	775	10.2	4.86	9.53
6			6.94	13.6
7			2.78	4.66
8	838	11.9	4.86	8.16
9			6.94	11.7

Table 6.4: Results of the equivalent settling area and the term $Q_{ds}/C_{ds}\Sigma_{ds}$ of the disc stack separator for different operating points

6.3.2 Applying the Sigma Theory to the Laboratory Centrifuge

The laboratory centrifuge is running in a batch process. Therefore the runtime has to be determined in order to ensure that the same performance as in the disc stack centrifuge is obtained. The equivalent settling area for a laboratory centrifuge with swing-out rotor and negligible acceleration/deceleration phases is given by Equation (6.12) [Maybury et al., 2000].

$$\Sigma_{lab} = \frac{V_{lab}\omega_{lab}^2}{2g \ln\left(\frac{2r_o}{r_i+r_o}\right)} \quad (6.12)$$

V_{lab} is the volume of the sample material per bottle, ω_{lab} is the rotational speed of the rotor, r_i is the radius to the surface of the sample material and r_o is the radius to the bottom of the bottle in swung-out position.

Specifications of the Laboratory Centrifuge

The model of the laboratory centrifuge which will be used is a Beckman Coulter Avanti J-25 with the JLA-9.1000 rotor [Piskernik, 2008]. The specifications of the centrifuge and the rotor are shown in Table 6.5 [Beckman-Coulter, 2009b] and Table 6.6, respectively [Beckman-Coulter, 2009a]. The JLA-9.1000 rotor is a fixed angle centrifuge rotor with a half conical opening angle of 20° . The bottles have a minimum fill volume (e.g. 1,000 [ml] for the J-LITE PP-1000) which is the same as the nominal fill volume. Therefore the amount of test material used should be chosen in multiples of the nominal fill volume in one tube. For this rotor the nominal amount of fill volume is 1000 [ml]. Counter-weighing can be done with water filled tubes, in case not all tubes are being used with bio-material.

max. speed	$[rpm]$	25,000
max. g	$[m s^{-2}]$	75,600 g
acc./dec. rates	$[-]$	2/3

Table 6.5: Specifications of the laboratory centrifuge (Beckman Coulter Avanti J-25)

capacity	$[ml]$	$4 \times 1,000$
r(min)	$[mm]$	82
r(max)	$[mm]$	185
max. rotor speed	$[rpm]$	9,000
max. g	$[m s^{-2}]$	16,800 g
approx. acceleration time	$[s]$	150
k factor	$[-]$	2,540

Table 6.6: Specifications of the rotor of the laboratory centrifuge (Beckman Coulter JLA-9.1000)

Calculating the Runtime of the Laboratory Centrifuge

The Sigma equations for laboratory centrifuges are derived for swing-out rotor machines only. Therefore the runtime will be calculated for a swing-out rotor analog and then converted to the fixed angle model used by using the manufacturers run time conversion [Beckman-Coulter, 2009c]. As the swing-out analog, the rotor JS-4.0 has been chosen due to the same capacity as the JLA-9.1000 rotor [Beckman-Coulter, 2009a]. The specifications of the JS-4.0 rotor are shown in Table 6.7.

capacity	$[ml]$	$4 \times 1,000$
r(min)	$[mm]$	86
r(max)	$[mm]$	226
max. rotor speed	$[rpm]$	4,000
max. g	$[m s^{-2}]$	4,050 g
approx. acceleration time	$[s]$	90
k factor	$[-]$	1,5300

Table 6.7: Specifications of the swing-out analog rotor of the laboratory centrifuge (Beckman Coulter JS-4.0)

For a centrifuge bottle filled to the maximum capacity, the radius to the surface of the sample material r_i equals the radius r(min) of the specification. With a constant rotational speed of $\omega_{lab} = 4,000 [rpm]$ and the maximum sample volume of $V_{lab} = 1,000 [ml]$, the equivalent settling area Σ_{lab} can be calculated. Inserting in Equation (6.12) leads to an equivalent settling area of the analog rotor of $\Sigma_{lab} = 24.1 [m^2]$. The correction factor for non-ideal flow conditions in laboratory centrifuges is $C_{lab} = 1 [-]$

[Maybury et al., 2000]. Now the run time of the laboratory centrifuge can be calculated by transforming Equation (6.7) to Equation (6.13). The term of the laboratory centrifuge parameters gives $V_{lab}/\Sigma_{lab}C_{lab} = 4.14 \cdot 10^{-5} [m]$.

$$t_{lab} = \frac{V_{lab}C_{ds}\Sigma_{ds}}{C_{lab}\Sigma_{lab}Q_{ds}} \quad (6.13)$$

Then the results of the run time for the swing-out analog rotor have to be converted to the fixed angle rotor. By using k-factors, a runtime conversion between different rotors is possible by using Equation (6.14) [Wilson and Walker, 2000]. The runtime conversion between different rotor types is not accurate. Therefore experiments to verify the operating parameters are suggested.

$$t_1 = t_2 \frac{k_1}{k_2} \quad (6.14)$$

On the homepage of the manufacturer, a conversion sheet between different types of rotors is available [Beckman-Coulter, 2009c]. After choosing the rotor types, the k-factor for each rotor is displayed for a given rotational speed. For the JS-4.0 rotor and a rotational speed of 4,000 [rpm] the k-factor is equal to $k_2 = 15,296.1$, and for the JLA-9.1000 rotor and a rotational speed of 9,000 [rpm] a k-factor of $k_1 = 2,544.4$ is obtained. By inserting the k-factors, the runtime can now be converted by Equation (6.15).

$$t_1 = 0.166 \cdot t_2 \quad (6.15)$$

A summary of the results of the run time calculations for different operating points is shown in Table 6.8 and Table 6.9. These results are valid for the given parameters only, and results for different operating parameters have to be calculated separately. For example, changing the rotational speed of the laboratory centrifuge leads to a different k-factor. Thus the equation of the runtime conversion is different. Also, a change in the volume of the sample material or a different tube or rotor model leads to different radii and consequently different values for the equivalent settling area.

Operating Point	ω [rpm]	ω [rad s ⁻¹]	Q_{ds} [kg h ⁻¹]	Q_{ds} [10 ⁻⁴ m ³ s ⁻¹]
1			1,000	2.78
2	6,800	712	1,750	4.86
3			2,500	6.94
4			1,000	2.78
5	7,400	775	1,750	4.86
6			2,500	6.94
7			1,000	2.78
8	8,000	838	1,750	4.86
9			2,500	6.94

Table 6.8: Parameter settings at different operating points

Operating Point	$t_{lab}(JS - 4.0)$ [10 ³ s]	$t_{lab}(JLA - 9.1000)$ [10 ³ s]	$t_{lab}(JLA - 9.1000)$ [min]
1	6.42	1.07	18
2	3.67	0.611	10
3	2.57	0.427	7
4	7.61	1.27	21
5	4.35	0.723	12
6	3.04	0.506	8
7	8.89	1.48	25
8	5.08	0.845	14
9	3.56	0.592	10

Table 6.9: Summary of the results of the run time calculations

Run Time Calculation with Acceleration and Deceleration

The process of batch centrifuging has starting and ending phases with a rotational speed being lower than the nominal operating speed. For shorter run-times and/or long acceleration and deceleration stages, the time for acceleration and deceleration should be taken into account, since the settling performance during speed-up and slowing down is lower than running at operational speed [Maybury et al., 2000]. Equation (6.16) takes the acceleration and deceleration stages into account. The parameters x and y represent the fraction of acceleration and deceleration time of the total runtime, respectively. They are calculated by $x = t_{acc}/t_{tot}$ and $y = t_{dec}/t_{tot}$.

$$\Sigma_{lab} = \frac{(3 - 2x - 2y) V_{lab} \omega_{lab}^2}{6g \ln\left(\frac{2r_o}{r_i + r_o}\right)} \quad (6.16)$$

Comparing Equation (6.12) with Equation (6.16) shows that the difference between the two equations is the term $(3 - 2x - 2y) / 3$. According to the manufacturers centrifuge catalog [Beckman-Coulter, 2009a], the acceleration time is approximately $t_{acc} = 150$ [s]. The required time for deceleration is not given and therefore it is assumed to be the same as for acceleration $t_{dec} = 150$ [s]. Using $t_{lab}(JLA - 9.100)$ from Table 6.9 as an approximation for the total runtime t_{tot} leads to x and y . Furthermore, the runtime $t_{lab,ad}(JLA - 9.1000)$ including acceleration and deceleration stages can be calculated by dividing $t_{lab}(JLA - 9.1000)$ by the additional term $(3 - 2x - 2y) / 3$. The results are shown in Table 6.10. Since the period until the rotor reaches the operating speed is independent from the runtime, the acceleration and deceleration phases have more significance the shorter the total runtime of the centrifuge is.

Operating Point	$t_{lab}(JLA - 9.1000)$ [min]	$t_{lab,ad}(JLA - 9.1000)$ [min]
1	18	22
2	10	15
3	7	13
4	21	25
5	12	17
6	8	14
7	25	29
8	14	18
9	10	15

Table 6.10: Comparison of the runtime of the laboratory centrifuge without and with the acceleration and deceleration phases

6.3.3 Experimental Determination of the Correction Factor of the Disc Stack Separator

The correction factor for non-ideal flow conditions depends on the model of the centrifuge. It can be determined experimentally by running the centrifuge of interest and a laboratory centrifuge as a reference at multiple operating points [Boychyn et al., 2000]. The clarification performance of the experimental runs has to be analyzed (e.g. using optical density measurements). Then the percentage of clarification for each run can be calculated by Equation (6.8). The results can be expressed in data points consisting of the term $V_{lab}/t_{lab}\Sigma_{lab}C_{lab}$ for the laboratory centrifuge with the corresponding percent of clarification. The data points for the disc stack separator consist of the term $Q_{ds}/\Sigma_{ds}C_{ds}$ and the corresponding percentage of clarification. Since all parameters except C_{ds} are known, and $C_{lab} = 1$ as a reference, the correction factor of the disc stack separator can be determined by data fitting of C_{ds} .

6.4 Specifications of the Ultra Scale-Down Process

This chapter contains recommendations for the key process components and the operating conditions. Since it is a recommendation, changes can be made in respect of compatibility. E.g., depending on already available laboratory equipment on site, an adaption of the components can be made accordingly.

6.4.1 Tube Pump

A tube pump has been chosen to pump the fluid through the process, due to its capability of delivering a constant volumetric flow rate. Additionally, the possibility of driving multiple tubes with one pump is given. This is an advantage regarding the flexibility of the process layout. In case the USD process is run in parallel with more than one shear device, or a cooling medium has to be pumped through the shear device, using a single pump is possible.

The MCP Process tube pump from Ismatec would be a suitable pump for this purpose. Its specifications are shown in Table 6.11 and can be found online [Ismatec, 2009]. This model has the possibility of running programs prepared on a personal computer, which could be an advantage when a tuning of the process is necessary. Different pump heads and various tubes in different size and materials, are also available from Ismatec.

Manufacturer/Model	Ismatec / MCP Process Tubing Pump
Component number	P001
Price	~ 4,000 €
Flow rates	0.001 – 3,700 [$ml\ min^{-1}$] (depending on pump-head)
Channels	1 – 24 (depending on pump-head)
Size (D x W x H)	220 × 155 × 260 [mm]
Comments	programmable command sequences

Table 6.11: Specifications of the tube pump

The tubes should be of the size of the inlet to the shear device (4 – 5 [mm] inner diameter). The material of the tube has to be suitable for pharmaceutical purposes. Table 6.12 shows a recommended example. Additionally, connection parts are required to connect the tubes with different parts of the process.

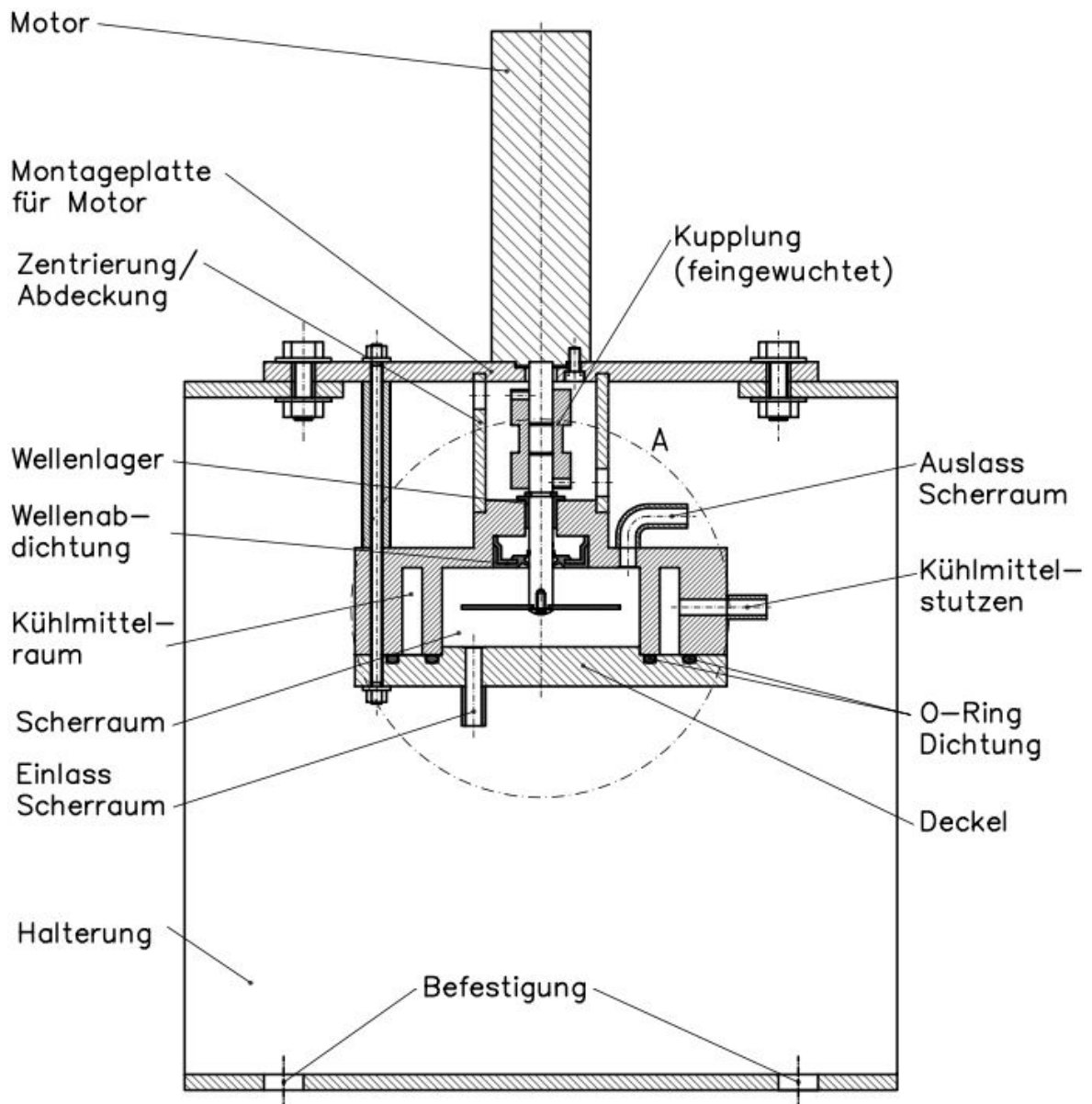


Figure 6.21: Schematic drawing of the shear device assembly

Manufacturer/Model	Ismatec / MF001 Tubes
Component number	P002
Material	Pharmed (suitable for sterile operation)
Size	4.8 [mm] diameter 1.6 [mm] wall thickness
Comments	connection parts required additionally

Table 6.12: Specifications of the tube pump tubes

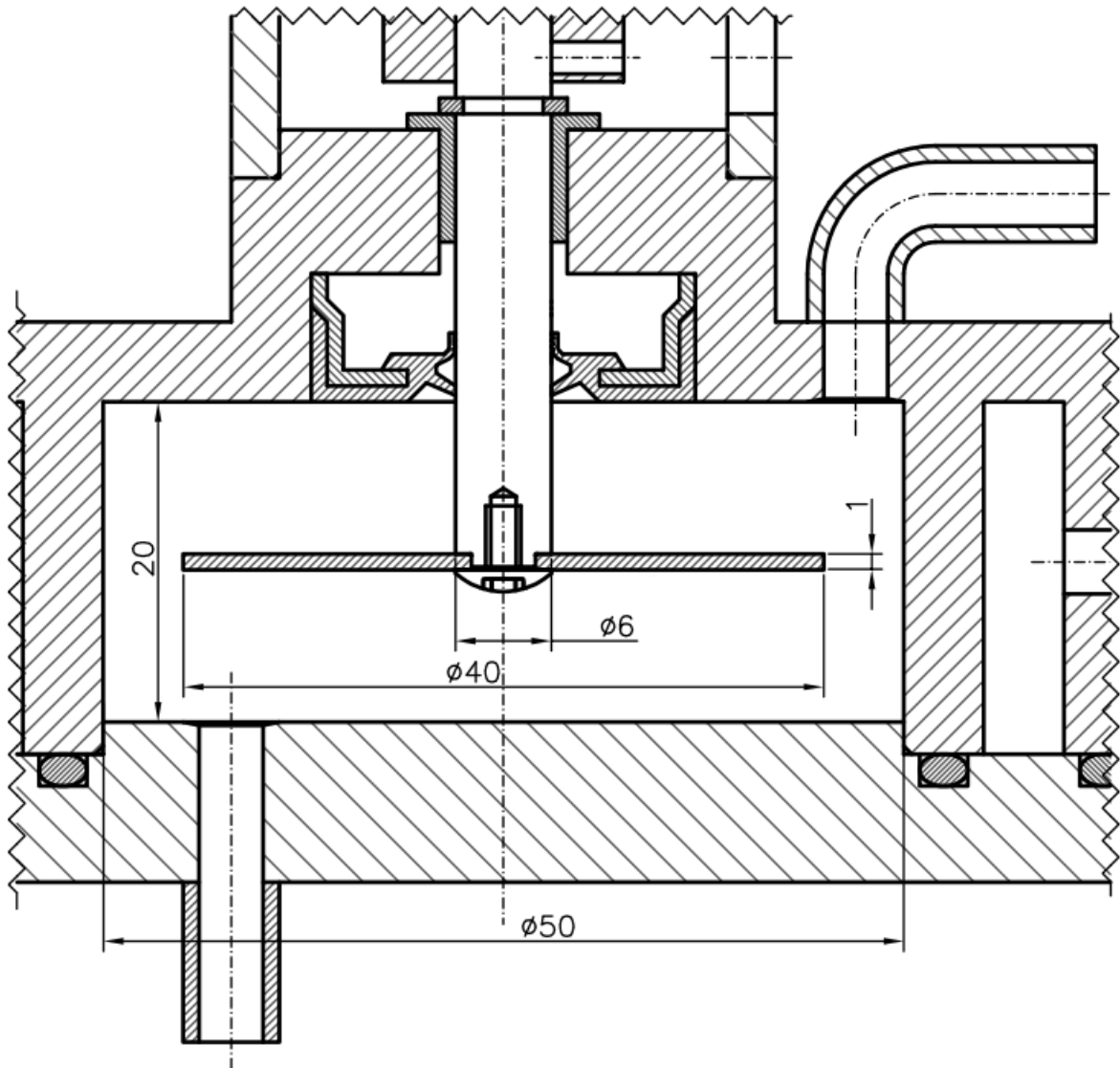


Figure 6.22: Schematic drawing of the shear device assembly, details shearing chamber (measurements in [mm])

6.4.2 Shear Device

The design of the shear device assembly is illustrated in Figure 6.21. The shearing chamber has a radius of $r_{SD} = 25$ [mm] and a height of $h_{SD} = 20$ [mm]. It is embedded in a suitable housing, which is providing mounting holes for the shaft bearing, shaft seal, inlet and outlet connections for the bio-material. An annular gap with connections for a cooling medium provides a cooling jacket to cool the shearing device. The positions of the inlet and outlet connections are important. The outlet should be on the top allowing air removal, and the radial position of the inlet and outlet to the center should be equal. The shear device would pump material through the outlet, if the outlet is positioned farther away from the center than the inlet. The bottom is closed via a cylindrical plate containing a O-ring sealing for the shearing chamber and the cooling medium. The whole shear device can be easily disassembled and allows for a fast and easy cleaning of the device.

The rotating disc has a diameter of $r_d = 40$ [mm] and a thickness of $s_d = 1$ [mm], and is positioned in the center of the shearing chamber. It is mounted on a shaft with a flat screw providing the possibility for disc changes. The shaft should be designed to allow for an accurate centering of the discs and perpendicular alignment with the shaft. The connection to the motor shaft is made with an appropriate coupling.

A cylindrical covering for the coupling unit and hollow bolts ensure correct positioning of the motor above the shearing chamber. The motor is secured on a plate and long screws through the hollow bolts lock the bottom of the the shearing chamber together with the motor mounting plate. The motor mounting plate is screwed on a construction providing a proper connection to a workbench.

DC Motor

There are only a few options regarding the choice of the motor, since it has to deliver a high power output at an adequate range of rotational speed. Using a motor for model sports cars or model aeroplanes, which was used by an other group [Boychyn et al., 2001], would not be possible for this project. Those motors are designed to run with the low voltage range from battery packs at about 2.4–7.2 [V]. Higher power output is solely possible by increasing the current. The maximum current needed would exceed 80 [A] for some models to achieve higher power output. Therefore, such a motor is not suitable for continuous use, since a current in this range would overheat and destroy the motor. Furthermore, power supplies for continuous high current output are massive devices, costly and not very flexible.

Another possibility would be to use a strong motor with speed transformation. Due to the increase of complexity regarding additional equipment and components, speed transformation is not an ideal choice.

Manufacturer/Model	Maxon Motor / EC 25 Motor
Component number	M001
Price	476.06 €
Power output	250 [W]
Nominal voltage	36 [V]
Nominal speed	61,600 [rpm]
Nominal torque (max. continuous)	42.4 [mNm]
Nominal current (max. continuous)	8.1 [A]
Ambient temperature	-20... + 100 [°C]
Size specification	diameter 25 [mm], length 83.5 [mm]
Shaft	diameter 6 [mm], length 16.1 [mm]

Table 6.13: Specifications of the Maxon EC 25 motor

A suitable motor solution could be found in the Maxon Motor EC 25 motor which shows the required characteristics. The specifications of the motor are shown in Table 6.13 (see Subsection A.1 for the data sheet). Compared to the motors, the Maxon EC 25 has a significantly higher nominal voltage. Therefore, the current is kept in a lower range for the same power output. This model combines several features, since it is small in size, rotating at high speeds and has a high power output. Additionally, there is the possibility to use the motor controllers from the same manufacturer (shown in Table 6.14).

The power supply should correspond to the required specifications according to the motor controller. The recommended power supply is shown in Table 6.15.

Manufacturer/Model	Maxon Motor / DEC 70/10 Controller
Component number	M002
Price	356.54 €
Operating voltage	10... 70 [V]
Continuous current	10 [A]
Max. rotational speed	80,000 [$U \text{ min}^{-1}$]
Ambient temperature	-10... + 45 [°C]
Size (L x W x H)	120 × 103 × 27 [mm]

Table 6.14: Specification of the Maxon DEC 70/10 speed and current controller for the motor

Manufacturer/Model	Elektro Automatik / EA-PS 880-40 R
Component number	M003
Price	1,048.00 €
Operating voltage	0 ... 80 [V]
Continuous current	0 ... 40 [A]
Max. power output	1,000 [W]
Ambient temperature	-10 ... + 45 [°C]
Size (W x H x D)	90 × 240 × 400 [mm]

Table 6.15: Specifications of the power supply model EA-PS 880-40 R

The connection between the shaft of the motor and the rotating disc can be solved using a small coupling device. An example is shown in Table 6.16, which is suitable for extreme rotational speeds.

Manufacturer/Model	R+W / MK2 Serie 5 Coupling
Component number	M004
Torque	0.5 [Nm]
Max. rotational speed	90,000 [$U \text{ min}^{-1}$] (fine balanced)
Ambient temperature	-30 ... + 120 [°C]
Size	Length 25 [mm], outer diameter 15 [mm] Inner diameter 6 [mm]

Table 6.16: Specification of the coupling of the motor shaft (MK2 Serie 5 Coupling)

6.4.3 Cooling of the Shear Device

The rotating disc in the shear device increases the temperature of the bio material due to the dissipated energy from the power output of the motor. The possibility of cooling is integrated in the design of the shear device (compare Figure 6.21). Tubes can be connected to pump a cooling medium through the narrow annular gap around the main chamber. The following calculations show an estimation of the temperature conditions for cooling.

Estimation of the Temperature Increase of the Bio-Material Flow

An explanatory calculation has been conducted with an assigned power output of the motor of $P_{motor} = 75$ [W]. It has been assumed that the power output of the motor is completely converted into heat ($P_{motor} = \dot{Q}_{motor}$) and that it is solely heating up the bio material flow. Therefore, the heat capacity of the chamber and the heat transfer to the environment has not been considered (compare Figure 6.23). This estimation leads to the maximum possible temperature increase of the bio material flow for a certain

motor power output level (i.e., the energy transfer due to cooling is neglected as well, $\dot{Q}_{cool} = 0$ [W]).

The energy balance is given by the heat input of the motor \dot{Q}_{motor} and the temperature increase ΔT_{USD} of the bio material with a mass flow rate of \dot{m}_{USD} through the shear device (Equation (6.17)). The heat capacity of the fluid is assumed to be close to the heat capacity of water ($c_{p,USD} = 4,200$ [J kg⁻¹K⁻¹]). With a volumetric flow rate of $\dot{V}_{USD} = 170$ [ml min⁻¹] and a density of $\rho_{USD} = 1,000$ [kg m⁻³] of the bio material, the mass flow rate becomes $\dot{m}_{USD} = 0.170$ [kg min⁻¹]. The temperature increase can be calculated by transforming Equation (6.17) to Equation (6.18).

$$\dot{Q}_{motor} = \dot{m}_{USD} \cdot c_{p,USD} \cdot \Delta T_{USD} \quad (6.17)$$

$$\Delta T_{USD} = \frac{\dot{Q}_{motor}}{\dot{m}_{USD} c_{p,USD}} = \frac{75}{\frac{0.170}{60} \cdot 4200} = 6.3 \text{ [K]} \quad (6.18)$$

The resulting temperature differences are shown in Table 6.17 depending on the power output of the motor for a given mass flow rate of $\dot{m}_{USD} = 0.170$ [kg min⁻¹].

The result shows that cooling has to be considered depending on the tolerated temperature increase. A further increase of the temperature in the bio material can be achieved by reducing the mass flow rate through the shear device at a constant power output of the motor (e.g., by an increase in the average residence time of the bio material in the shear device).

\dot{P}_{motor} [W]	5	10	25	50	75	100	150	200
ΔT_{USD} [K]	0.4	0.8	2.1	4.2	6.3	8.4	12.6	16.8

Table 6.17: Temperature increase of the fluid flow through the shear device dependent on the power output of the motor ($\dot{m}_{USD} = 0.170$ [kg min⁻¹])

Estimation of the Required Temperature Difference for Cooling

The final design of the prototype assembly of the shear device is planned by Sandoz, and therefore, several assumptions have to be made to calculate the temperature conditions for cooling.

The energy balance for the cooling of the shear device is given by Equation (6.19), and illustrated in a schematic drawing of the problem in Figure 6.23. The left hand side shows the energy flow into the system and the right hand side shows the energy flowing out of the system. The bio material flow enters the shear device at a temperature of $T_{i,USD}$ and exits it with a tolerated temperature increase of $\Delta T_{USD} = 0.5$ [K]. The term \dot{Q}_{cool} equals the amount of energy required for cooling.

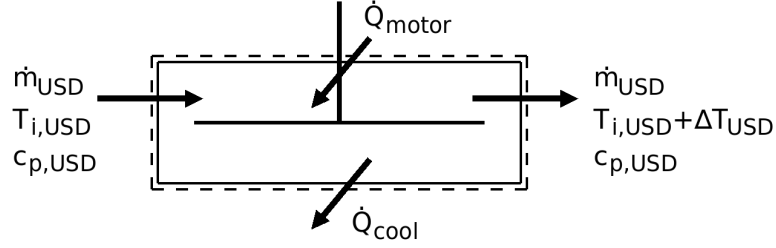


Figure 6.23: Schematic drawing of the temperature conditions in the shear device

$$\dot{m}_{USD} \cdot c_{p,USD} \cdot T_{i,USD} + \dot{Q}_{motor} = \dot{m}_{USD} \cdot c_{p,USD} \cdot (T_{i,USD} + \Delta T_{USD}) + \dot{Q}_{cool} \quad (6.19)$$

Using the parameters $\dot{m}_{USD} = 0.118 \text{ [kg min}^{-1}\text{]}$, $\dot{Q}_{motor} = 75 \text{ [W]}$ and $c_{p,USD} = 4,200 \text{ [J kg}^{-1}\text{K}^{-1}\text{]}$ leads to a required power for cooling of $\dot{Q}_{cool} = 69.05 \text{ [W]}$.

\dot{Q}_{cool} has to be transferred from the inside of the shear device to the wall and from the wall to the cooling medium. The available area for the heat transfer is assumed to be the cylindrical wall of the chamber. This assumption is due to the space required for connections and the assembly of the shear device on the top and bottom of the chamber (see Figure 6.21). With a radius of $r_{SD} = 25 \text{ [mm]}$ and a height of $h_{SD} = 20 \text{ [mm]}$ the cylindrical area of the inner surface gives $A_i = 3142 \text{ [mm}^2\text{]}$. With a thickness of the wall of $s_{wall} = 5 \text{ [mm]}$, the outer cylindrical surface becomes $A_o = 3770 \text{ [mm}^2\text{]}$. Then, the logarithmic averaged cylindrical surface of $A_m = 3446 \text{ [mm}^2\text{]}$ can be calculated, taking the wall thickness into account:

$$A_m = \frac{A_o - A_i}{\ln(A_o/A_i)} \quad (6.20)$$

The thermal conductivity of the wall material has been assumed to be $\lambda_{wall} = 15 \text{ [W m}^{-1}\text{K}^{-1}\text{]}$ for a 1.4301 stainless steel suitable for pharmaceutical purposes [Euro-Inox, 2010]. The required temperature difference of the cooling medium is estimated by assuming perfect heat transfer from the bio material to the wall (i.e. $\alpha_i = \infty \text{ [W m}^{-2}\text{K}^{-1}\text{]}$). This assumption is reasonable, since the flow condition inside of the chamber of the shear device is highly turbulent. On the cooling side, the heat transfer coefficient is assumed to be $\alpha_o = 500 \text{ [W m}^{-2}\text{K}^{-1}\text{]}$. The k-value can be calculated according to Equation (6.21), and gives $k = 429 \text{ [W m}^{-2}\text{K}^{-1}\text{]}$. k for cooled stirred tanks is typically in the range from 150 to 1200 $\text{[W m}^{-2}\text{K}^{-1}\text{]}$ for liquid phases [VDI, 2006].

$$k = \frac{1}{\frac{1}{\alpha_i} + \frac{s_{wall}}{\lambda_{wall}} + \frac{1}{\alpha_o}} \quad (6.21)$$

The average temperature of the cooling medium $T_{m,cool}$ follows by transforming Equa-

tion (6.22), with the average temperature of the bio material calculated from $T_{m,USD} = T_{i,USD} + \Delta T_{USD}/2$. Assuming a temperature of the feed material of $T_{i,USD} = 10$ [°C] leads to an average temperature of the cooling medium of $T_{m,cool} = -37.7$ [°C].

$$\dot{Q}_{cool} = k \cdot A_m \cdot (T_{m,USD} - T_{m,cool}) \quad (6.22)$$

$$\dot{Q}_{cool} = \dot{m}_{cool} \cdot c_{p,cool} \cdot \Delta T_{cool} \quad (6.23)$$

Furthermore, the required mass flow rate can be calculated from Equation (6.23). The heat capacity for the cooling medium is assumed to be similar to water and equal to $c_{p,cool} = 4,200$ [J kg⁻¹K⁻¹]. Choosing a narrow temperature difference between the inlet and outlet temperature of the cooling medium, this leads to the required mass flow rate of the cooling medium. With a design temperature difference of $\Delta T_{cool} = 0.5$ [K], a mass flow rate for the cooling medium of $\dot{m}_{cool} = 2.03$ [kg min⁻¹] results. The inlet temperature of the cooling medium gives should be $T_{i,cool} = -38$ [°C] to allow the desired mean temperature of the cooling medium $T_{m,cool}$.

Discussion of the Results

Cooling of the system has to be considered depending on the tolerated temperature increase of the bio material flow through the shear device. In case of a motor output of $P_{Motor} = 75$ [W] the maximum temperature increase without cooling is $\Delta T_{USD} = 6.3$ [K]. In this scenario a mass flow rate of the cooling medium of $\dot{m}_{cool} = 2.03$ [kg min⁻¹] at an inlet temperature of $T_{i,cool} = -38$ [°C] is required. This calculation is based on a total conversion of the power output of the motor to heat. Due to the assumptions in the calculation, the temperature increase of the bio material during laboratory experiments is expected to be lower. Cooling might not be necessary for certain parameter configurations, but nevertheless the conditions should be checked by measurements.

6.4.4 Accessories

Additionally, secondary components are necessary for the process, which do not need as detailed specifications as the components listed above. These parts include two containers to hold the feed material for the process input and to collect the bio material after processing. Furthermore, additional parts are required to adjust the process parameters. Basically, controlling the process can be done in two different ways. One way is to connect the components to a personal computer and control the process with appropriate software. In this case a PC with a suitable interface to connect the motor and the tube pump is necessary. The benefit of this option is that the whole process control is programmable and open to automation. It would, for example, also allow a

changing rotational speed of the rotating disc or flow rate of the tube pump over time according to a predefined parameter curve. Therefore, fine tuning of the outcome of the process is easy. The other way is to build a control interface, including electronic parts like a display, switches, etc., to adjust the parameters manually. This approach requires intervention by hand for the setup of the process and changing of parameters. Nevertheless, an upgrade with a programmable personal computer can be made at any time, and the programming of command sequences might not be necessary for a satisfactory result.

7 Conclusions and Outlook

7.1 Conclusions

In this work, an ultra scale-down process for the performance prediction of Sandoz' disc stack separator has been designed. After literature review, the key influences on the process behaviour have been analyzed on both scales, which lead to the proposed USD approach. The operating parameters of the USD have been determined based on a CFD analysis for the full-scale separator and the shear device. The Sigma theory of equivalent settling area has been used to design the laboratory centrifuge. Furthermore, the shear device assembly has been designed, and a proposal for the key components of the process has been made. To verify the applicability of the determined operating parameters, a comparison of the process results is recommended, since several assumptions had to be made in the calculations.

The EDR levels occurring in the entrance region of the disc stack separator have been of the order of $10^5 [W kg^{-1}]$, and the rotational speed of the separator bowl, as expected, was the key influence on the resulting EDR level. Compared to the Viscon nozzles, the EDR levels have been significantly lower. An EDR of the order of $10^9 [W s^{-1}]$ and above occurred in the Viscon nozzle simulations. Furthermore, the EDR of droplet impact on the separator housing, due to the ejection from the radial exit nozzles, has been estimated. The estimated EDR ranged up to $10^9 [W s^{-1}]$, strongly depending on the droplet diameter. These results, showing high EDR levels, are an indication of the weak points of the disc stack separator regarding cell destruction.

The properties of the outlet material of the ultra scale-down process can be altered by several possibilities. The rotational speed of the disc, the average residence time in the shear device and the centrifugation time of the laboratory centrifuge can be manipulated to mimic different operating conditions of the full-scale separator. Thus, the degree of cell stress and the separation characteristics can be controlled separately in the proposed USD device. Additionally, further tuning of the process can be done by splitting the considered time for shearing into smaller time intervals and applying different rotational speeds of the disc during each interval. Furthermore, changes of the geometry of the rotating disc (i.e. the diameter and the thickness) can easily be made by replacing it with a differently sized substitute disc.

7.2 Outlook

By an adaption of the operating parameters, the ultra scale-down process can also be used to mimic the characteristics of other disc stack separators or centrifuges. The adaption can be done based on a CFD analysis of the chosen separator, like it has been shown in this work, or experimentally. Matching the results of the USD process with

the results from the chosen process leads to new settings of the operating parameters of the USD process. The settling behaviour of a chosen process can be determined according to the Sigma theory of equivalent settling area.

Future work may deal with an extension of the ultra scale-down process with additional miniature devices. For example, other downstream processing elements could be integrated in the USD device (e.g., a device reproducing the surface impact of liquid jets) This could lead to an even more complete replica of the full-scale process.

References

- Beckman-Coulter. High performance centrifuges catalog br-8102n-e, July 2009a. URL <http://www.beckmancoulter.com/resourcecenter/labresources/centrifuges/br-8102.asp>.
- Beckman-Coulter. Avanti j series centrifuge systems, July 2009b. URL <http://www.beckmancoulter.com/>.
- Beckman-Coulter. Run time conversion using k-factors, July 2009c. URL <http://www.beckman.com/resourcecenter/labresources/centrifuges/runtimecon.asp>.
- R.B. Bird, W.E. Stewart, and E.N. Lightfoot. *Transport Phenomena*. John Wiley & Sons, 2002.
- M. Boychyn, W. Doyle, M. Bulmer, J. More, and M. Hoare. Laboratory scaledown of protein purification processes involving fractional precipitation and centrifugal recovery. *Biotechnol Bioeng*, 69(1):1–10, Jul 2000.
- M. Boychyn, S.S.S. Yim, P.A. Shamlou, M. Bulmer, J. More, and A. Hoare. Characterization of flow intensity in continuous centrifuges for the development of laboratory mimics. *Chemical Engineering Science*, 56(16):4759–4770, 2001. URL [ISI:000170930600005](https://doi.org/10.1016/S0009-2509(01)00005-5).
- M. Boychyn, S.S.S. Yim, M. Bulmer, J. More, D.G. Bracewell, and M. Hoare. Performance prediction of industrial centrifuges using scale-down models. *Bioprocess and Biosystems Engineering*, 26(6):385–391, December 2004. URL [ISI:000226088400005](https://doi.org/10.1002/226088400005).
- A.W. Cense, M.E.H. van Dongen, B. Gottenbos, A.M. Nuijs, and S.Y. Shulepov. Removal of biofilms by impinging water droplets. *Journal of Applied Physics*, 100, 2006.
- CFD-Online. Low-Reynolds number models, 2010. URL http://www.cfd-online.com/Wiki/Low-Re_k-epsilon_models.
- G. Chan, A.J. Booth, K. Mannweiler, and M. Hoare. Ultra scale-down studies of the effect of flow and impact conditions during e-coli cell processing. *Biotechnology and Bioengineering*, 95(4):671–683, November 2006. URL [ISI:000241264300012](https://doi.org/10.1002/241264300012).
- Horst Chmiel. *Bioprozesstechnik*. Elsevier GmbH, München, 2. edition, 2006.
- R. Clift, J.R. Grace, and M.E. Weber. *Bubbles, drops and particles*. Academic Press, 1978.

- Euro-Inox. Stainless Steel: Tables of Technical Properties, 2010. URL http://www.euro-inox.org/pdf/map/Tables_TechnicalProperties_EN.pdf.
- M. Felber and S. Radl. Measurements on site, October 2008. Sandoz, Kundl.
- J.H. Ferziger and M. Peric. *Computational Methods for Fluid Dynamics*. Springer-Verlag, 3rd edition, 2002.
- Gnuplot, 2008. URL <http://www.gnuplot.info/>.
- D.M. Hartley and P.Y. Julien. Boundary shear stress induced by raindrop impact. *Journal of Hydraulic Research*, 30:341–359, 1992.
- Klaus A. Hoffmann and Steve T. Chiang. *Computational Fluid Dynamics*. Engineering Education System, 2000.
- Ismatec. Specifications mcp process, 2009. URL http://www.ismatec.com/int_e/pumps/t_mcp_bvp/mcp_proc.htm.
- Stefan Martens. Blockvorlesung Strömungsmechanik und Stoffaustausch. TU Graz, 2008.
- J. P. Maybury, K. Mannweiler, N. J. Titchener-Hooker, M. Hoare, and P. Dunnill. The performance of a scaled down industrial disc stack centrifuge with a reduced feed material requirement. *Bioprocess and Biosystems Engineering*, 18(3):191–199, March 1998. URL <http://dx.doi.org/10.1007/s004490050430>.
- J.P. Maybury, M. Hoare, and P. Dunnill. The use of laboratory centrifugation studies to predict performance of industrial machines: Studies of shear-insensitive and shear-sensitive materials. *Biotechnology and Bioengineering*, 67(3):265–273, February 2000. URL [ISI:000084740000002](http://www.isi.com/ISI:000084740000002).
- C. Mundo, M. Sommerfeld, and C. Tropea. Droplet-wall collisions - experimental studies of the deformation and breakup process. *International Journal of Multiphase Flow.*, 21:151–173, 1995.
- Octave. Octave 3.0.1, 2008. URL <http://www.gnu.org/software/octave/>.
- OpenCFD Ltd. OpenFOAM 1.5, 2008. URL <http://www.opencfd.co.uk/openfoam/index.html>.
- D.W. Perry, R.H.; Green, editor. *Perry's Chemical Engineers' Handbook (7th Edition)*. McGraw-Hill Professional, 1997.
- Piskernik. Data window of operations, December 2008. Private communication.

- Sandia National Laboratories. Cubit 11.1, 2008. URL <http://cubit.sandia.gov/>.
- Hermann Schlichting and Klaus Gersten. *Grenzschicht-Theorie*. Springer-Verlag, Berlin, 10. auflage edition.
- VDI. *VDI W/"armeatlas*. Springer-Verlag, 2006.
- W. Wang, Y. Huang, M. Grujicic, and D.B. Chrisey. Study of impact-induced mechanical effects in cell direct writing using smooth particle hydrodynamic method. *Journal of Manufacturing Science and Engineering-Transactions of the Asme*, 130, 2008.
- Westfalia, 2010. URL <http://www.westfalia-separator.com>.
- Keith Wilson and John M. Walker. *Principles and techniques of practical biochemistry*. Cambridge University Press, 2000.

Appendix

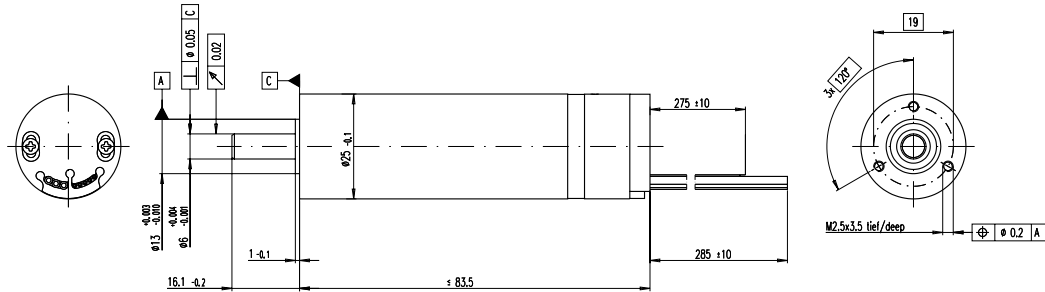
A Components of the Ultra Scale-Down Process

A.1 Data Sheets of Components

EC 25 Ø25 mm, bürstenlos, 250 Watt
High Speed

NEW

maxon EC motor



M 3:2

- Lagerprogramm
- Standardprogramm
- Sonderprogramm (auf Anfrage)

Bestellnummern

351144

Motordaten

Werte bei Nennspannung		
1	Nennspannung	V 36
2	Leerlaufdrehzahl	min ⁻¹ 64000
3	Leerlaufstrom	mA 316
4	Nenn-drehzahl	min ⁻¹ 61600
5	Nennmoment (max. Dauer-drehmoment)	mNm 42.2
6	Nennstrom (max. Dauerbelastungsstrom)	A 8.1
7	Anhaltmoment	mNm 1430
8	Anlaufstrom	A 266
9	Max. Wirkungsgrad	% 93
Kenndaten		
10	Anschlusswiderstand Phase-Phase	Ω 0.135
11	Anschlussinduktivität Phase-Phase	mH 0.014
12	Drehmomentkonstante	mNm A ⁻¹ 5.36
13	Drehzahlkonstante	min ⁻¹ V ⁻¹ 1780
14	Kennliniensteigung	min ⁻¹ mNm ⁻¹ 44.9
15	Mechanische Anlaufzeitkonstante	ms 2.57
16	Rotorträgheitsmoment	gcm ² 5.45

Spezifikationen

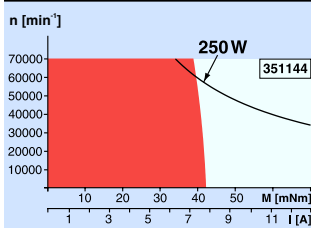
Thermische Daten		
17	Therm. Widerstand Gehäuse-Luft	6.52 KW ⁻¹
18	Therm. Widerstand Wicklung-Gehäuse	0.331 KW ⁻¹
19	Therm. Zeitkonstante der Wicklung	1.61 s
20	Therm. Zeitkonstante des Motors	331 s
21	Umgebungstemperatur	-20 ... +100°C
22	Max. Wicklungstemperatur	+125°C
Mechanische Daten (vorgespannte Kugellager)		
23	Grenzdrehzahl	70000 min ⁻¹
24	Axialspiel bei Axiallast < 8 N	0 mm
	> 8 N	max. 0.14 mm
25	Radialspiel	0.025 mm
26	Max. axiale Belastung (dynamisch)	7 N
27	Max. axiale Aufpresskraft (statisch)	120 N
	(statisch, Welle abgestützt)	5650 N
28	Max. radiale Belastung, 5 mm ab Flansch	20 N
Weitere Spezifikationen		
29	Polpaarzahl	1
30	Anzahl Phasen	3
31	Motorgewicht	210g

Motordaten gemäss Tabelle sind Nenndaten.

Anschlüsse, Motor (Kabel AWG 22)

- rot Motorwicklung 1
- schwarz Motorwicklung 2
- weiss Motorwicklung 3
- grün V_{max} 4.5 ... 24 VDC
- blau GND
- rot / grau Hall-Sensor 1
- schwarz / grau Hall-Sensor 2
- weiss / grau Hall-Sensor 3

Betriebsbereiche



Legende

- Dauerbetriebsbereich**
Unter Berücksichtigung der angegebenen thermischen Widerstände (Ziffer 17 und 18) und einer Umgebungstemperatur von 25°C wird bei dauernder Belastung die maximal zulässige Rotortemperatur erreicht = thermische Grenze.
- Kurzzeitbetrieb**
Der Motor darf kurzzeitig und wiederkehrend überlastet werden.
- Typenleistung**

maxon-Baukastensystem

Übersicht Seite 16 - 21

Empfohlene Elektronik:
DEC 70/10 Seite 295
Hinweise 20

Der DEC 70/10 (Digital EC Controller) ist ein kompakter 4-Quadranten-Verstärker zur Ansteuerung von elektronisch kommutierten Gleichstrommotoren mit einer Leistung von bis zu 700 Watt.

Der bürstenlose Motor muss mit Hallsensoren ausgerüstet sein. Es wird somit kein zusätzlicher Encoder benötigt. Der 4-Q-Betrieb ermöglicht ein kontrolliertes Beschleunigen und Abbremsen der Motorwelle, mit einem gegenüber 1-Q-Verstärkern signifikant besseren Regelverhalten.



Per DIP-Schalter können folgende drei Betriebsarten ausgewählt werden:

- Hall-Sensoren-Drehzahlregler (Drehzahl > 1'000 min⁻¹)
- Spannungssteller mit IxR Kompensation
- Stromregler (Drehmomentregler)

Zum Einstellen des Sollwertes bieten sich folgende Möglichkeiten:

- Analoge Sollwertvorgabe +/- 10 V zur direkten Ansteuerung, beispielsweise mit SPS
- Vorgabe zweier Sollwerte mittels interner Potentiometer

Durch den grossen Eingangsspannungsbereich von 10-70 VDC zeigt sich die DEC 70/10 sehr flexibel in Kombination mit verschiedensten Speisungen. Das kompakte Aluminiumgehäuse und die trennbaren Schraubklemmen erlauben eine einfache Montage.

Inhaltsverzeichnis

1	Sicherheitshinweise	2
2	Technische Daten	3
3	Minimalverdrahtung	5
4	Inbetriebnahme	8
5	Funktionsbeschreibung der Ein- und Ausgänge	17
6	Zusätzliche Einstellmöglichkeiten	25
7	Einschränkungen im Drehzahlreglerbetrieb	28
8	Funktionsbeschreibung der Schalter (Übersicht)	29
9	Funktionen der Potentiometer (Übersicht)	30
10	Betriebszustandsanzeige	31
11	Externe Motordrosseln	33
12	EMV-gerechte Installation	34
13	Blockschaltbild	35
14	Massbild	36
15	Ersatzteilliste	36

Diese Bedienungsanleitung steht im Internet als PDF-Datei unter www.maxonmotor.com in der Rubrik «Service & Downloads», Sachnummer 306089 zur Verfügung.

EA-PS 800 R 320W - 1500W EINBAUNETZGERÄTE / BUILT-IN POWER SUPPLIES



- Weiteingangsbereich 90...264V mit aktiver PFC
- Hoher Wirkungsgrad bis 92%
- Ausgangsleistungen: 320W bis 1500W
- Ausgangsspannungen: 16V bis 360V
- Ausgangsströme: 4A bis 60A
- Flexible leistungsgeregelte Ausgangsstufe ab 1kW
- Überspannungsschutz (OVP)
- Übertemperaturschutz (OT)
- Zustandsanzeige über LEDs
- Fernfühleingang mit automatischer Erkennung
- Analoge Schnittstelle mit vielen Funktionen
- U / I programmierbar mit 0...10V
- U / I Monitorausgang mit 0...10V
- Natürliche Konvektion zur Kühlung bis 650W
- Temperaturgeregelter Lüfter zur Kühlung ab 1kW
- CE Zeichen gemäß EMV und Niederspannungsrichtlinie

- Wide input voltage range 90...264V with active PFC
- High efficiency up to 92%
- Output powers: 320W up to 1500W
- Output voltages: 16V up to 360V
- Output currents: 4A up to 60A
- Flexible, power regulated output stage from 1kW
- Overvoltage protection (OVP)
- Overtemperature protection (OT)
- Status indication via LEDs
- Remote sense with automatic detection
- Analogue interface with many functions
- U / I programmable via 0...10V
- U / I monitoring via 0...10V
- Natural convection for cooling up to 650W
- Temperature controlled fans for cooling from 1kW
- CE marked compliance to EMC, Low voltage directives

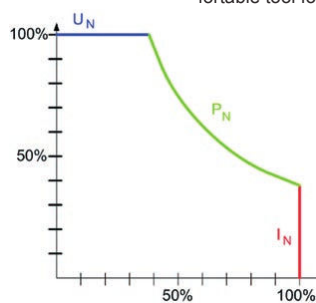
Allgemeines

Die nach neuestem Stand der Technik mikroprozessor-gesteuerten Einbaunetzgeräte der Serie EA-PS 800 R bieten dem Anwender viele Funktionen und Features serienmäßig, die das Arbeiten mit diesen Geräten erheblich erleichtern.

General

The state-of-the-art, micro-processor controlled, chassis mounting power supplies of the series EA-PS 800 R offer a wide variety of useful integrated functions and features, turning them into an extremely effective and highly comfortable tool for the user.

Geräte ab 1kW haben eine flexible, leistungsgeregelte Ausgangsstufe die bei hoher Ausgangsspannung den Strom oder bei hohem Ausgangsstrom die Spannung so reduziert, daß die maximale Ausgangsleistung nicht überschritten wird. Siehe Grafik rechts. So kann mit nur einem Gerät ein breites Anwendungsspektrum abgedeckt werden.



Units as from 1kW output power are equipped with a flexible autoranging output stage which provides a higher output voltage at lower output current, or a higher output current at lower output voltage, always limited to the max. nominal output power. See figure to the left. Therefore, a wide range of applications can already be covered by the use of just one single unit.

Eingang

Die Geräte besitzen alle eine aktive PFC und sind für den weltweiten Einsatz mit einem Netzeingang von 90V bis 264V AC ausgelegt.

Input

The equipment uses an active Power Factor Correction, enabling worldwide use on a mains input from 90V up to 264V AC.

Ausgang

Zur Verfügung stehen Geräte mit einer Ausgangsspannung von 16V bis 360V, Ströme von 4A bis 60A und Leistungen von 320W bis 1,5kW. Die Ausgangsspannung der Geräte ist von 0V bis zur U_{Nenn} einstellbar. Bei Geräten bis 65V Ausgangsspannung können zudem Festspannungen ausgewählt werden.

Output

Different units with voltage output ranges from 16V to 360V, current output ranges from 4A to 60A and power output ranges from 320W to 1.5kW, are available. The output voltage is adjustable from 0V up to max. voltage. At the units up to 65V, fixed output values can be selected.

EA-PS 800 R 320W - 1500W EINBAUNETZGERÄTE / BUILT-IN POWER SUPPLIES

Überspannungsschutz (OVP)

Um die angeschlossenen Verbraucher vor Zerstörung zu schützen ist ein Überspannungsschutz (OVP) vorhanden, der jeweils auf 110% der eingestellten Ausgangsspannung eingestellt ist. Beim Überschreiten wird der Ausgang abgeschaltet. Es wird eine Warnmeldung im Display und auf der analogen Schnittstelle ausgegeben.

Fernfühlung (Sense)

Der vorhandene Fernfühlungseingang kann direkt am Verbraucher angeschlossen werden, um den Spannungsabfall auf den Leitungen zu kompensieren. Das Gerät erkennt dies selbstständig und regelt die Ausgangsspannung direkt am Verbraucher.

Analogschnittstelle

Die Analogschnittstelle verfügt über analoge Steuereingänge mit 0...10V um Spannung und Strom von 0...100% zu programmieren. Ausgangsspannung und Strom können über analoge Monitorausgänge mit 0...10V ausgelesen werden. Weiterhin gibt es einige Statuseingänge und Ausgänge.



1000W / 1500W

Overvoltage protection (OVP)

To protect equipment connected against excess of voltage, a floating overvoltage protection (OVP) set to 110% of the adjusted output is implemented. In an event of overvoltage, the output will disconnect automatically and an alarm will be generated both on the display and the analog interface.

Remote sense

The sense input can be connected directly to the load to compensate voltage drops along the power leads. If the sense input is connected to the load, the power supply will correct the output voltage automatically in order to ensure that the accurate required voltage is available on the load.

Analogue interface

Analogue inputs with voltage ranges from 0V...10V for set up voltage and current from 0...100% are available. For monitoring the output voltage and current, analogue outputs are realised with voltage ranges from 0V...10V. Several digital inputs and outputs are available for controlling and monitoring the status.

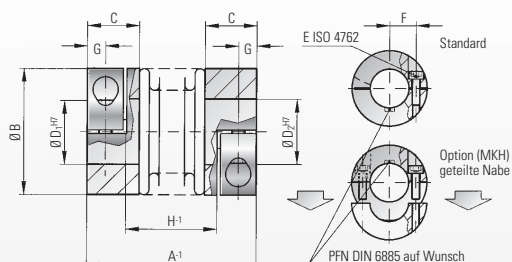
Technische Daten	Technical Data	EA-PS 816-20 R	EA-PS 832-10 R	EA-PS 865-05 R	EA-PS 832-20 R	EA-PS 865-10 R
Eingangsspannung	Input voltage	90...264V	90...264V	90...264V	90...264V	90...264V
-Frequenz	-Frequency	45...65Hz	45...65Hz	45...65Hz	45...65Hz	45...65Hz
-Leistungsfaktorkorrektur	-Power factor correction	>0,99	>0,99	>0,99	>0,99	>0,99
-Eingangsstrom (230V)	-Input current (230V)	1,6A	1,6A	1,6A	3,2A	3,2A
Ausgangsspannung	Output voltage	0...16V	0...32V	0...65V	0...32V	0...65V
-Stabilität bei 10-90% Last	-Stability at 10-90% load	<0,05%	<0,05%	<0,05%	<0,05%	<0,05%
-Stabilität bei $\pm 10\% \Delta U_E$	-Stability at $\pm 10\% \Delta U_{IN}$	<0,02%	<0,02%	<0,02%	<0,02%	<0,02%
-Restwelligkeit	-Ripple	<40mV _{pp}				
-Ausregelung 10-100% Last	-Regulation 10-100% load	<2ms	<2ms	<2ms	<2ms	<2ms
-OVP Einstellung	-OVP adjustment	0...17,6V	0...35,2V	0...71,5V	0...35,2V	0...71,5V
Ausgangsstrom	Output current	0...20A	0...10A	0...5A	0...20A	0...10A
-Stabilität bei 0-100% ΔU_A	-Stability at 0-100% ΔU_{OUT}	<0,15%	<0,15%	<0,15%	<0,15%	<0,15%
-Stabilität bei $\pm 10\% \Delta U_E$	-Stability at $\pm 10\% \Delta U_{IN}$	<0,05%	<0,05%	<0,05%	<0,05%	<0,05%
-Restwelligkeit	-Ripple	<50mA _{pp}				
Max. Ausgangsleistung	Max. output power	320W	320W	325W	640W	650W
Abmessungen (BxHxT)	Dimensions (WxHxD)	218x83x163mm	218x83x163mm	218x83x163mm	218x83x163mm	218x83x163mm
Gewicht	Weight	4,7kg	4,7kg	4,7kg	4,9kg	4,9kg
Artikel Nr.	Article No.	21540101	21540102	21540103	21540104	21540105

Technische Daten	Technical Data	EA-PS 8160-04 R	EA-PS 880-40 R	EA-PS 880-60 R	EA-PS 8360-10 R	EA-PS 8360-15 R
Eingangsspannung	Input voltage	90...264V	90...264V	90...264V	90...264V	90...264V
-Frequenz	-Frequency	45...65Hz	45...65Hz	45...65Hz	45...65Hz	45...65Hz
-Leistungsfaktorkorrektur	-Power factor correction	>0,99	>0,99	>0,99	>0,99	>0,99
-Eingangsstrom (230V)	-Input current (230V)	3,2A	5A	7,5A	5A	7,5A
Ausgangsspannung	Output voltage	0...160V	0...80V	0...80V	0...360V	0...360V
-Stabilität bei 10-90% Last	-Stability at 10-90% load	<0,05%	<0,05%	<0,05%	<0,05%	<0,05%
-Stabilität bei $\pm 10\% \Delta U_E$	-Stability at $\pm 10\% \Delta U_{IN}$	<0,02%	<0,02%	<0,02%	<0,02%	<0,02%
-Restwelligkeit	-Ripple	<40mV _{pp}	<70mV _{pp}	<70mV _{pp}	<100mV _{pp}	<100mV _{pp}
-Ausregelung 10-100% Last	-Regulation 10-100% load	<2ms	<2ms	<2ms	<2ms	<2ms
-OVP Einstellung	-OVP adjustment	0...176V	0...88V	0...88V	0...396V	0...396V
Ausgangsstrom	Output current	0...4A	0...40A	0...60A	0...10A	0...15A
-Stabilität bei 0-100% ΔU_A	-Stability at 0-100% ΔU_{OUT}	<0,15%	<0,15%	<0,15%	<0,15%	<0,15%
-Stabilität bei $\pm 10\% \Delta U_E$	-Stability at $\pm 10\% \Delta U_{IN}$	<0,05%	<0,05%	<0,05%	<0,05%	<0,05%
-Restwelligkeit	-Ripple	<50mA _{pp}	<100mA _{pp}	<100mA _{pp}	<15mA _{pp}	<15mA _{pp}
Max. Ausgangsleistung	Max. output power	640W	1000W	1500W	1000W	1500W
Abmessungen (BxHxT)	Dimensions (WxHxD)	218x83x163mm	90x240x400mm	90x240x400mm	90x240x400mm	90x240x400mm
Gewicht	Weight	4,9kg	8,9kg	9,2kg	8,9kg	9,2kg
Artikel Nr.	Article No.	21540106	21540107	21540108	21540109	21540110



MODELL MK2

TECHNISCHE INFORMATION



Eigenschaften:

- spielfrei und verdrehsteif
- Ausgleich von Fluchtungsfehlern
- kraftschlüssige Verbindung durch Klemmnaben
- für hochdynamische Anwendungen
- niedriges Trägheitsmoment

Material:

Balg aus hochelastischem Edelstahl, Nabe AL

Aufbau:

Standard: mit Klemmnabe und je einer seitlichen Schraube ISO 4762

Option (MKH): geteilte Klemmnabe, beide Nabenhälften sind in einer Richtung abnehmbar

Temperaturbereich:

-30 bis +120° C

Drehzahlen:

Bis 10.000 1/min. über 10.000 1/min. in ausgewuchteter Ausführung

Lebensdauer:

Bei Beachtung der techn. Hinweise sind die Kupplungen dauerfest und wartungsfrei

Passungsspiel:

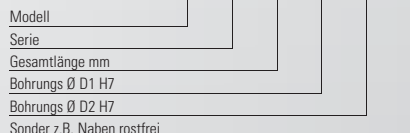
Welle-Nabenverbindung 0,01 - 0,05 mm

Sonderlösungen:

Wie andere Passungen, Passfedernuten, Sondermaterial und Bälge sind kurzfristig möglich

Bestellbeispiel

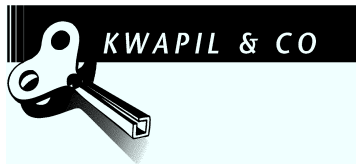
MK2 / 5 / 25 / 4 / 5 / XX



MKH = geteilte Nabe

Modell MK 2		Serie														
		5			10			15		20		45		100		
Nenn Drehmoment (Nm)	T _{KN}	0,5			1,0			1,5		2,0		4,5		10		
Gesamtlänge (mm)	A	25	28	31	27	30	33	30	35	35	40	44	46	54	50	60
Außendurchmesser (mm)	B	15			15			19		25		32		40		
Passungslänge der Nabe (mm)	C	9			9			11		13		16		16		
Sonderbohrung von Ø bis Ø H7 (mm)	D _{1/2}	3-7			3-7			3-8		3-12,7		5-16		5-24		
Standardbohrung H7 (mm)	D _{1/2}	6			6			6		6/10		10		10		
Schrauben ISO 4762	E	M2			M2			M2,5		M3		M4		M4		
Anzugsmoment (Nm)	E	0,43			0,43			0,85		2,3		4		4,5		
Mittenabstand (mm)	F	4,5			4,5			6		8		10		15		
Abstand (mm)	G	3			3			3,5		4		5		5		
Einfügelänge (H)	H	12	15	18	14	17	20	14,5	19,5	17	22	26	23,5	31,5	27,5	37,5
Trägheitsmoment (gcm ²)	J _{ges}	2,6	2,8	3	3	3,4	3,6	8,5	9,5	25	27	29	100	108	160	205
Gewicht ca. (g)		9	9	9	9	10	11	22	24	36	38	40	74	78	120	130
Torsionssteife (Nm/rad)	C _T	280	210	170	510	380	320	750	700	1200	1300	1200	7000	5000	9050	8800
axial (mm)	max. Werte	0,4	0,5	0,6	0,4	0,5	0,6	0,5	0,7	0,5	0,6	0,7	0,7	1	1	1,2
lateral (mm)		0,15	0,2	0,25	0,15	0,2	0,25	0,15	0,2	0,15	0,2	0,25	0,2	0,25	0,2	0,3
angular (Grad)		1	1,5	2	1	1,5	2	1,5	1,5	1,5	1,5	2	1,5	2	1,5	2

A.2 Offers for Key Components



**ANGEBOT
NUMMER**

940719

Seite: 1
 Datum: 20.04.2009
 Anfrageart: per E-Mail / 16.04.2009
 Anfrage von: Herr Michael Felber
 Telefon Kunde: 0316/873 7464
 Telefax Kunde: 0316/873 7963
 Bearbeiter/DW: Astrid Schwanzer/23
 Fachberater/DW: Günther Roither/40

Institut für Prozess- und Partikeltechnik
 z. Hd. Herr Michael Felber
 Inffeldgasse 21/A/II
 AT-8010 Graz

Sehr geehrter Herr Felber,
 wir danken für Ihre Anfrage und bieten wie folgt an:

Pos.	Artikel	Menge	Einheit	Preis	%	Einzelpreis	Termin	Gesamt
1	351144 maxon EC Motor Ø25 BL D 250W KL 1WE FS6x16.1 mit Hallsensoren	1,00	STK	467,06		467,06		467,06
2	306089 maxon digitaler 4-Q-EC Verstärker 70 V / 10 A, Drehzahlregelung, Stromregelung, Modulgehäuse, DEC 70/10	1,00	STK	356,54		356,54		356,54

Zahlung: 10 Tage 2,00% Skonto, 30 Tage netto
 Versandart: Paketdienst
 Lieferbedingungen: Ab Lager Wien, verzollt, exkl. Verpackung

Nettobetrag	EUR	823,60
+ 20,00% MwSt.		164,72
Gesamtbetrag	EUR	988,32

D E R E R F O L G S A N T R I E B

Kwapil & Co Gesellschaft mbH Telefon +43 (1) 278 85 85-0
 Antriebstechnik und Elektronik Telefax +43 (1) 278 85 86
 A-1210 Wien, Austria, Kammelpweg 9 UID-Nr. ATU15072604
 www.kwapil.com FN126212g, Handelsgericht Wien, DVR 0396419



nano80 Handels Ges.m.b.H.
Donaufelder Straße 247
1220 Wien
Tel.: +43 (1) 203 7901- 0
Fax: +43 (1) 203 7901-21
besuchen Sie uns auf: www.nano80.at

[nano80 Ges.m.b.H., Donaufelder Str. 247, 1220 Wien](http://www.nano80.at)

TU Graz
Institut für Prozess und Partikeltechnik
Z. Hd. Herrn Felber Michael
Inffeldgasse 21A
A-8020 Graz
AUSTRIA

unser Zeichen: pjk@nano80.at
Telefon: +43 (1) 203 7901-20
Fax: +43 (1) 203 7901-21
Wien, am 17.04.2009

Angebotsnr.: 7835

Sehr geehrter Herr Felber,

wir beziehen uns auf unser Telefongespräch vom 17.04.2009 und freuen uns, Ihnen folgendes Angebot unterbreiten zu können:

1 Stück	Elektro-Automatik Einbaunetzgerät	€ 1048,00 / Stück
	Typ: EA-PS 880-40 R	
	Ausgangsspannung 0...80V	
	Ausgangsstrom 0...40A	
	Ausgangsleistung 0...1000Watt	

Preise: in Euro, netto, ab Lager nano80
Versand: € 7,50- +MWSt. / Paket bis 31,5kg
Lieferzeit: ca. 3-4 Wo.
Zahlung: 14 Tage netto
Angebotsgültigkeit: 30 Tage

Wir hoffen, dass dieses Angebot soweit Ihren Vorstellungen entspricht und verbleiben

mit freundlichen Grüßen,

Pil-Jung Kim
[nano80](http://www.nano80.at) Handels Ges.m.b.H.

Firmenbuchnummer beim HG Wien: FN 97526x; Geschäftsführer: Ing. Ramesh Sharma; UID: ATU 147 36 106; ARA: 2995; ERA: 50129;
Bankverbindung: Erste Bank, 1010 Wien, BIC: GIBAATWW, IBAN(Kto.): AT86 2011 1000 0045 1800; BLZ: 20111;

B Simulation-Related Content

B.1 Particle Tracking

Introduction

The solver icoLagrangianFoam (as well as buoyantSimpleLagrangianFoam) tracks individual particles that have been injected into a given flow field. The particle velocities are calculated using a simple force balance.

Main solver

The main solver can be found in icoLagrangianFoam.C and is based on icoFoam. Particle specific routines are linked into this solver through the files:

- HardBallParticle.H (declaration of variables and function for the particles needed in the solver)
- IncompressibleCloud.H (declaration of variables and function for the assembly of particles needed in the solver)
- IncompressibleCloudI.H (declares an inline function for the momentumSource and is included in IncompressibleCloud.H)
- createParticles.H (initializes the pointMesh “pMesh”, the interpolated velocities “vpi” and the cloud of particles (class “IncompressibleCloud”) “cloud”).

In the program loop the particle cloud “cloud” is evolved, i.e., particles are injected and moved, using the included file “evolveParticles.H”. The momentum from the suspended particles is included in the Navier-Stokes equation (i.e., the Ueqn.) via the function “momentumSource”.

Runtime Parameters to be Specified for Particle Cloud “cloud”

The solver is designed such, that the file “cloudProperties” is readin when the object “cloud” is generated, i.e., at the moment when the line

```
IncompressibleCloud cloud(vpi,U);
```

is hit in the file “createParticles.H”. What is done during this readin can be seen in the constructor of an object (in our case the name is “cloud) of the class “IncompressibleCloud” is initialized. The source code for this can be found consequently in IncompressibleCloud.C (line 47 to 101). The meaning of the variables is commented in the file IncompressibleCloud.H, where these variables are declared.

Overview of the Involved Classes

Basically, two classes are involved in particle tracking:

- the “HardBallParticle” class that is derived from the main “Particle” class of OpenFOAM (definition of the “Particle” class can be found in OpenFOAM-1.5/src/lagrangian/basic/Particle). This class specifies what the particle “is able to do” and which properties make up the particle. Consequently it defines how particles are moved, what happens when they contact the wall, what particle properties are written to files.
In OF's standard implementation, the class “parcel” is similar to the class “HardBallParticle” used

in icoLagrangianFoam.

- The “IncompressibleCloud.C” class is derived from the main “Cloud” class of OpenFOAM (definition can be found in OpenFOAM-1.5/src/lagrangian/basic/Cloud). It specifies what happens when a cloud of particles is generated, how particles can be injected and tracked, interpolation of fluid properties to the particles, particle management and some “on-top” functions for writing particle parameters to files. In OF's standard implementation, the class “spray” is similar to the class “IncompressibleCloud” used in icoLagrangianFoam.

How the Particle Cloud of Class “IncompressibleCloud” is Evolved

All functions responsible for what happens with the object “cloud” can be found in the definition of its class, i.e., IncompressibleCloud.C. The important functions are:

- IncompressibleCloud::evolve() (interpolates velocities, tracks and injects particles)
- IncompressibleCloud::track() (This is a call to the function Cloud<HardBallParticle>::move (can be found in ..OpenFOAM-1.5/src/lagrangian/basic/Cloud/), which further leads to a call of HardBallParticle::move (definition in file HardBallParticle.C).
- IncompressibleCloud::inject() (This sets the initial position, velocity and diameter of the injected particles)
- IncompressibleCloud::writeFields() (calls the function HardBallParticle::writeFields that specifies what to write to the file. This function is defined in the file HardBallParticleIO.C).

How Particles Move

The function call “cloud.evolve()” leads to a call of the function “evolve” of the object cloud, in which “track” is called which finally leads to a call of HardBallParticle::move (defined in HardBallParticle.C). This function consists of several substeps (lagrangian substeps dt) where the calculation of the fluid flow is frozen and only the particle position/velocity is updated. In this function basically the particle is moved to the new position using:

toPos=position()+U_*dt

Here U_ is the particle velocity. Thus, a simple forward Euler algorithm is used. Finally, the function “trackToFace” (defined in the class “Particle” in the src-dir of OpenFOAM-1.5) is used to update the variable “position()” of the particle.

Because the particle can be accelerated by the surrounding fluid, U_ has to be updated. This is done with the call to the function “updateProperties” (defined in HardBallParticle.C from line 120 to 144.

The velocity is updated using:

U()=(U() + coeff*Upos + data.g()*dt)/(1. + coeff);

Where coeff is calculated out of the lagrangian time step dt and the relaxation time of the particle.

How to Use It

- call icoLagrangianFoam in the case directory. The resulting directories should no have a sub-folder

- “lagrangian” that contains the particle variables.
- do a “foamToVTK” to convert the data to VTK format as paraFoam is not able to display the particles.
- call “paraFoam”
- Press “Delete”
- Press “Ctrl+o” to open a file
- Select the file “<case>.vtk” in the “VTK” directory of your case. The Eulerian data (flow field) will be loaded.
- Select the file “defaultCloud.vtk” in the “VTK/lagrangian/defaultCloud” directory of your case.
- Select the “defaultCloud.vtk” data in paraview and press on the “Glyph” button. Select “Sphere” as Glyph Type and select an appropriate scale mode (e.g. scalar and as scalar d, the particle diameter) and scale factor.

Lagrangian-Stochastic-Deterministic (LSD) Model

Basic Description

In order to model the effect of turbulent fluctuations (which are not resolved when using, e.g., the RANS approach), we have implemented a stochastic model that mimics the motion of turbulent eddies. For this purpose we use the so-called Lagrangian-Stochastic-Deterministic (LSD) model. This model is detailed and compared with other models in Frank.¹

Within the LSD model, the instantaneous fluid velocity \vec{u}_{inst} is calculated from the (resolved) mean velocity field \vec{u}_{mean} (this velocity field might be obtained from, e.g., a RANS or URANS simulation) and velocity fluctuations \vec{u}_{fluct} :

$$\vec{u}_{inst} = \vec{u}_{mean} + \vec{u}_{fluct} \quad (1)$$

The velocity fluctuations \vec{u}_{fluct} are determined under the assumption of an isotropic turbulence field and calculated via a stochastic process. Specifically, turbulent fluctuations are random vectors (Gaussian distributed) with a mean value of zero and a RMS value of:

$$\sigma_{\vec{u}_{fluct}} = \sqrt{\frac{2}{3} \cdot k} = \sqrt{\overline{\vec{u}_{fluct}^2}} \quad (2)$$

Here, k is the turbulent kinetic energy and $\sigma_{\vec{u}_{fluct}}$ is the standard deviation of the ensemble-averaged velocity fluctuations $\overline{\vec{u}_{fluct}^2}$ in each spatial direction.

The calculation of these turbulent velocity fluctuations mimics the effect of turbulent eddies that a particle crosses on the way through the flow field. In order to take into account the size L_E and the life time T_E of this turbulent eddy, these two properties of the eddy are calculated at each point in time. Therefore, the eddy life time T_E is set equal to the turbulent time scale of the smallest eddy in the flow field:

$$T_E = c_T \cdot \frac{k}{\varepsilon} \quad (3)$$

Here, ε is the energy dissipation rate and c_T is a model parameter. c_T is typically taken equal to 0.3 and varies in the range between 0.135 and 0.46 depending on the flow situation.¹ c_T strongly impacts particle dispersion and is the critical parameter of the LSD model.

The size of the eddy x_E is set equal to the turbulent length scale given by:

$$x_E = c_\mu^{1/2} \cdot \frac{k^{3/2}}{\varepsilon} = T_E \cdot \sqrt{\frac{2}{3}} \cdot k \quad (4)$$

Hence, L_E can be directly evaluated from the eddy life time and the turbulent kinetic energy. Once T_E and x_E have been calculated, the two criteria on when the particle leaves the eddy can be formulated. These criteria are:

$$T_p \geq T_E \quad (5)$$

and

$$x_p \geq x_E \quad (6)$$

Here, T_p is the time the particle was in the eddy (i.e., the particle is released from the eddy when the eddy brakes down) and x_p is the length the particle has travelled through the eddy (i.e., the particle leaves the eddy when it has completely crossed it). T_p can be easily calculated by integrating the time since the eddy has been generated. x_p is calculated from the magnitude of the relative velocity of the particles and the instantaneous flow field:

$$x_p = \int_0^t |\bar{v}_{rel}| dt \quad (7)$$

$$\bar{v}_{rel} = \bar{U} - \bar{u}_{inst} \quad (8)$$

Here \bar{U} denotes the particle velocity. To account for spatial inhomogeneities of the turbulent flow properties (i.e., k and ε), T_E and x_E are calculated every time step and the time T_p as well as the path x_p travelled by the particle in the eddy are scaled according to:

$$T_{p,n+1} = T_{p,n+1} \cdot \frac{T_{E,n+1}}{T_{E,n}} \quad (9)$$

$$x_{p,n+1} = x_{p,n+1} \cdot \frac{x_{E,n+1}}{x_{E,n}} \quad (10)$$

Also, the velocity fluctuations are scaled according to:

$$\bar{u}_{fluct,n+1} = \bar{u}_{fluct,n} \cdot \frac{\sigma_{\bar{u}_{fluct,n+1}}}{\sigma_{\bar{u}_{fluct,n}}} \quad (11)$$

The advantage of the LSD model is its simplicity and its numerical efficiency. Drawbacks are:

- the correlation of velocity fluctuations in space and time are not taken into account,
- the turbulent eddy is assumed to be isotropic,
- there is no correlation between the individual components of the fluctuating velocity, i.e., the continuity equation of the velocity fluctuations is not satisfied.

More elaborate models can be found in Sommerfeld.²

Programm Code

```
//Calculate actual eddy properties at the current particle position
scalar tENew=data.cT()*kpos/(epsilonpos + SMALL); //eddy lifetime acc. to T. Frank, Eqn. 4.73
scalar xENew=tENew*sqrt(2./3.*kpos); //eddy length scale acc. to T. Frank, Eqn. 4.74
scalar sigmaNew=sqrt(2./3.*kpos); //RMS-value of fluctuation velocity, Eqn. 4.72

//Update the particle variables to account for local change in turbulent properties
tP()=tP()*tENew/(tE()+SMALL); //acc. to T. Frank, Eqn. 4.77
xP()=xP()*xENew/(xE()+SMALL); //acc. to T. Frank, Eqn. 4.77
Ufluct()=sigmaNew/(sqrt(2./3.*k())+SMALL)*Ufluct(); //acc. to T. Frank, Eqn. 4.78
tE()=tENew; //Save new eddy properties for next time step
xE()=xENew; //Save new eddy properties for next time step
k() = kpos; //Save new eddy properties for next time step

//Move Particle within the eddy
Uinst = Upos + Ufluct();
vrel=U()-Uinst; //Relative velocity between particle and instantaneous velocity field
tP()=tP()+dt; //integrate time the particle is in the eddy
xP()=xP()+mag(vrel)*dt; //integrate the particle distance

// Check if particle has entered a new eddy
if( (tP() > tE()) || (xP() > xE()) ) //particle was too long in eddy or has crossed the eddy
{
    //Particle has left the eddy, generate new eddy and set particle velocities
    tmp=vector(fluctuation.GaussNormal(), fluctuation.GaussNormal(),
        fluctuation.GaussNormal()) / sqrt(3.); //A random vector with a RMS length of 1
    Ufluct()=tmp*sigmaNew;
    Uinst = Upos + Ufluct();
    tP()=0.0;
    xP()=0.0;
}
```

Sample Calculation

In order to highlight the effect of the LSD model on particle dispersion, we have performed a sample calculation of the flow in a clean room (see Figure 1).

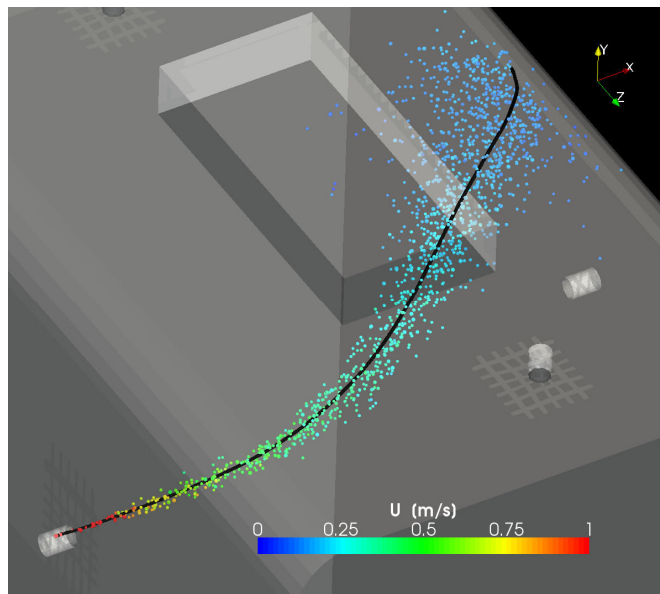


Figure 1: Comparison of particle positions for LSD model switched off (black line) and LSD model activated with $c_T=0.3$ (particles colored with their velocity).

Additional Variables needed

1. “LSDSwitch”

Switches the model on/off, to be set in `IncompressibleCloud.H` (2x, also enable access!) and `IncompressibleCloud.C`.

2. “kInterpolator”

Sets the interpolator to get the k-value at the particle position,

3. “k”

the turbulent kinetic energy, to be defined in `IncompressibleCloud.H` and `IncompressibleCloud.C` as well as in `HardBallParticle.H` and `HardBallParticle.C` as a saved variable for each particle.

4. LSD properties of each particle:

vector `Ufluct_;` //The fluctuating velocity at the particle position

vector `Uinst;` //Temp vector of the instantaneous velocity of the fluid at the particle position

scalar `k_;` //The turbulent kinetic energy at the particle position

```
scalar tP_; //The actual time the particle is in the turbulent eddy
scalar xP_; //The actual distance the particle has travelled in the turbulent eddy
scalar tE_; //The eddy lifetime
scalar xE_; //The eddy length scale
vector tmp; //temp value for a random vector
vector vrel; //relative velocity between particle and fluid
Random fluctuation; //The GaussNormal-distributed random variable
```

They have to be defined in `HardBallParticle.H`

Temporary vectors to hinder particle moving :

- vector `USource`;
- vector `scaleVector`;
- vector `UsourceScaled`;

should be also defined in `HardBallParticle.H` prior to use in `HardBallParticle.C`

5. Constant `cT`

is a property read in in the dict “`cloudProperties`”, similar to `LSDSwitch`, default value should be `cT=0.3` as in Frank, p. 86

The effect of the LSD model is illustrated in

Figure 1 with an example in which the flow field is obtained using a RANS simulation (case “`testCaseBuoyantSimpleLagrangianFoam`”). In case no model for the turbulent fluctuations is used, the particle dispersion cannot be reconstructed in this case as the flow field is time-independent.

References

- (1) Frank T. Parallele Algorithmen für die numerische Simulation dreidimensionaler, disperser Mehrphasenströmungen und deren Anwendung in der Verfahrenstechnik. Aachen, Germany: Shaker Verlag, 2002.
- (2) Sommerfeld M. Modellierung und numerische Berechnung von partikelbeladenen turbulenten Strömungen mit Hilfe des Euler/Lagrange-Verfahrens. Aachen: Shaker Verlag, 1996.

B.2 EDR Profile Simulations

B.2.1 M4 Script File for a Parameter-Based Mesh Generation of the Shear Device

```

reset
# * * * * *
# * * * * *
# Shear_device_cubit_journal_m4_script.m4
# This macro creates a cubit journal file for the mesh
# generation of the USD shear device.
# This temporary mesh is designed for a final conversion
# via the makeAxialMesh application for wedge shaped
# simulations in OpenFOAM.
# 23. January 2009
# Revision 2
# by Michael Felber

changeom(//)changequote([,])
define(calc, [esyscmd(perl -e 'printf ($1)')]])
define(VCOUNT, 0)
define(vlabel, [[// ]Vertex $1 = VCOUNT define($1, VCOUNT)
define([VCOUNT], incr(VCOUNT))])
define(pi, 3.14159265)

# measurements are given in meters

# PARAMETER DEFINITIONS
# * * * * *
# * * * * *

# chamber
define(chamber_radius, 0.025) # radius of the chamber
define(chamber_height, 0.02) # height of the chamber

# rotating disc and shaft
define(rd_radius, 0.02) # radius of the rotating disc
define(rd_thickness, 0.001) # thickness of the rotating
disc

```

```
define(shaft_radius, 0.003) # thickness of the shaft

# rotating cell zone
define(cellzone_thickness, 0.001) # thickness of the
    rotating cell zone
define(cellzone_tip_x_thickness, calc(2*cellzone_thickness)
    ) # thickness of the cellzone in x direction at the tip
    of the disc

# meshing parameters
define(y_thickness, 0.001) # thickness of the geometry in y
    direction
define(mesh_cellzone_constant_size, 0.0001) # constant size
    of the surface mesh of the cellzone surface
define(mesh_bulkzone_min_size, 0.0001) # geometry adaptive
    meshing of the bulk surface: min cell size
define(mesh_bulkzone_max_size, 0.0002) # geometry adaptive
    meshing of the bulk surface: max cell size
define(mesh_bulkzone_max_gradient, 1.05) # geometry
    adaptive meshing of the bulk surface: cell gradient

# required calculated measurements in cubit
define(twocellzoneanddisc_thickness, calc(2*
    cellzone_thickness+rd_thickness)) # thickness of the
    rotating disc with the cell zone above and below
define(move_vol3_x, calc((chamber_radius-shaft_radius)
    *(-1/2)))
define(half_chamber_radius, calc(chamber_radius/2))
define(half_chamber_height, calc(chamber_height/2))

# GENERATING THE GEOMETRY
# * * * * *
# * * * * *

# Creating the basic geometry
# Outline of the geometry
brick x chamber_radius y y_thickness z chamber_height
```

```
# Shifting the geometry to the origin
volume 1 move x half_chamber_radius y 0 z
    half_chamber_height

# Create the outline of the rotating disc
brick x rd_radius y y_thickness z rd_thickness

# Aligning the rotating disc brick and the main brick (
    centered in z)
align volume 2 surface 10 with surface 4

# Subtract the rotating disc from the main brick
subtract volume 2 from volume 1

# Create, align and subtract the shaft for the rotating
    disc
brick x shaft_radius y y_thickness z half_chamber_height
align volume 3 surface 20 with surface 1
volume 3 move x move_vol3_x y 0 z 0
subtract volume 3 from volume 1

# Create rotating cell zone
# Rotating cell zone near the shaft
brick x cellzone_thickness y y_thickness z
    half_chamber_height
align volume 4 surface 34 with surface 26
chop volume 1 with volume 4 keep
delete volume 1 4

# Create and align brick for the rotating cell zone at the
    tip of the disc
brick x cellzone_tip_x_thickness y y_thickness z
    twocellzoneanddisc_thickness
align volume 7 surface 56 with surface 47

# Create rotating cell zone on the top of the disc
surface 49 copy
sweep surface 59 direction z distance cellzone_thickness
```

```
# Create rotating cell zone on the bottom of the disc
surface 48 copy
sweep surface 65 direction nz distance
    cellzone_thickness

# Delete overlapping volumes
subtract volume 7 8 9 from volume 6 keep
delete Volume 6

# Unite the rotating cell zone parts
unite volume 5 7 8 9

# Imprint and merge all volumes
imprint volume all
merge volume all

# MESHING
# * * * * *
# * * * * *

# Meshing the rotating cell zone
surface 55 size mesh_cellzone_constant_size
mesh surface 55
refine curve 168 122 134 numsplit 1 bias 1 depth 5 smooth
refine curve 168 122 134 numsplit 1 bias 1 depth 5 smooth

# Meshing the bulk zone
surface 79 sizing function type skeleton scale 3
    time_accuracy_level 3 min_size mesh_bulkzone_min_size
    max_size mesh_bulkzone_max_size max_gradient
    mesh_bulkzone_max_gradient
surface 79 scheme pave
mesh surface 79

# Mirror the front rotating cell zone surface mesh
surface 57 scheme mirror source surface 55 nosmoothing
```

```
mesh surface 57
delete mesh surface 57 propagate
surface 57 scheme mirror source surface 55 nosmoothing
mesh surface 57

# Mirror the front bulk surface mesh
surface 71 scheme mirror source surface 79 nosmoothing
mesh surface 71
delete mesh surface 71 propagate
surface 71 scheme mirror source surface 79 nosmoothing
mesh surface 71

# Meshing the y direction with a 1 cell layer
volume 10 7 interval 1
mesh volume 10 7

# DEFINING CELL ZONES AND FACES

create sideset 1
create sideset 2
create sideset 3
create sideset 4
sideset 1 name "rotor"
sideset 2 name "stator"
sideset 3 name "frontandback"
sideset 4 name "axis"

create block 1
block 1 name "rotcellzone"

# Adding volumes to the block rotcellzone
block 1 volume 7

# Adding surfaces to sideset rotor
sideset 1 surface 40 surface 70 surface 38 surface 81

# Adding surfaces to sideset stator
sideset 2 surface 41 surface 80 surface 76 surface 77
```

```
# Adding surfaces to sideset frontandback
sideset 3 surface 79 surface 55 surface 71 surface 57

# Adding surfaces to sideset axis
sideset 4 surface 67 surface 78
```

B.2.2 The makeMesh Shell Script

```
#!/bin/sh

makeAxialMesh axis frontandback
mv ./1/polyMesh/* ./constant/polyMesh
rm -r ./1

# cleaning up the mesh
collapseEdges 1e-9 179
mv ./1/polyMesh/* ./constant/polyMesh
rm -r ./1

# remove unused patches
sed '18,18d' ./constant/polyMesh/boundary > ./constant/
polyMesh/output
mv ./constant/polyMesh/output ./constant/polyMesh/boundary
sed '17{p;s/./4/;}' ./constant/polyMesh/boundary > ./
constant/polyMesh/output
mv ./constant/polyMesh/output ./constant/polyMesh/boundary
sed '38,49d' ./constant/polyMesh/boundary > ./constant/
polyMesh/output
mv ./constant/polyMesh/output ./constant/polyMesh/boundary
sed '20,25d' ./constant/polyMesh/boundary > ./constant/
polyMesh/output
mv ./constant/polyMesh/output ./constant/polyMesh/boundary

sed '20,20d' ./constant/polyMesh/cellZones > ./constant/
polyMesh/output
mv ./constant/polyMesh/output ./constant/polyMesh/cellZones
```

```

sed '19{p;s/.*/rotor/;}' ./constant/polyMesh/cellZones > ./
  constant/polyMesh/output
mv ./constant/polyMesh/output ./constant/polyMesh/cellZones
#sed '18,18d' ./constant/polyMesh/cellZones > ./constant/
  polyMesh/output
#mv ./constant/polyMesh/output ./constant/polyMesh/
  cellZones
#sed '17{p;s/.*/1/;}' ./constant/polyMesh/cellZones > ./
  constant/polyMesh/output
#mv ./constant/polyMesh/output ./constant/polyMesh/
  cellZones

cellSet
cp ./system/faceSetDict_rotorFaces ./system/faceSetDict
faceSet
cp ./system/faceSetDict_noBoundaryFaces ./system/
  faceSetDict
faceSet
setsToZones -noFlipMap

checkMesh

```

B.2.3 Determination of the EDR Profiles

Formatting Shell Script for the EDR Data File for Import in Octave

```

cd ..
sed '1,1d' ./logSummary_1.dat > ./EDR_calc_single_case/
  output
sed 's/[]() []//g' ./EDR_calc_single_case/output > ./
  EDR_calc_single_case/logSummary_1_formatted.dat
cd EDR_calc_single_case
rm ./output

```

EDR Profile Calculation Script for Octave

```
clear all;

%%%%%%%%%%%%%%%%%%%%%%%%%%%%%%%%%%%%%%%%%%%%%%%%%%%%%%%%%%%%%%%%%%%%%%%%
% EDR profile calculations
%%%%%%%%%%%%%%%%%%%%%%%%%%%%%%%%%%%%%%%%%%%%%%%%%%%%%%%%%%%%%%%%%%%%%%%%

% Parameters
%%%%%%%%%%%%%%%%%%%%%%%%%%%%%%%%%%%%%%%%%%%%%%%%%%%%%%%%%%%%%%%%%%%%%%%%

% Filename
filename_load = ['./logSummary_1_formatted.dat'];
filename_write = ['EDR_Summary.dat'];

% EDR
N_EDRclasses = 200; % Number of EDR classes
EDR_max = 1e+07;

% Data file format: Number of columns per parameter
N_time = 1; % Simulationtime
N_epsilon = 1; % Epsilon: 1 column per particle
N_U = 3; % Velocity: 3 columns per particle
N_partpar = N_epsilon + N_U; % Sum of columns of parameters
    per particle

%%%%%%%%%%%%%%%%%%%%%%%%%%%%%%%%%%%%%%%%%%%%%%%%%%%%%%%%%%%%%%%%%%%%%%%%

% Preparing data files
%%%%%%%%%%%%%%%%%%%%%%%%%%%%%%%%%%%%%%%%%%%%%%%%%%%%%%%%%%%%%%%%%%%%%%%%
data1 = load(filename_load); % Reading data from opened
    file and writing it to the matrix "data1"
data1(:,1) = data1(:,1) - data1(1,1); % Offset the time
    data to start at 0

% Calculation
```

```
%%%%%%%%%%%%%%%%%%%%%%%%%%%%%%%%%%%%%%%%%%%%%%%%%%%%%%%%%%%%%%%%%%%%%%%%

N_C1 = columns(data1); % Number of columns in the data file
N_P1 = (N_C1-N_time)/(N_partpar); % Number of particles in
    the data file

% For-loop to evaluate the maximum EDR value each particle
    passed
for Counter=1:N_P1;

    N_Col = (Counter - 1) * 4 +2; % Column position of
        epsilon corresponding to the number of the particle
    maxEDR(1,Counter) = max(data1(:,N_Col)); % Generating a
        vector of maximum EDR values each particle passed

    if (maxEDR(1,Counter) < 0);
        maxEDR(1,Counter)=0;
    endif;

endfor;

% For-loop to count the number of particles corresponding
    to each EDR class

EDR_count = zeros(N_EDRclasses, 5); % Generate the output
    matrix

nonlinear_class_size = log10(EDR_max) / N_EDRclasses;

for Counter2=1:N_EDRclasses; % For-loop for the EDR classes

% Linear class size distribution
    EDR_class_low = (EDR_max / N_EDRclasses) * (Counter2 - 1)
        ;
    EDR_class_high = EDR_class_low + (EDR_max / N_EDRclasses)
```

```

;

% Nonlinear class size distribution
% EDR_class_low = 10 ** (nonlinear_class_size * (Counter2 -
    1));
% EDR_class_high = 10 ** (nonlinear_class_size * Counter2);

EDR_count(Counter2,1) = EDR_class_low; % Writing the
    lower class limit
EDR_count(Counter2,2) = EDR_class_high; % Writing the
    higher class limit
EDR_count(Counter2,3) = (EDR_class_high + EDR_class_low)
    / 2; % Writing the average class limit to the matrix

for Counter3=1:N_P1; % For-loop for the number of
    particles

    currentEDR = maxEDR(1,Counter3);

    if (EDR_class_low <= currentEDR); % If the EDR of the
        current particle is within the range, ...
        if (currentEDR < EDR_class_high); % the particle
            counter is increased by one
            EDR_count(Counter2,4) = EDR_count(Counter2,4) + 1;
        endif;
    endif;

endfor;

EDR_count(Counter2,5) = EDR_count(Counter2,4) / (N_P1 * (
    EDR_count(Counter2,2) - EDR_count(Counter2,1)));

endfor;

% Output to file
%%%%%%%%%%%%%%%%%%%%%%%%%%%%%%%%%%%%%%%%%%%%%%%%%%%%%%%%%%%%%%%%%%%%%%%%

```


for more details.

You should have received a copy of the GNU General
Public License
along with OpenFOAM; if not, write to the Free Software
Foundation,
Inc., 51 Franklin St, Fifth Floor, Boston, MA
02110-1301 USA

Application

wallMassFlux

Description

Calculates and writes the mass flux for all patches as
the boundary field
of a volScalarField and also prints the integrated flux
for all wall
patches.

```
\*-----*
-----*/
```

```
#include "fvCFD.H"
```

```
// * * * * *
* * * * * //
```

```
int main(int argc, char *argv[])
{
    timeSelector::addOptions();
    #include "setRootCase.H"
    # include "createTime.H"
    instantList timeDirs = timeSelector::select0(runTime,
        args);
    # include "createMesh.H"

    Info << "Calculate total_epsilon" << endl;
    volScalarField total_epsilon
```

```
(
    IObject
    (
        "total_epsilon",
        runTime.timeName(),
        mesh,
        IObject::NO_READ,
        IObject::AUTO_WRITE
    ),
    mesh,
    dimensionedScalar
    (
        "total_epsilon",
        dimensionSet(0, 5, -3, 0, 0),
        scalar(1.0)
    )
);

forAll(timeDirs, timeI)
{
    runTime.setTime(timeDirs[timeI], timeI);
    Info<< "Time = " << runTime.timeName() << endl;
    mesh.readUpdate();
#    include "createFields.H"

    total_epsilon = sum(mesh.V()*epsilon) ;

    Info<< "Exporting Data..." << endl;
    total_epsilon.write();
}

Info<< "Export finished" << endl;

return 0;
}
```

```
// *****
***** //
```

C EDR Calculation for Radial Exit Nozzles

C.1 Numerical Calculation of the EDR

```
clear all; %%%%%%%%%%% %
    Calculation of the Impact EDR
    %%%%%%%%%%%
% Parameters %%%%%%%%%%%
% Exit velocity [m/s] v_exit_pool = [50, 100, 150,
    200, 250]; %v_exit_pool = [1];
% Droplet diameter [m] D_pool = [1e-4, 2e-4, 1e-3,
    5e-3]; %D_pool = [1e-5];
% Impact distance [m] s_imp = 0.367;
% Density of the droplet [kg/m3] Rho_drop = 1000;
% Density of the surrounding fluid [kg/m3] Rho =
    1.2306;
% Kinematic viscosity of the surrounding fluid [m2/
    s] Nu = 144e-7;
% Time step size [s] delta_t = 1e-8;
% Other constants Pi = 3.14159265;
% Output files %%%%%%%%%%%
% Over-write existing file fileid = fopen('
    EDR_calculation_data.txt', 'w'); fclose(fileid);
% Open file to append data fileid = fopen('
    EDR_calculation_data.txt', 'a'); fprintf(fileid
    , 'D_drop\t v_exit\t time\t v_imp\t s_drop\t EDR\
    n');
% Calculation %%%%%%%%%%%
for j=1:length(D_pool)    D_drop = D_pool(j);
    for i=1:length(v_exit_pool)    m = 1/6 * Pi
        * D_drop**3 * Rho_drop; % Mass of the
        spherical droplet    A = 1/4 * D_drop**2 * Pi
        ; % Cross-sectional area of the spherical
        droplet
```

```

v_exit = v_exit_pool(i);      v_drop = v_exit; %
    Starting velocity      time = 0; % Starting
    time      s_drop= 0; % Starting position
function Cdvar = Cd (v_drop,D_drop,Nu)
    % Reynolds number of the droplet
    Re = D_drop * abs(v_drop) / Nu;
    % Drag relationship for spheres (Clift and
    Gauvin, Re < 3e5)      Cdvar = 24 / Re *
    (1 + 0.15 * Re**0.687) + 0.42 / (1 + 4.25
    e4 * Re**(-1.16));
endfunction
%fprintf(fileid, '%e %e %e %e %e \t start\n',
    D_drop, v_exit, time, v_drop, s_drop);
loopterminator=0;
while (loopterminator<1)
    % Stepping further in time      time = time
    + delta_t;
    % Calculating the position of the droplet
    s_drop = s_drop + v_drop * delta_t;
    % Velocity difference per time step for
    turbulent flow conditions      Re =
    v_drop * D_drop / Nu;
    if (Re>0.1)      delta_v = - Rho * A * Cd(v_drop
    ,D_drop,Nu) * v_drop**2 / (2 * m) *
    delta_t;      endif
    % Velocity difference per time step for
    laminar flow conditions      if (Re<=0.1)
    delta_v = (-3) * Pi * Nu * Rho * D_drop
    * v_drop * delta_t / m;      endif
    % Calculating the new velocity      v_drop =
    v_drop + delta_v;
%%%%%% %      if (Re>0.1) %      fprintf(fileid,
    '%e %e %e %e %e turb\n', D_drop, v_exit, time,
    v_drop, s_drop); %      endif % %      %
Velocity difference per time step for laminar
flow conditions %      if (Re<=0.1) %
fprintf(fileid, '%e %e %e %e %e lam\n', D_drop,
v_exit, time, v_drop, s_drop); %      endif
%%%%%%

```

```
% If the impact distance is reached the
    position is rounded as the impact distance
    and the loop is terminated          if (
    s_drop >= s_imp)  s_drop = s_imp;
    loopterminator=1;          endif
% If the droplet velocity is small it is
    rounded as 0 and the loop is terminated
    if (v_drop < 1e-33)  v_drop = 0;
    loopterminator=1;          endif
endwhile
% Calculating the resulting EDR          EDR =
    v_drop**3 / (2 * D_drop);
% Write data to file          fprintf(fileid, '%e %e
    %e %e %e %e\n', D_drop, v_exit, time,
    v_drop, s_drop, EDR);          endfor
endfor
%t_imp= -m/(3*Pi*Nu*Rho*D_drop)*log(1-s_imp*3*Pi*Nu
    *Rho*D_drop/(v_exit*m));
%fprintf(fileid, '%e t_imp \n', t_imp);
% Closing files fclose(fileid); close all;
%%%%%%%%%%%%%%%%%%%%%%%%%%%%%%%%%%%%%%%%%%%%%%%%%%%%%%%%%%%%%%%%%%%%%%%%%
```

C.2 Validation of the Numerical Approach

C.2.1 Drag after Clift and Gauvin

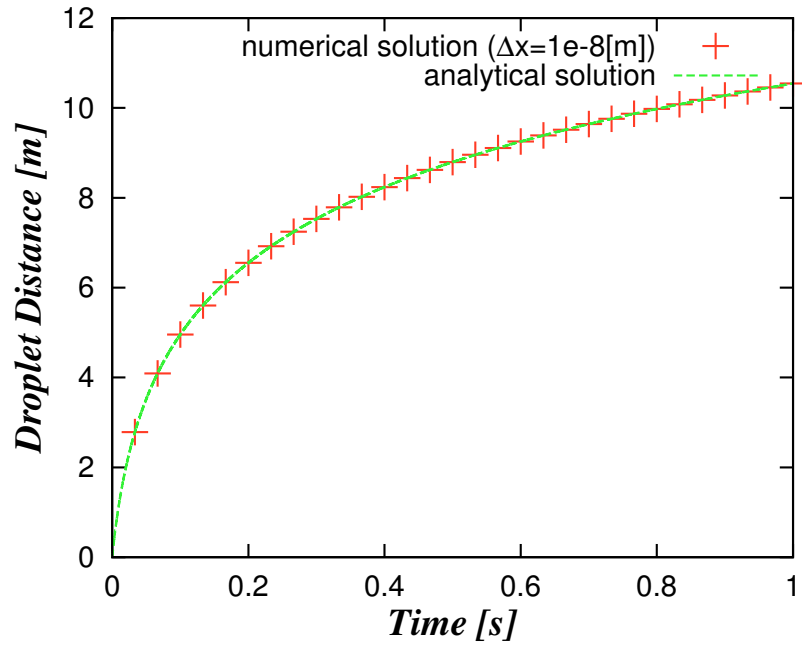


Figure C.1: Validation of the numerical calculation for a constant drag coefficient c_D after Clift and Gauvin with $D_{drop} = 10^{-3}$ [m] and $v_{exit} = 150$ [$m s^{-1}$] [Clift et al., 1978]

C.2.2 Stokes Law

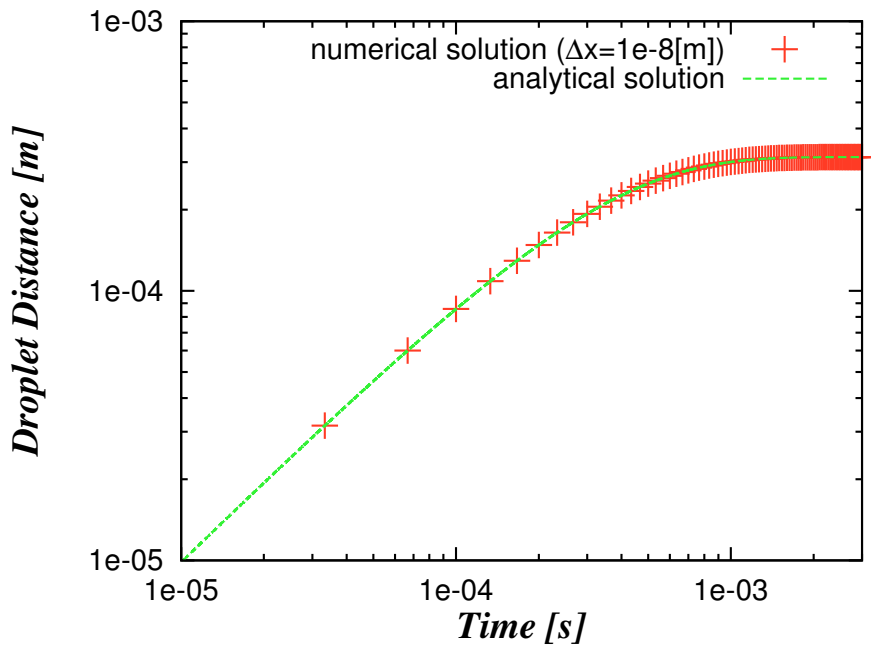


Figure C.2: Validation of the numerical calculation for Stokes' law ($D_{drop} = 10^{-5}$ [m], $v_{exit} = 1$ [$m s^{-1}$])

D Data from Sandoz

D.1 Data from Test Runs of the Disc Stack Separator

Betriebsparameter des Separators X-311.1 zum Zeitpunkt der Sonderprobenahme

Betriebsparameter	Charge	Fluß [kg/h]	Temperatur [°C]
Zulauf V-320.0 1.Zentrifugation F1311672	45601974	1931.6	10.0
Ablauf 1.Zentrifugation F1311682	45601974	1260.2	10.0
Zulauf V-310.0 2.Zentrifugation F1311672	45601974	2500.8	8.9
Ablauf 2.Zentrifugation F1311682	45601974	1904.5	8.9
Zulauf V-325.0 3.Zentrifugation Klärung 1. Teil F1311672	45601974	3005.9	5.8
Ablauf 3.Zentrifugation Klärung 1. Teil F1311682	45601974	2596.2	5.8
Zulauf V-325.0 3.Zentrifugation Klärung 2. Teil F1311672	45601974	2999.2	7.4
Ablauf 3.Zentrifugation Klärung 2. Teil F1311682	45601974	2503.5	7.4
Zulauf V-320.0 1.Zentrifugation F1311672	45601975	1998.0	10.9
Ablauf 1.Zentrifugation F1311682	45601975	1408.2	10.9
Zulauf V-310.0 2.Zentrifugation F1311672	45601975	2501.2	8.5
Ablauf 2.Zentrifugation F1311682	45601975	1928.3	8.5
Zulauf V-325.0 3.Zentrifugation Klärung 1. Teil F1311672	45601975	3000.0	5.3
Ablauf 3.Zentrifugation Klärung 1. Teil F1311682	45601975	2591.1	5.3
Zulauf V-325.0 3.Zentrifugation Klärung 2. Teil F1311672	45601975	3003.7	6.2
Ablauf 3.Zentrifugation Klärung 2. Teil F1311682	45601975	2578.9	6.2

Bestimmung der Viskosität und der Biofeuchtmasse anhand der EP2000 Sonderproben des Separators X-311.1

2. Viskosität

Probenbezeichnung	Charge	Viskosität [cP]
Zulauf V-320.0 1.Zentrifugation	45601974	1.53
Klarphase V-320.0 1.Zentrifugation	45601974	1.05
Konzentrat V-320.0 1.Zentrifugation	45601974	6.33
Zulauf V-310.0 2.Zentrifugation	45601974	1.35
Klarphase V-310.0 2.Zentrifugation	45601974	0.99
Konzentrat V-310.0 2.Zentrifugation	45601974	6.27
Zulauf V-325.0 3.Zentrifugation Klärung 1. Teil	45601974	2.07
Klarphase V-325.0 3.Zentrifugation Klärung 1. Teil	45601974	0.99
Konzentrat V-325.0 3.Zentrifugation Klärung 1. Teil	45601974	12.2
Zulauf V-325.0 3.Zentrifugation Klärung 2. Teil	45601974	2.31
Klarphase V-325.0 3.Zentrifugation Klärung 2. Teil	45601974	1.11
Konzentrat V-325.0 3.Zentrifugation Klärung 2. Teil	45601974	8.85
Zulauf V-320.0 1.Zentrifugation	45601975	2.25
Klarphase V-320.0 1.Zentrifugation	45601975	1.47
Konzentrat V-320.0 1.Zentrifugation	45601975	7.23
Zulauf V-310.0 2.Zentrifugation	45601975	1.77
Klarphase V-310.0 2.Zentrifugation	45601975	1.47
Konzentrat V-310.0 2.Zentrifugation	45601975	6.27
Zulauf V-325.0 3.Zentrifugation Klärung 1. Teil	45601975	3.75
Klarphase V-325.0 3.Zentrifugation Klärung 1. Teil	45601975	1.47
Konzentrat V-325.0 3.Zentrifugation Klärung 1. Teil	45601975	50.0
Zulauf V-325.0 3.Zentrifugation Klärung 2. Teil	45601975	3.45
Klarphase V-325.0 3.Zentrifugation Klärung 2. Teil	45601975	1.41
Konzentrat V-325.0 3.Zentrifugation Klärung 2. Teil	45601975	52.3

Meßtemperatur 25°C

Meßtemperatur 8°C

Anmerkung:
zur Viskositätsmessung wurde die Spindel S18 verwendet
alle Messungen wurden mit einer Drehzahl von 50RPM durchgeführt
1cP = 1mPa*s

Bestimmung der Viskosität und der Biofeuchtmasse anhand der EP2000 Sonderproben des Separators X-311.1

1. Biofeuchtmasse

Probenbezeichnung	Charge	Biofeuchtmasse [%]
Zulauf V-320.0 1.Zentrifugation	45601974	13.62
Klarphase V-320.0 1.Zentrifugation	45601974	0.69
Konzentrat V-320.0 1.Zentrifugation	45601974	39.95
Zulauf V-310.0 2.Zentrifugation	45601974	12.43
Klarphase V-310.0 2.Zentrifugation	45601974	0.69
Konzentrat V-310.0 2.Zentrifugation	45601974	46.60
Zulauf V-325.0 3.Zentrifugation Klärung 1. Teil	45601974	4.02
Klarphase V-325.0 3.Zentrifugation Klärung 1. Teil	45601974	0.17
Konzentrat V-325.0 3.Zentrifugation Klärung 1. Teil	45601974	18.31
Zulauf V-325.0 3.Zentrifugation Klärung 2. Teil	45601974	4.04
Klarphase V-325.0 3.Zentrifugation Klärung 2. Teil	45601974	0.17
Konzentrat V-325.0 3.Zentrifugation Klärung 2. Teil	45601974	19.30
Zulauf V-320.0 1.Zentrifugation	45601975	12.02
Klarphase V-320.0 1.Zentrifugation	45601975	1.17
Konzentrat V-320.0 1.Zentrifugation	45601975	39.94
Zulauf V-310.0 2.Zentrifugation	45601975	10.86
Klarphase V-310.0 2.Zentrifugation	45601975	1.10
Konzentrat V-310.0 2.Zentrifugation	45601975	43.28
Zulauf V-325.0 3.Zentrifugation Klärung 1. Teil	45601975	4.59
Klarphase V-325.0 3.Zentrifugation Klärung 1. Teil	45601975	0.75
Konzentrat V-325.0 3.Zentrifugation Klärung 1. Teil	45601975	18.59
Zulauf V-325.0 3.Zentrifugation Klärung 2. Teil	45601975	4.54
Klarphase V-325.0 3.Zentrifugation Klärung 2. Teil	45601975	0.57
Konzentrat V-325.0 3.Zentrifugation Klärung 2. Teil	45601975	18.55